June 2020

Log File-Based Dose Reconstruction to Moving Targets during Lung Stereotactic Body Radiation Therapy

Andrew S. McGuffey
Louisiana State University and Agricultural and Mechanical College

LOG FILE-BASED DOSE RECONSTRUCTION TO MOVING TARGETS DURING LUNG STEREOTACTIC BODY RADIATION THERAPY

A Thesis

Submitted to the Graduate Faculty of the
Louisiana State University and
Agricultural and Mechanical College
in partial fulfillment of the
requirements for the degree of
Master of Science

in

The Department of Physics and Astronomy

by
Andrew Scott McGuffey
B.S., Western Kentucky University, 2017
August 2020

Acknowledgements

First, I express my sincerest gratitude to the members of my supervisory committee: Dr. Justin Sick, Dr. Kenneth (Kip) Matthews II, Dr. Jonas Fontenot, and Dr. Manos Chatzopoulos, for their advice, support, and investment of time and interest in this project. I give special thanks to my research advisor, Dr. Justin Sick, for his mentorship and guidance throughout the duration of this project. The oversight and direction provided by my supervisory committee were essential to the completion of this project.

Next, I acknowledge clinical physics faculty, Mr. Connel Chu, Mr. Daniel Neck, Dr. David Solis, and Mr. David Perrin, for their help in utilizing clinical resources for this project.

Next, I thank our program coordinators, Dr. Yao Zeng, Mrs. Susan Hammond, and Ms. Katelynn Fontenot, for their assistance in scheduling meetings, answering administrative questions, and helping me navigate the path toward the completion of degree requirements.

I acknowledge several of my fellow LSU Medical Physics students: Payton Bruckmeier, Audrey Copeland, Troy Jacobs, Stephanie Wang, and Phillip Wall. I believe that all of our discussions about coursework and research, and, in general, the time we spent together over the past 3 years were invaluable to my education and experience here at LSU.

Finally, I thank my parents, Kim Douros and Gary McGuffey, and my siblings, Adam, Aiden, and Abigail, for their endless love, support, and encouragement for me to pursue my interests and goals.

Table of Contents

List of Tables

List of Figures

Abstract

Purpose: To perform film-based verification of 4D dose reconstruction to moving targets during lung stereotactic body radiation therapy (SBRT).

Introduction: Current patient-specific quality assurance measures to test deliverability of plans with dynamic intensity modulation involve delivering beams to static measurement device and comparing the planned dose to measurement. However, motion-induced dose errors are not detected with static measurement. Previous studies have investigated combining machine log data with respiratory tracking to determine moving-target dose. By combining machine log data with anatomic and density information at each breathing phase from 4D-CT, intrafraction anatomical deformation due to respiration may be accounted for. However, to our knowledge, a film-based verification of dose reconstruction using machine log data, intrafraction respiratory tracking, and 4D-CT has yet to be performed.

Methods: Lung SBRT plans were anonymized for 12 patients treated at our institution. Treatment plans were copied onto known geometry (programmable respiratory phantom) and dose was computed. Each SBRT plan was delivered to the phantom twice; first using 3 sec/breath (SPB), again at 6 SPB. Respiratory traces were acquired during treatment. Logfiles were acquired after treatment and partitioned according to breathing amplitude. Next, in-house code was used to import logfile beams into the treatment planning system. Dose was computed on each 4D-CT image using the imported beams and deformably accumulated. The accumulated, planned, and measured doses for each plan and breathing rate were compared using gamma analysis.

Results: Gamma passing rates (GPR) (3%, 2mm, 10% threshold) of 4D dose reconstruction vs. planned dose were >94% (mean 98.9% range 94.1%-100%) for all plans at each breathing rate. No significant difference was found between the 3 and 6 SPB GPRs (p=0.310). Overall, the 4D

dose reconstructions were found to better agree with film measurement, within the tumor motion extent, than the treatment plan for both breathing rates (3 SPB: p=0.013, 6 SPB: p=0.017).

Conclusions: Log file-based dose reconstruction was verified using film measurement for 12 lung SBRT plans delivered to a respiratory motion phantom. We showed that, given predictable phantom motion, 4D dose reconstruction resulted in significantly higher GPR compared with film than treatment plan to static geometry.

Chapter 1. Introduction

1.1. Background and Significance

1.1.1. Lung Cancer

Lung cancer comprises 1 out of 8 new cancer cases and has a 5-year survival rate of less than 20%, making it the leading cause of cancer-related death in the United States. Approximately 6% of men and women will be diagnosed with lung cancer during their lifetimes (NCI 2019). The majority (85%) of lung cancer cases are an aggressive form known as non-small cell lung cancer (NSCLC), which is resistant to conventional radiation therapy techniques and chemotherapy. Thus, the most effective treatment for early-stage NSCLC is surgical resection (NCI 2019). However, many lung cancer patients are not surgical candidates, either from being medically inoperable or refusing surgery. For patients with medically inoperable stage-I NSCLC, an advanced radiotherapy technique known as stereotactic body radiation therapy (SBRT) has been shown to have similar efficacy to surgery (Onishi, et al. 2011).

1.1.2. Stereotactic Body Radiation Therapy

Radiation therapy is the use of particulate or electromagnetic radiation to treat disease. Radiation can have a therapeutic effect in several ways; the most notable is reproductive death of cells via mitotic catastrophe in which a cell attempts to divide using damaged DNA. The most probable mechanism of DNA damage varies among radiation type. For photons, most probable is indirect action, in which radiation interactions result in formation of free radical oxygen molecules capable of damaging DNA. However, if given enough time between radiation events, a cell may be able to repair sublethal damage to its DNA. Normal tissues are better at repairing damaged DNA than cancer. By fractionating a prescribed dose of radiation over many separate treatments

(e.g., once per weekday for six weeks), rapidly dividing normal tissues can repair sublethal radiation damage and acute detrimental health effects of radiation are reduced (Liu, et al. 2012).

Linear accelerators (linacs) are used to produce the x-rays used for radiation therapy. To generate these x-rays, electrons are accelerated using microwave energy to MeV energies before striking a tungsten target. The acceleration of the electrons by the electric field of the tungsten nuclei results in the release of bremsstrahlung x-rays. This radiation is forward-directed (Faddegon, et al. 1990), which compromises the flatness of the radiation field delivered to the patient. To flatten the field, a flattening filter, thicker in the middle and decreasing thickness radially, is placed in front of the x-ray beam. Since the beam is selectively attenuated in the middle, flatness is improved at the patient (Vassiliev, et al. 2006). However, the flattening filter by principle removes x-rays from the beam, which results in a decreased dose rate and increased treatment duration.

Conventional radiation therapy involves between 10 and 30 fractions with 1.8-3 Gy delivered per fraction. In contrast with conventional fractionation, a course of SBRT typically consists of 1-5 fractions with 6-30 Gy delivered per fraction (Benedict, et al. 2010). Increasing dose per fraction results in an increase of the radiation biological effect, which increases the effectiveness of SBRT against NSCLC. To protect surrounding normal tissues, SBRT must be delivered to the delineated target volume within millimeter margins (Shah, et al. 2013).

The linac may be operated in flattening-filter-free mode to increase the dose rate and decrease treatment time. To further decrease treatment time, volumetric modulated arc therapy, or VMAT, may be employed to deliver SBRT. VMAT is characterized by continuous delivery of radiation dose during gantry rotation. Delivering radiation during gantry rotation reduces treatment time, which increases patient comfort as well as daily patient throughput. VMAT seeks to optimize

dose delivery by utilizing complex beam apertures to modulate the fluence of a given field during treatment while the gantry rotates around the patient. This fluence is modulated by binary multi-leaf collimators (MLCs), which are two banks of 0.5 cm-wide tungsten leaves that move perpendicularly to the beam central axis to attenuate and conform the beam to a shape determined by the computer optimization of dose objectives set during the planning process.

1.1.3. SBRT Treatment Planning and Motion Management

The first step in the radiation treatment planning process is to gather information for both patient setup and dose calculation. This information is collected from a computed tomography (CT) simulation, in which a scan of the patient is taken on a specialized CT scanner with a table that simulates the treatment table. This specialized table allows the patient to be positioned and immobilized just as they would be during treatment. These CT images are exported to the dosimetrist, and the treatment is planned under the assumption that the CT image will represent the patient throughout the course of treatment. CT image pixel intensity values are calibrated to represent x-ray attenuation at their geometric location within the image. These intensity values are converted to Hounsfield units (HU) during image processing, which are proportional to the linear attenuation coefficient. The linear attenuation coefficient is a measure of the probability of energy deposition at that location. Commercial treatment planning systems (TPSs), such as Pinnacle^3 (Philips Radiation Oncology Systems, Fitchburg, WI, USA), combine information on the energy spectrum and fluence of the beam with the attenuation coefficients from the CT image set to compute radiation dose (Papanikolaou and Stathakis 2009).

While the planning CT scan provides only a snapshot of tumor location during the scan, respiratory correlated CT, or 4D-CT, is used to account for tumor motion during the planning stage for lung SBRT. This imaging technique allows the physicist to determine the extent of tumor

motion that occurred during the scan. 4D-CT is standard-of-care for patients in the simulation phase of lung SBRT treatment (Brandner, et al. 2017). To incorporate the motion of the tumor in the planning phase, an internal target volume (ITV) containing the range of tumor motion during the 4D-CT scan is contoured onto the maximum intensity projection (MIP) of the 4D-CT image set as shown in Figure 1.1.

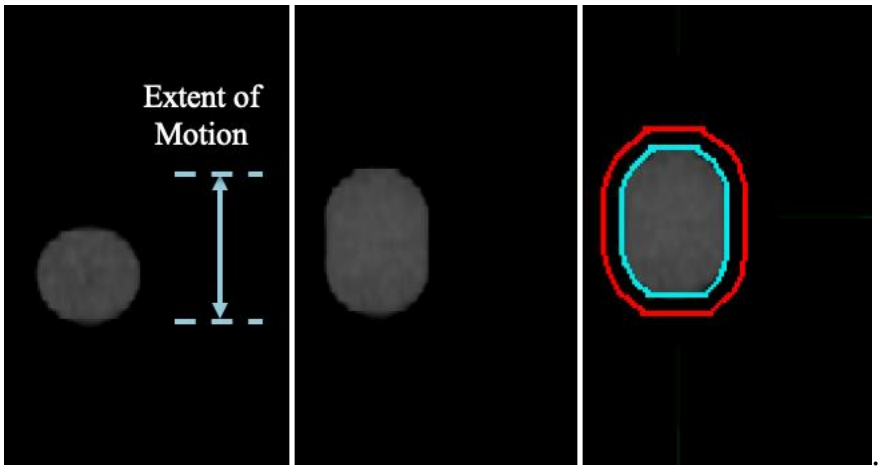

Figure 1.1. Delineation of tumor motion extent using maximum intensity projection. Left: 4D-CT image of phantom at amplitude position 0.0. Center: Maximum intensity projection (MIP) over all 4D-CT images. Right: MIP contours; internal target volume containing motion (ITV, cyan) and planning target volume including setup margin (PTV, red = ITV + 0.5 cm).

The MIP gives the planner a visualization of the full range of motion of the tumor. The planning target volume (PTV) is created for lung SBRT by expanding the internal target volume by a setup margin, 5 mm according to the Radiation Therapy Oncology Group (RTOG) 0813 protocol. The setup margin accounts for variance in day-to-day patient alignment. The prescription dose is planned to be conformally delivered to the PTV. Using computer optimization in the planning system, VMAT SBRT beams are planned to meet treatment goals, such as target dose heterogeneity, PTV dose coverage, and normal tissue dose allowance.

1.1.4. Effects of Tumor Motion on Delivered Dose

Respiratory motion can affect the location of abdominal and thoracic tumors during planning as well as treatment. The delivered dose to the moving target may deviate from the statically planned dose via two effects: (1) gradient effect and (2) interplay effect (Jiang, et al. 2003).The gradient effect may be thought of as the 'smearing' of the dose distribution along the principle axis of tumor motion. This smearing occurs when the moving target passes through heterogeneities in the static dose distribution and is present in any radiation treatment modality. Interplay effect, in contrast, is only present in treatments with dynamic intensity modulation. Interplay effect can be described as the destructive or constructive interference between the tumor motion and moving MLC aperture (Stambaugh, et al. 2013). Computer optimization in VMAT or intensity-modulated radiation therapy (IMRT) planning involves a numerical optimization of plan objectives which may result in beam shapes that do not always contain the full target volume (Bortfeld, et al. 2002). Hence, part or all of the tumor may be outside of the radiation field at given times during treatment, reducing tumor dose and increasing dose to normal tissue.

Bortfeld, et al. found, using the Central Limit Theorem, that the probability density function of the dose to a given point becomes near-Gaussian after about 5 fractions (Bortfeld, et al. 2002). The low number (5 or fewer) of fractions in an SBRT treatment regimen may inhibit these errors from being 'averaged out'. The interplay effect can result in significant dose deviations. Jiang, *et al* showed inter-fraction dose delivery variation of up to 30% for single-field IMRT, and up to 18% for 5-field IMRT (Jiang, et al. 2003). Court, et al. showed that for 2-arc VMAT, interplay effect becomes more significant as breathing rate decreases and amplitude of motion increases (differences as great as 5% for 2cm motion at 5 SPB) (Court, et al. 2010). Kubo, et al. showed

dose differences of up to 10% between successive film measurements in a programmable respiratory phantom (Kubo, et al. 2018).

1.2. Motivation for Research

Patient-specific quality assurance (QA) measures use a static 2D diode array for verification measurement, which does not account for the effect of motion on the absorbed dose to the target region. The delivery log file written by the linac during each treatment has been previously studied as a way to provide a way to compute the delivered dose to a moving target, if combined with intrafraction respiratory data. Poulsen et al. proposed an efficient log file binning methodology, through which they reconstructed delivered dose to moving targets by reformatting the log file into a motion-mimicking treatment plan using isocenter shifts (Poulsen, et al. 2012). Zou, et al. proposed a log file 4D-binning methodology, using deformable image registration to map doses from each 4D-CT phase image to a reference phase, and simulated motion effects during VMAT lung SBRT (Zou, et al. 2014). Chung, et al. applied the isocenter shift method of Poulsen *et al.* and correlated the tracked respiratory signal with measured tumor displacement from the 4D-CT dataset (Chung, et al. 2018). Meijers, et al. applied log file-based 4D dose accumulation to evaluate moving target dose in pencil beam proton therapy (Meijers, et al. 2019).

Log file-based dose reconstruction for moving targets, utilizing the patient 4D-CT dataset, is less well-established than the method of isocenter shifts. To our knowledge, an end-to-end verification of the 4D-CT-based procedure for retrospective QA has yet to be performed. 4D-CT may provide advantages to log file dose reconstruction over to the isocenter shift method, such as information on the patient anatomical deformation due to respiration at each breathing phase, as well as deformation of the tumor. In addition, we find no publications utilizing Elekta delivery log files for reconstructing dose to a moving target. This study seeks to perform an end-to-end

verification of log file-based dose reconstruction using 4D-CT and utilizing Elekta log files. In addition, we seek to study the effect of breathing rate on the resultant dose accumulations.

Chapter 2. Methods and Materials

2.1. Patient Selection, Phantom Imaging, and Treatment Planning

2.1.1. Retrospective Patient Selection and Anonymization

The patients for the anonymized cohort were selected using the criteria presented in Table 2.1. The most restrictive criterion was the respiratory motion management strategy, as many lung SBRT patients in our clinic are treated employing breath-hold techniques. The final sample size meeting our criteria was 12 patients.

Table 2.1 Patient selection criteria.

Criterion	Requirement
Lung Left or Right	Either
Intra-lung tumor location	Any
Dose per Fraction	≥ 10 Gy
Number of fractions	≤ 5 fractions
Superior-inferior motion	≥ 5 mm
Motion Management Strategy	Free-breathe
Beam Energy	6 MV flattening-filter-free

Patients in the cohort were anonymized using Mobius3D software (Varian Medical Systems, Palo Alto, CA). Anonymized RT Plan files were downloaded from Mobius3D and imported into the MOSAIQ Radiation Oncology (Elekta AB, Stockholm, Sweden) record and verify system via the RTP Import function to retrieve the SBRT plans to be delivered. Each patient was simulated using the Quasar Respiratory Motion Phantom.

2.1.2. Quasar Respiratory Motion Phantom

The Quasar respiratory motion phantom (Modus Medical Systems, London, ON, Canada) features a body oval, cedar ‘lung’ cylindrical insert with acyclic tumor, and a drive motor which moves the lung insert and stage. Figure 2.1 presents an annotated image of the Quasar phantom, and Figure 2.2 shows an axial CT image of the Quasar phantom.

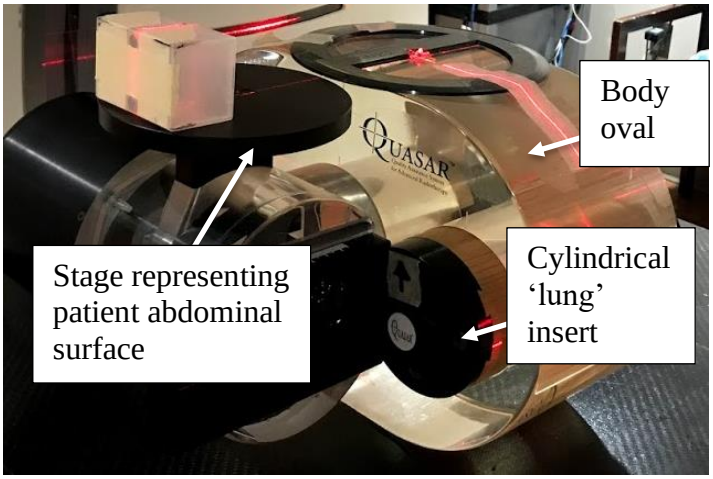

Figure 2.1. Image of Quasar Respiratory Motion Phantom.

The amplitude of motion of the lung insert in the superior-inferior direction can be set manually or controlled via software. Software control can be performed using an external computer connected to the phantom via a local network connection and using the accompanying software package . Fiducial markers on the sides (pictured in CT image) and top of the phantom allow alignment of the phantom with room lasers for imaging or beam delivery.

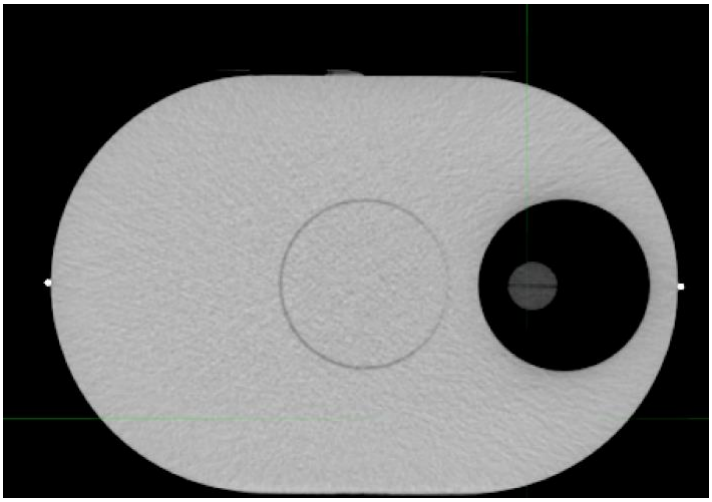
Figure 2.2. Axial computed tomography image of Quasar Respiratory Motion Phantom.

Several cylindrical insert types are available for the phantom, including an ion chamber insert, halved tumor insert, and film cassette.

2.1.3. 4D-CT Acquisition

Respiratory-correlated CT, or 4D-CT, is an imaging technique in which a series of CT images taken during respiration are sorted according to the respiratory cycle. The respiratory cycle is tracked during the scan using an external fiducial marker. The position of this marker's motion over time results in a respiratory trace. To acquire a respiratory trace for image binning, breathing motion is tracked during the scan using an external surrogate signal; e.g., an IR reflector box set on the patient's abdomen. The external surrogate signal is used to bin images to the section of the patient breathing cycle in which they were acquired. These sections are known as breathing phases.

4D-CT scans were acquired of the moving Quasar respiratory phantom simulating a sin6 breathing pattern for each amplitude in the patient cohort. The sin6 wave was defined as

$$\sin_6(t) = A \sin^6\left(\frac{\pi t}{T_B}\right) \tag{2.1}$$

where A is the peak-to-peak amplitude of motion in the superior-inferior direction and T_B is the breathing period, usually presented in seconds-per-breath (SPB). Figure 2.3 presents a plot of a sine6 wave.

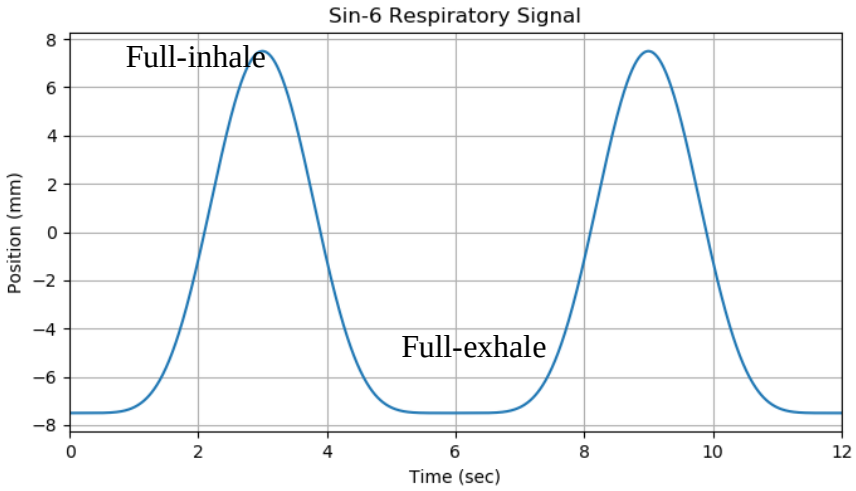

Figure 2.3. Sin6 wave used to represent human breathing cycle.

The sin6 function was used because it is characterized by long full-exhale position and short full-inhale position, which better represents a human breathing cycle than a sine wave. This respiratory-mimicking waveform was imported as a text file into the Quasar Programmable Respiratory Phantom software (Modus Medical Systems, London, ON, Canada), in which the waveform could be scaled to match a given amplitude and frequency. For our 4D-CT acquisition, we used a breathing period of 6 SPB.

This amplitude was set to be the peak-to-peak distance of the sin6 wave. To simulate right and left lungs, the phantom was rotated on the table so that the cedar 'lung' insert matched patient-left or patient-right. An IR reflector box was positioned on top of the phantom stage, and motion tracking was performed using the Varian Real-time Position Monitoring (RPM) system. The Varian RPM system is a clinical external surrogate marker tracking system which utilizes an IR camera. Images were acquired using a GE LightSpeed 16RT CT scanner (GE Healthcare, Chicago, IL) and clinical 4D gating protocol.

The clinical 4D gating protocol begins with a scout CT scan, which is a static X-ray scan taken to localize the target and select the imaging volume for the following scans. Next is a 3D helical CT scan, which was skipped for our procedure as it was not used for our treatment planning. Finally, the last scan in the protocol is a cine scan. During the cine scan, the CT table remains fixed while the x-ray tube rotates around the patient for a duration of time within which a full breathing cycle takes place. After this duration of time has ended, the x-ray tube turns off and the table indexes in the cephalocaudal direction by the axial slice thickness, nominally 2.5 mm, to the next position. Then, the x-ray tube turns back on and another full breathing cycle is captured. Finally, this process is repeated until the scan length indicated by the scout CT localization has been filled.

The cine image acquisition process results in CT data acquisition at each successive table position from which CT images are reconstructed. To reconstruct cine images, these CT data are sorted into bins corresponding to divisions of the respiratory cycle, called phases. We used a clinically 'long' breathing rate of 6 SPB used during the CT scan, to reduce the tumor speed and thus reduce motion artefacts. To ensure enough time for both a full breathing cycle image capture with time for reconstruction, the cine time, or the duration at which the table is at each index and the x-ray tube is on, is set to the duration of the breathing cycle plus a nominal tube ramp-up time of two full CT rotations. For our 6 SPB breathing period, this value was 7.7 seconds. Scan parameters are provided in Table 2.2.

Table 2.2. Cine scan parameters for 4D-CT acquisition.

Cine Scan Parameter	Value
X-Ray Tube Voltage	120 kV
X-Ray Tube Current	400 mA
Slice Thickness	2.5 mm
Cine Time Between Images	0.15 s
Cine Time	7.7 s

Cine image sets are much larger in file size than conventional CT images, and the limiting factor in our sampling was the number of images allowed for a single scan, which is limited to under 3,000. Using the parameters in Table 2.2., for a full scan length including the full body of the phantom, the resulting image set contained 2,632 images and any further changes resulted in an image set that was greater than the limit.

After the images were acquired, the motion amplitude data with timestamps were exported from the RPM system and the cine images were transferred to MIM software (MIM Software Inc., Cleveland, OH). Using MIM, the cine images were binned according to the motion data, which

resulted in a 4D image set, and the cine file was removed from the MIM server and stored externally. Amplitude-based binning was employed to bin the 4D images.

2.1.4. Treatment Planning

The time-weighted average intensity projection (AIP) image was exported from MIM to the Pinnacle3 treatment planning system. The average intensity projection image has been shown be less prone to image artefacts than free-breathe CT, while being nearly equivalent dosimetrically to the free-breathe CT (Tian, et al. 2012). For this reason, we used the AIP image of the phantom for computing our static treatment plans. Each patient's clinical lung SBRT VMAT beams were retrieved from the MOSAIQ record and verify system (Elekta AB, Stockholm, Sweden) as a text file containing each beam's control points. A VMAT beam consists of many control points (usually 50+) along the arc traced by the gantry rotation; at each of these points the beam shape, machine output, gantry orientation, etc., are specified. Control points were manually imported using the scripting interface within the Pinnacle3 treatment planning system.

Using the known geometry of the Quasar phantom, in which the center of the tumor is 80 mm lateral to the center of the phantom, the isocenter was manually and consistently set. The treatment isocenter was consistently placed at 0 mm in the superior-inferior direction, and 80 mm laterally. For left-lung beams, +80 mm was used; for right-lung beams, -80 mm. The couch was removed from the dose computation. Finally, the dose grid was specified with resolution 2mm x 2mm x 2mm. For consistency between plans, a script was used to set the isocenter, remove the couch, and define the dose grid. Dose was computed using the Pinnacle3 Adaptive Convolve algorithm.

Due to geometrical differences between the real patients and the phantom, the computed dose distributions within the phantom did not exactly match the planned dose distributions within

the real patients. Specifically, the dose distributions within the target volume (PTV) may contain hot and cold spots and the dose falloff regions may be present within the PTV, due to the phantom geometry. Thus, the plans may be systematically less representative of the moving target dose because motion effects may be exaggerated due to the spherical tumor moving through the dose heterogeneities. However, this is advantageous in assessing the accuracy of the 4D dose reconstruction, as the likelihood of motion-related dose variance is increased while the mechanical delivery conditions of clinical SBRT are preserved.

2.2. Treatment Delivery and Reconstruction of Moving Target Dose

2.2.1. Treatment Delivery Experimental Setup

Figure 2.4 presents the experimental setup for treatment delivery to the phantom.

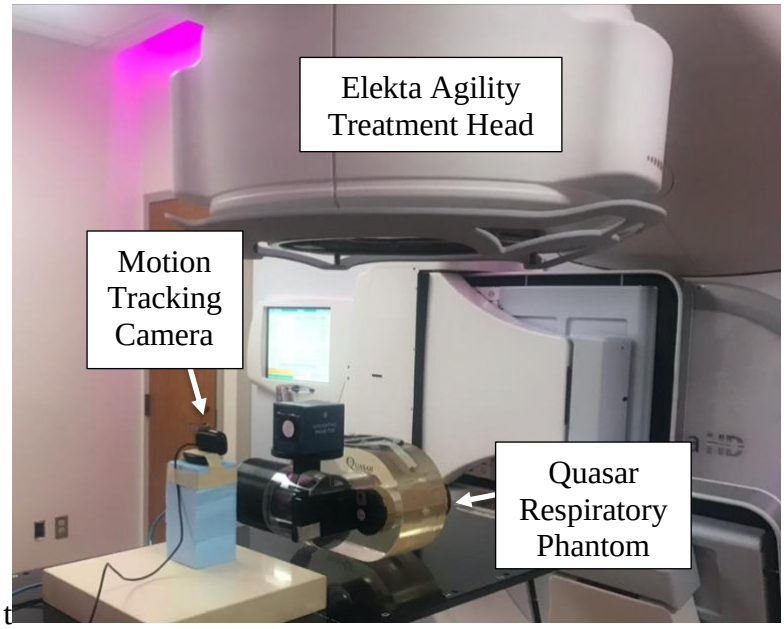

t

Figure 2.4. Experimental setup for beam delivery to phantom.

For each trial in the study, radiochromic film was cut so that it fit within the cylindrical Quasar phantom lung insert. The radiochromic film was used to measure dose to the moving target. CT-visible markers were placed on the film for registration with the CT coordinate system. Next, the cylinder was placed back inside the acrylic body of the phantom and the stage was set to its

home position. The phantom was controlled using the Quasar Respiratory Motion Software, which was set to produce the desired respiratory amplitude for each patient. Motion was tracked using the in-house external surrogate tracking camera system. Beams were delivered using an Elekta Versa HD linear accelerator with Agility treatment head (80 MLCs per bank) (Elekta AB, Stockholm, Sweden). After the beams were delivered, a CT scan of the phantom was taken to get the CT coordinates upon which to register the film.

2.2.2. Treatment Delivery Log File

During treatment, a delivery log file is written in real time at a sampling rate of 4 Hz. This file contains beam information as a function of time, such as monitor units, gantry angle, and MLC positions. Following each treatment delivery, log files were retrieved from Mobius Log software (Elekta AB, Stockholm, Sweden) which returns the log files from the linac control system via a local network connection. While the timestamps recorded in the logfile are relative to the starting time, the header information of the log file contains the datetime string of the first timestamp, and thus the true time of each row of logfile data could be determined. The synchronization of the log file timestamp with the respiratory trace was verified.

2.2.3. In-House External Surrogate Tracking System for Treatment Vault

The platform of the Quasar phantom moves up and down (anterior-posterior direction) with the forward and backward (superior-inferior) motion of the cylindrical lung insert. This motion is 1:1; that is, 1 cm of movement of the cylindrical lung insert translates to 1 cm of platform movement. Thus, for our trials with only 5 mm of total motion, the platform and therefore our surrogate marker only moves 5 mm. This necessitated a camera system which was reliable yet inexpensive, since the camera would need to be placed very close to the radiation field to capture a usable signal. We used a Logitech C270 webcam, which outputs 720p video at a framerate of 30

Hz, for our tracking purposes. Each frame of the live video feed was used to track the center of a circle using in-house Python code. To initiate tracking, the user was able to click within the circle. This click location was used as a guess to compute the center of the circle. The computed (x, y) center was used as the guess for the next frame. This method was found to be stable for the external marker motion speeds studied in this project.

2.2.4. Verification of Log File Synchronization with Camera

To partition log file data using motion data from our in-house system, it was necessary to verify that the timestamps recorded in the log file were synchronized with the timestamps returned by our motion tracking code. This was accomplished by tracking the gantry angle with our motion tracking system during treatment delivery and comparing the tracked gantry angle to the recorded gantry angle in the log file at each timestamp. A white circle with black background was taped to the false wall which rotates with the linac. The camera system was initialized to track the circle on the wall as the gantry rotated during beam delivery. Using the x, y coordinates of the trace of the gantry, the gantry angle was computed. Cross-correlation was used to determine whether any time shift existed between the computed and tracked gantry angles.

2.2.5. Log File Partitioning

Log files from the linear accelerator were overlaid with respiratory tracking data taken from the in-house webcam system. First, due to the limited resolution of the camera, a sin6 wave was fit to the data using the peaks of the respiratory signal, which were found to be the most reliable feature. The fit wave was normalized to the range [0, 1]. Next, the amplitude targets were copied from the MIM 4D-CT binning settings. The amplitude targets used in this study were 0.0, 0.2, 0.4, 0.6, 0.8, 1.0, where 0.0 represents the lowest point of the wave and 1.0 represents the wave's highest point. Amplitude targets are shown in Figure 2.5.

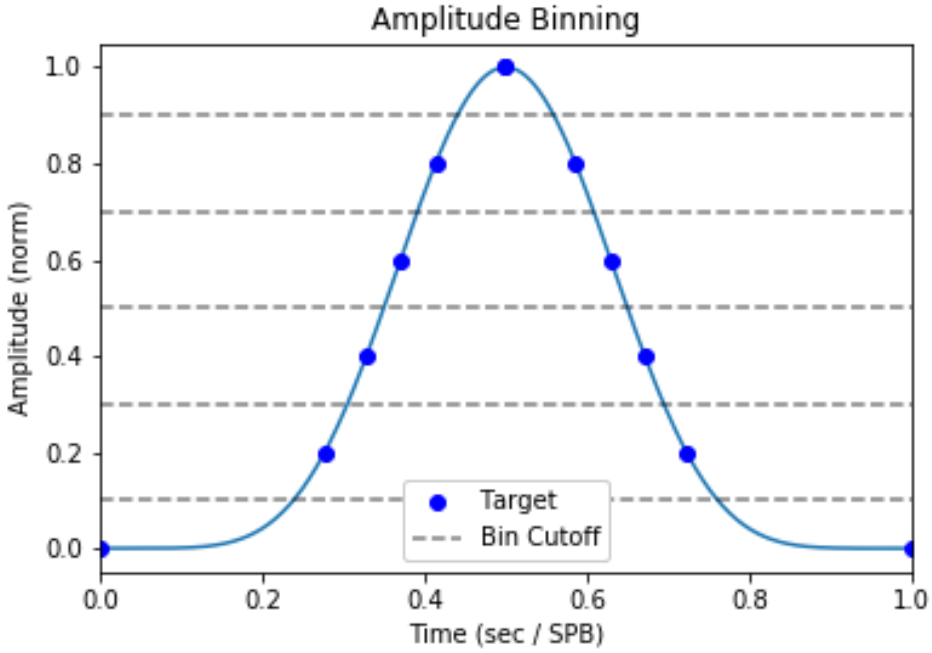

Figure 2.5. Amplitude binning targets for log file partitioning.

Next, the time at which each amplitude cutoff occurred was determined using linear interpolation. After bin cutoff times were computed, log files were partitioned using the cutoff times as dividing points. Each log file partition (log file data falling between sequential cutoff times) was written to a temporary text file with the filename indicating the amplitude bin and partition number within that bin. Since the sampling rates of the amplitude data and log file data were asynchronous, linear interpolation was used to find the log file data values at the cutoff times. These interpolated values were included in the partitions. In-house Python code was used to convert the log file partitions into static beams within the Pinnacle^3 treatment planning system using the Pinnacle^3 scripting interface.

For a log file partition containing N rows (with a maximum of 2 interpolated rows of data and minimum of $N-2$ rows of non-interpolated data from the log file), the number of static beams written for that log file partition was $N-1$. More specifically, each static beam written to the

import script was a composite of the ith- and ith + 1 row of the log file partition, P_i and P_{i+1}; scripted static beam parameters T_i, such as gantry angle, collimator angle, etc., with the exception of the beam output (MU), for the ith static beam were assigned by taking the average:

$$T_i = \frac{P_i + P_{i+1}}{2} \tag{2.2}$$

Each amplitude bin was assigned a specified number of monitor units, MU_{bin} which was computed using

$$MU_{\text{bin}} = \sum_{j=1}^{M} \sum_{i=1}^{N-1} (MU_{i+1,j} - MU_{i,j}) \tag{2.3}$$

where i, j represent the indices of the row (of N rows) inside the partition, and partition (of M partitions) inside the amplitude bin, respectively. The weight $w_{i,j}$ of each scripted beam was taken to be the monitor units (MU) delivered from the ith to the ith + 1 row of the partition, divided by the total MU for that amplitude bin,

$$w_{i,j} = \frac{MU_{i+1,j} - MU_{i,j}}{MU_{\text{bin}}} \tag{2.4}$$

Importantly, the sum of all weights for a given amplitude bin is unity,

$$\sum_{j=1}^{M} \sum_{i=1}^{N-1} w_{i,j} = 1 \tag{2.5}$$

A visualization of the log file partitioning process is presented in Figure 2.6.

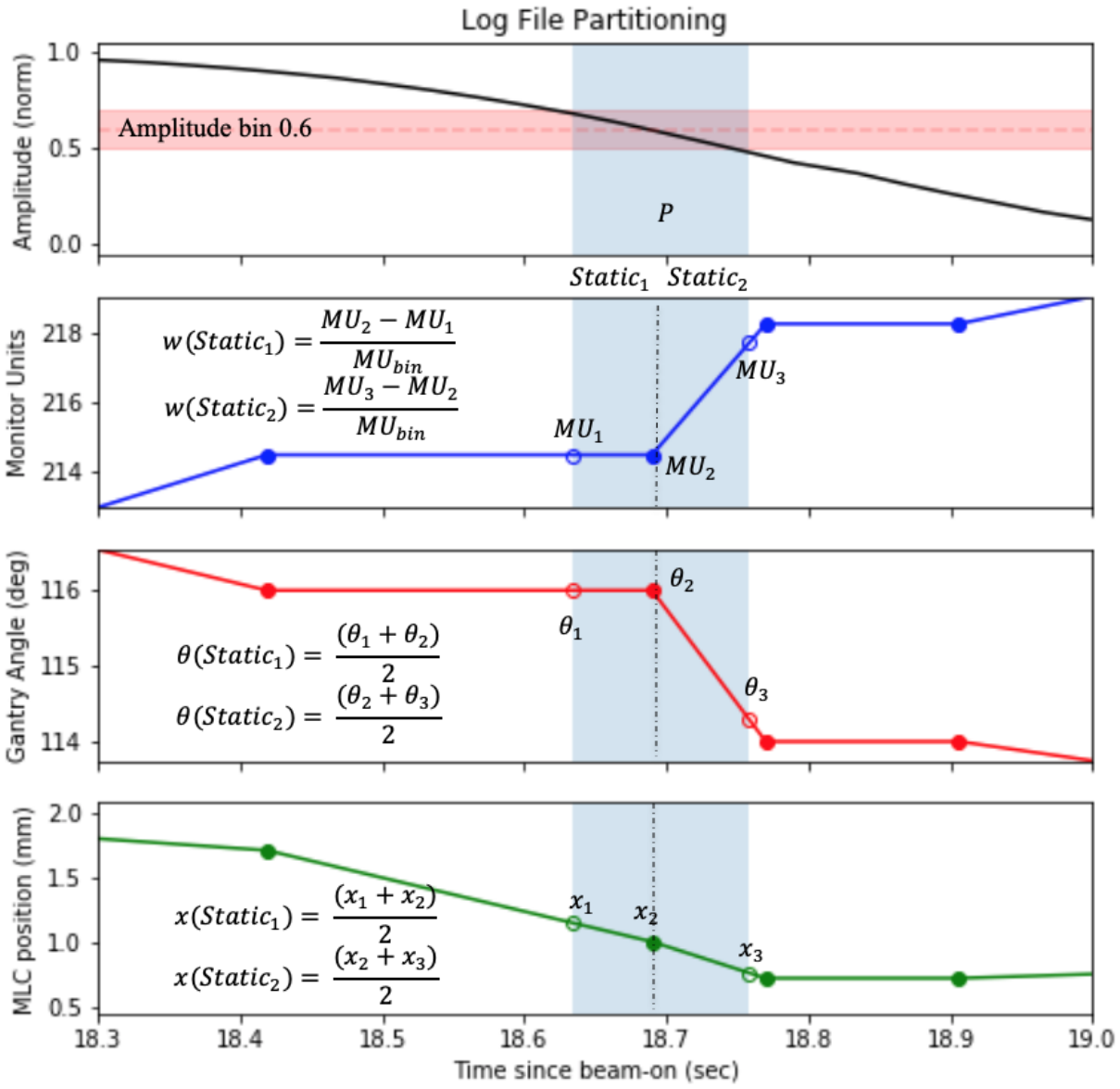

Figure 2.6. Log file partitioning visualization. The blue vertical shaded region indicates the log file partition P within the 0.6 amplitude bin, with the red horizontal shaded region indicating the amplitude position target (in this case, 0.6) and the cutoff values of the bin (0.5, 0.7). Filled circles correspond to log file data points, while the unfilled circles correspond to linearly interpolated points. $Static_1$ and $Static_2$ correspond to the two static beams which are elements of P. Symbols θ and x correspond to the gantry angle and example MLC position, respectively.

2.2.6. Deformable Dose Accumulation

Image registration, the process of mapping corresponding points between images, has become ubiquitous in radiation therapy. There are two main types of image registration algorithms; (1) rigid and (2) deformable image registration (DIR). Rigid registrations can be defined by a linear transformation (e.g., rotation, translation) from a source image to a target image, in which there is no deformation of the underlying image grid. An example application of rigid registration is daily patient alignment using the on-board cone-beam CT prior to radiation treatment delivery. The patient is scanned using the on-board imager, and the resultant images are aligned with the patient's planning CT scan to compute necessary table shifts and ensure consistent patient alignment from one treatment fraction to the next. An example application of DIR, especially relevant to this work, is the deformable registration from 4D-CT phase images to a reference phase. During breathing motion, the patient remains stationary but the internal anatomy changes by stretching and contracting. DIR allows a vector map to be drawn from corresponding points in one phase image (the source) to another phase image (the target). The source image (i.e., where the vector field mapping voxels from one image to another starts) is referred to in this work as the 'secondary image'. The target image (i.e., where the vectors point) is referred to as the 'primary image'.

A review of DIR algorithms for dose accumulation has been published by Chetty and Rosu-Bubulac (Chetty and Rosu-Bubulac 2019). In their review, the two major types of deformable registration algorithms are described, which are spline-based and free form algorithms. Spline-based algorithms use features of the image to define control points and use spline functions to map correspondences between those points. Free form algorithms, in contrast, allow the vectors for each secondary image voxel to map freely to any voxel in the primary image. MIM v.9.6. provides

a proprietary free-form DIR algorithm which attempts to find the most physically realistic mapping for each voxel (Calusi, et al. 2019). The MIM DIR algorithm was used in this study.

Deformable dose accumulation is an application of DIR where dose values from the dose grid of the secondary image follow the vector map to the corresponding grid points on the primary image. We applied deformable dose accumulation in MIM software to map computed doses from each amplitude position bin image to our reference position image. The reference position image was defined to be at the time-weighted average position of the phantom lung insert during treatment. Figure 2.7 presents the workflow used to deform log file partition doses onto the reference image geometry.

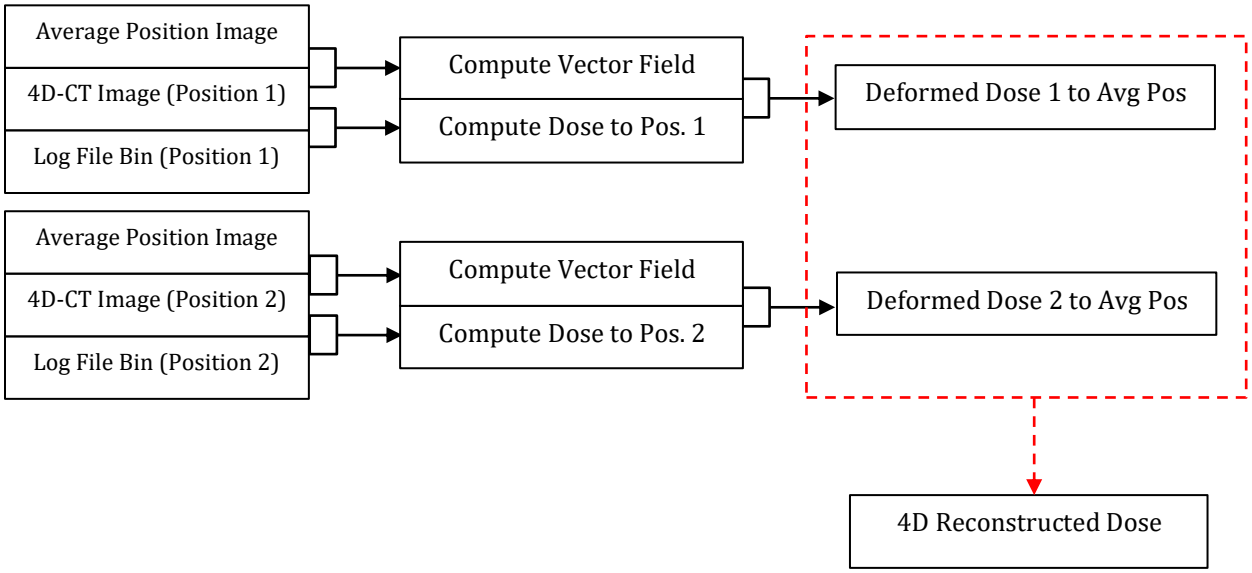

Figure 2.7. Flowchart of deformable dose accumulation. For simplicity, only two positions are shown; however, in practice we accumulated dose over all 6 position bins. Red dashed box indicates dose accumulation on the time-weighted average position geometry.

2.2.7. Validation of Deformable Dose Accumulation

The combination of 4D-CT images of the Quasar phantom with the binned log file data allowed us to reconstruct the beam apertures occurring at each tumor position. Thus, 4D dose accumulation allows the computation of the delivered dose to the moving tumor which takes into

account the interplay effect. To test our deformable dose accumulation method, we created an IMRT Step-N-Shoot treatment plan which forced interplay effect to occur, delivered this plan to the Quasar phantom, measured the dose delivered to the moving target, and compared our measured moving-target dose with the 4D log file-based deformable dose accumulation. The IMRT Step-N-Shoot plan forced interplay using an aperture, approximately the size of the tumor, which moved aperiodically along the tumor's principle axis of motion. Since the sine6 wave is periodic, the aperiodic nature of the aperture position over time guaranteed that interplay (i.e., destructive interference) between the two motion patterns would occur.

2.3. Radiochromic Film Dosimetry

2.3.1. Radiochromic Film Calibration

Radiochromic film is a passive, integrating dosimeter with high spatial resolution that is nearly tissue equivalent. It is widely used over radiographic film due to its self-processing and insensitivity to ambient light (Devic, et al. 2016). Gafchromic EBT3 radiochromic film (Ashland, Wilmington, DE) was used (Lot #: 05161905) for our film measurements. A cross-sectional diagram of Gafchromic EBT3 film is presented in Figure 2.8.

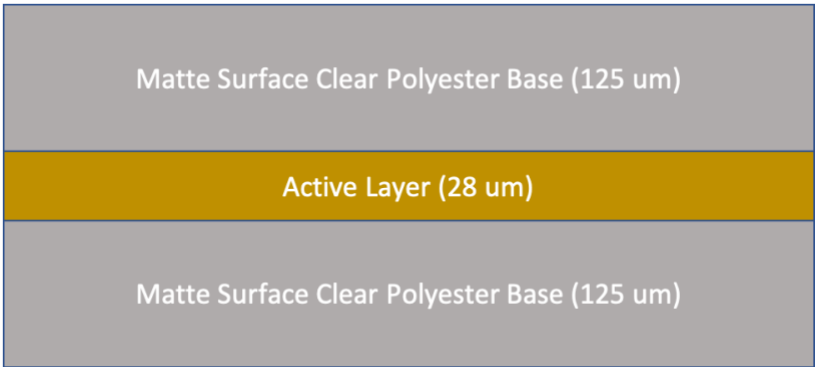

Figure 2.8. Cross-section of Gafchromic EBT3 film (Ashland 2020).

Radiochromic film changes color when radiation dose is absorbed in it due to polymer reactions caused by the radiation interacting within the film's active layer. The color pixel values

of scanned radiochromic film images are calibrated with absorbed dose so that radiochromic film may be used for relative dosimetry. The dose response range of radiochromic film is up to 4000 cGy (Casanova Borca, et al. 2013). Our calibration included 14 points, which ranged from 0 cGy to 3000 cGy. The calibration doses used were 0, 125, 250, 375, 500, 625, 750, 875, 1000, 1250, 1500, 2000, 2250, and 2500 cGy.

For each calibration point, a small (minimum 3 cm x 3 cm) rectangular section of film was cut placed at reference depth under reference conditions. For our clinic, reference depth was 10 cm, and reference conditions included 10 cm backscatter, a 10cm x 10cm field size at isocenter, and 90 cm source-to-surface distance (SSD). Each calibration film was placed at the center of the square field. Solid water phantoms were used to create these reference conditions. Given these reference conditions, the equation (Gibbons, et al. 2014) relating dose D to machine output (monitor units, MU), for the central axis reduces to

$$MU = \frac{D}{\dot{D}_0} \tag{2.6}$$

where $\dot{D}_0$ = 0.8 cGy / MU for 6 MV photons at our institution. This equation was used to convert our known calibration doses into the MU setting in the linac control system for each calibration film.

Calibration films were scanned >24h after exposure using an Epson Expression 10000XL document scanner, following the recommendations of AAPM TG 55 (Niroomand-Rad, et al. 1998). Care was taken to ensure consistent orientation of the film, which was essential to mitigate the effect of light polarization on the computed optical density (Perez Azorin, et al. 2016). Prior to scanning film, a minimum of 10 warmup scans were run to ensure that the scanner operating temperature was level. Table 2.3 presents the scanner settings used for our film digitization.

Table 2.3. Film digitization parameters (Epson Scan Software).

Parameter	Setting
Mode	Professional
Resolution	150 dpi
Image Type	48-bit color
Document Type	Film
Save Format	TIFF

Film images were saved in tagged-image file format (TIFF). Next, the mean pixel values for the red, green, and blue channels were found for each of the calibration films using a rectangular selection window. These pixel values PV were converted into optical density OD using the formula

$$OD = -\log_{10}\left(\frac{PV}{2^{16}-1}\right) \tag{2.7}$$

where 2^{16}- 1 represents the maximum pixel value for each color channel given the 48-bit color setting (16 bits per color channel). A rational fit function was used to calibrate absorbed dose to optical density as recommended by the manufacturer,

$$OD(x) = -\log_{10}\left(A + \frac{B}{(x+C)}\right) \tag{2.8}$$

where x is the absorbed dose, and A, B, and C are the fit coefficients. The red, green, and blue color channels of the film image were calibrated independently. A piecewise fit function was utilized to accommodate the large dose range following a previously published methodology (Morrison, et al. 2014). To implement this piecewise function, the OD for each fit curve (Red, Green, and Blue) corresponding to the median dose over the whole range was determined and set to be the cutoff point for its respective color channel. To ensure a smooth function at the cutoff point, fit curves included the calibration doses immediately surrounding the cutoff point. Figure 2.9 presents the film densitometric curve used for calibration.

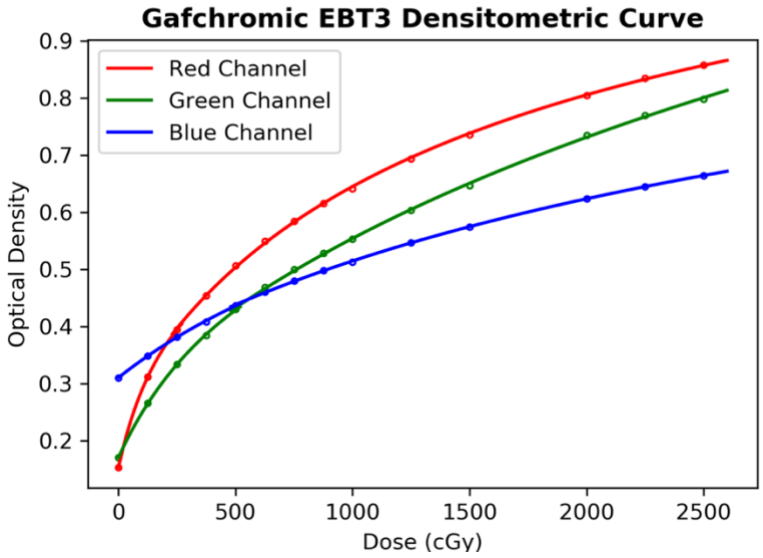

Figure 2.9. Gafchromic EBT3 film densitometric calibration curve.

2.3.2. Radiochromic Film Image Processing

Radiochromic film does not have an inherent coordinate system that can be directly linked to any CT image. Therefore, it was essential to register the film to a reference DICOM coordinate system. To register the film, we used a point-based registration method. Consider two points (A, B) on the film and corresponding CT coordinates (A_{CT}, B_{CT}). First, the pixel coordinates of points A and B were determined on each film image. Next, each film image was rotated so that the line passing through (A, B) was parallel to the line passing through (A_{CT}, B_{CT}). Finally, the film coordinates were scaled and translated to match those of the CT to complete the rigid registration. After the linear transformation for the registration was solved, each film image was denoised using a median filter (5 px window), and then downsampled using a bilinear interpolation to a 1 mm x 1 mm grid.

2.4. Data Analysis

2.4.1. Gamma Analysis

Gamma analysis provides a comparison between two dose distributions that takes into account both dosimetric and geometric information to determine agreement (Low, et al. 1998). Gamma analysis is performed by computing gamma indices at each point in a dose distribution. The gamma value was defined by Low et al. as:

$$\Gamma(r_m, r_c) = \sqrt{\frac{r^2(r_m, r_c)}{\Delta d_m^2} + \frac{\delta^2(r_m, r_c)}{\Delta D_M^2}} \tag{2.9}$$

where $\delta(r_m, r_c)$ is the dose difference between the measured dose at r_m and the calculated dose at r_c, $r(r_m, r_c)$ is the Euclidean distance between r_m and r_c, Δd_m is the distance-to-agreement criterion, and ΔD_M is the dose agreement criterion. Given a point i, j in the reference dose, the gamma index is defined by Low et al., as

$$\gamma(r_m) = \min\{\Gamma(r_m, r_c)\} \forall \{r_c\} \tag{2.10}$$

Gamma analysis is used clinically as a metric by which to assess the deliverability of IMRT and VMAT plans. The Report of the American Association of Physicists in Medicine (AAPM) Task Group (TG) 218 recommends a distance-to-agreement of 2mm and a dose agreement value of 3% of maximum dose with a lower threshold of 10% of maximum dose (Miften, et al. 2018). Only reference dose points with dose values above the threshold are considered in the gamma analysis. According to the AAPM TG 218 recommendations, treatment plans are considered to pass if their gamma passing rate (GPR), or the number of gamma indices with value less than one divided by the total number of points for which gamma was computed, is greater than 90%.

2.4.2. Modulation Complexity Score

The modulation complexity score (MCS) was originally proposed by McNiven, et al. for Step-N-Shoot IMRT plans (McNiven, et al. 2010). The MCS is defined between 0 and 1 and approaches 0 as plan complexity increases. Plan complexity is computed using both the MLC leaf sequence variability, which is a measure of the amount of MLC leaf motion during the plan, and the aperture area variability, which is a measure of how much the aperture formed by the MLC changes during the treatment. Masi, et al. modified the MCS to work with the continuous arcs of VMAT, with the modified version called MCSv (Masi, et al. 2013).

Chapter 3. Results

3.1. Verification of Log File Synchronization with Camera

The synchronization of timestamps from the log file and camera tracking system was verified by tracking the gantry angle during a VMAT SBRT treatment. The tracked gantry angle is plotted in Figure 3.1 with the log file record of the gantry angle during the treatment.

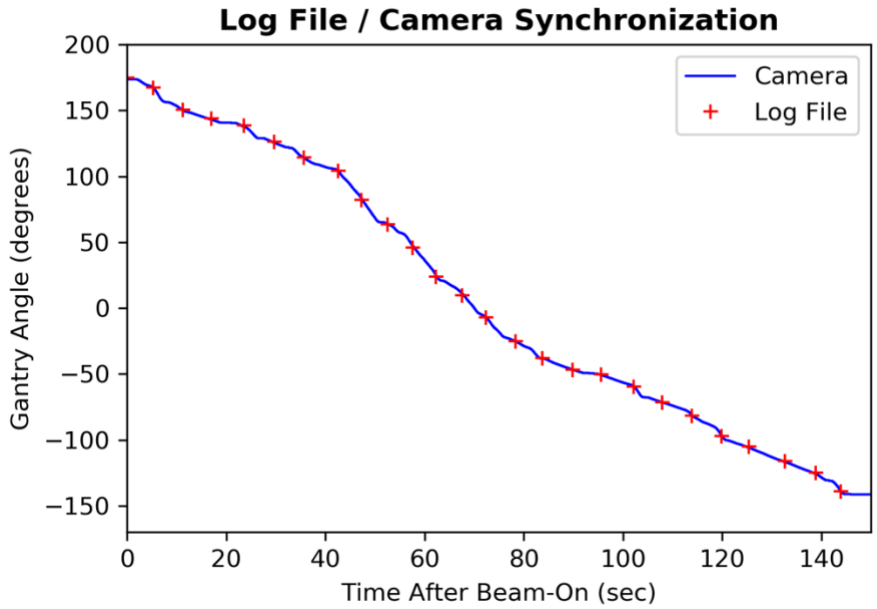

Figure 3.1. Comparison of tracked and log file record gantry angles. Measurement using camera system under same conditions as respiratory tracking.

Visual inspection of Figure 3.1 suggests that no time shift is necessary between the two sets of timestamps. To verify, cross correlation of the tracked and log file-recorded gantry angles indicated that the agreement between the time series was maximized with no time shift applied. From this result, we conclude that the absolute timestamps returned by the log file were synchronized with the camera system used during this study, and that it is valid to overlay the log file with the tracked respiratory data with no time delay between the two clocks.

3.2. Verification of Deformable Dose Accumulation

The results of the verification of our deformable dose accumulation method to detect forced dose errors due to interplay are shown in Figures 3.2 and 3.3. The dose profiles are displayed with extent-of-motion (MIP Extent). It was found that the 4D accumulation method performed well within the MIP extent, indicated by the agreement between the 4D reconstruction (solid line) and film measurement (dotted line). However, outside the tumor motion extent the 4D reconstruction breaks down. This can be seen by the divergence of the film from the 4D reconstruction in both the 6 and 12 SPB cases of this validation work (Figure 3.2 and Figure 3.3, respectively). These results indicate that the 4D reconstruction detects known dose errors due to interplay. For comparison, the profiles of the treatment plan and static film measurement are also shown.

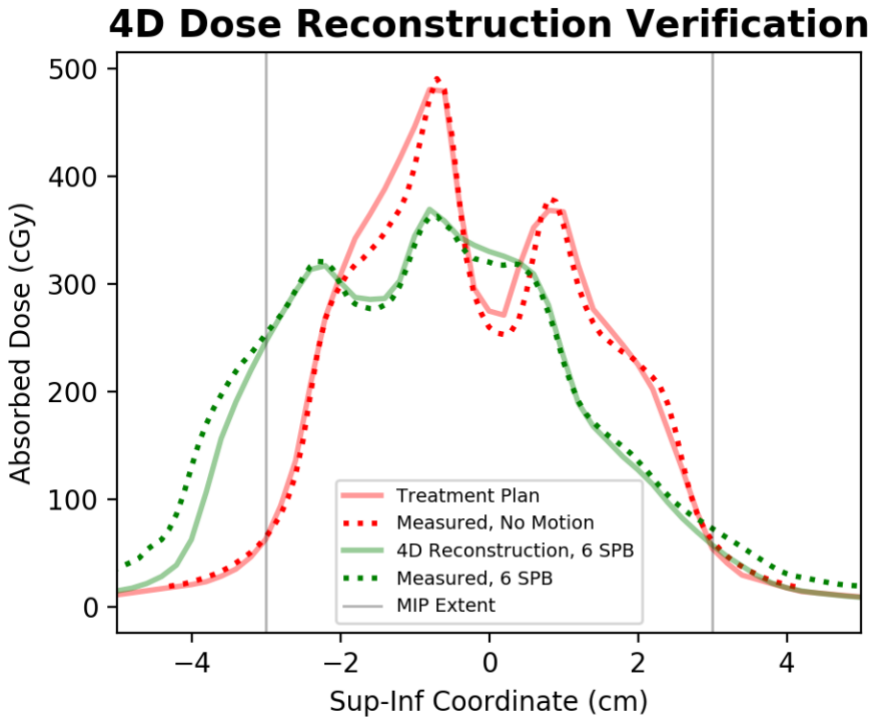

Figure 3.2. Superior-inferior dose profiles along principle axis of motion for validation case, 6 SPB.

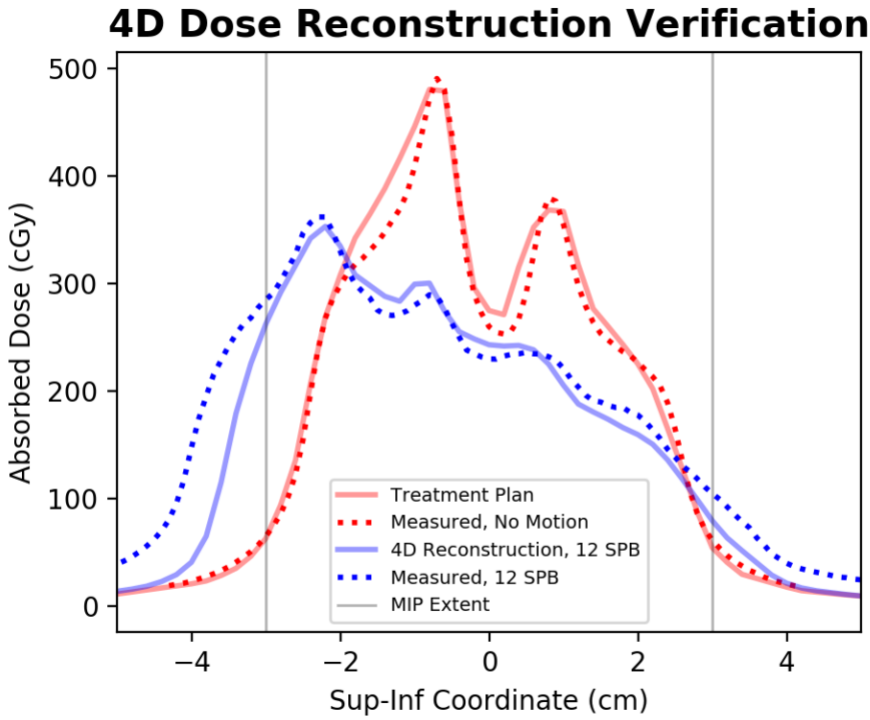

Figure 3.3. Superior-inferior dose profiles along principle axis of motion for validation case, 12 SPB.

3.3. Gamma Analysis of 4D Reconstructions with Treatment Plans

Gamma analysis was used to compare the 3 and 6 SPB 4D reconstructions with the corresponding treatment plans, which were planned on the time-weighted average intensity projection images (AIP). Table 3.1. presents the results for the gamma analysis, along with plan metrics such as MU and MCSv for reference. In our gamma analysis, AAPM TG 218-recommendations of 3% dose agreement and 2mm distance-to-agreement were implemented. Values are presented for gamma calculations incorporating both a 10% and 50% threshold of maximum dose. Above this threshold, gamma values were computed. The 50% threshold provides an analysis of the agreement within the higher dose region; large differences between the 10% and 50% gamma passing rate indicate dose variance in the high dose region.

Table 3.1. Gamma analysis of 4D dose reconstructions at 10% and 50% thresholds (T) compared with static treatment plans for 3- and 6- SPB, with corresponding plan MU and VMAT modulation complexity score (MCSv). * indicates selection for further analysis in next section.

Patient Number	Motion (mm)	GPR 4D vs. Plan (global 3%, 2mm)				MU	MCSv
		3 SPB	6 SPB	3 SPB	6 SPB		
		T=10%	T=10%	T=50%	T=50%		
1*	5	100	99.9	100	99.5	1808	0.363
2	6	100	100	100	100	2648	0.358
3	12	99.6	100	98.6	100	3033	0.482
4*	15	98.2	98.5	93.8	94.8	1425	0.471
5*	15	96.8	97.1	91	91.9	2319	0.326
6*	9	98.6	97.9	94.5	92.1	2556	0.353
7	8	100	100	100	100	2209	0.485
8	9	99.4	99.7	97.8	98.8	2243	0.389
9	6	100	100	100	100	2903	0.234
10*	5	94.1	94.7	80.8	82.7	3883	0.250
11	9	100	100	100	100	2581	0.428
12	8	100	100	100	100	2171	0.476
Mean	8.9	98.9	99	96.4	96.7	2481.6	0.385
St. Dev.	3.5	1.8	1.7	5.8	5.4	626.2	0.087

No statistically significant difference was found between the 3 and 6 SPB gamma passing rates, using criteria 3%, 2mm was found at either dose threshold.

3.4. Comparison of Selected Patients with Film Measurement

Based on the gamma analysis results of the 4D reconstructions with the treatment plans, we found that plans for Patients 4, 5, 6, and 10 were associated the largest dose differences within the high dose region. In this section, we compare the selected patients' 4D reconstructions and treatment plans with film measurement to determine if the 4D reconstructions are in closer agreement (higher GPR) than the treatment plans. For contrast, Patient 1 is also shown as an example case in which the 4D reconstruction closely matches the treatment plan.

3.4.1. Patient 1

We found good agreement between the 4D log file-based dose reconstruction and the planned dose distribution for Patient 1, which are presented in Figure 3.4 and Figure 3.5 for the 3 and 6 SPB cases, respectively.

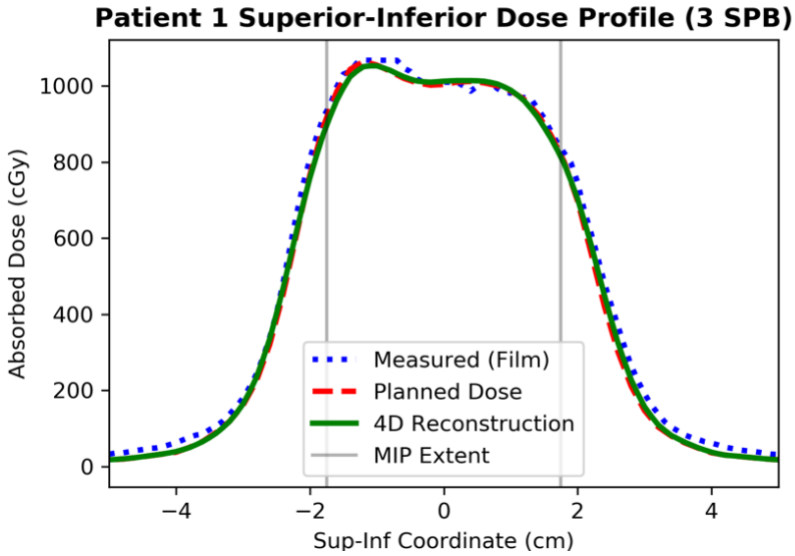

Figure 3.4. Superior-inferior dose profile for Patient 1 with breathing rate of 3 SPB.

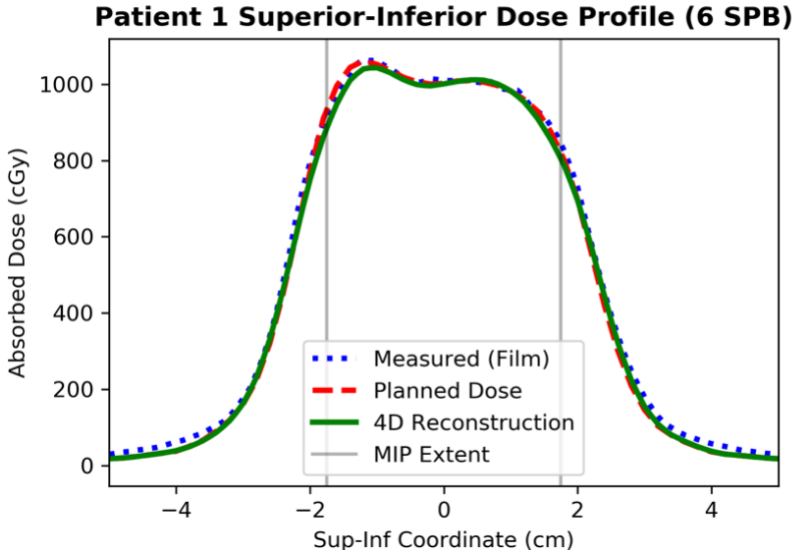

Figure 3.5. Superior-inferior dose profile for Patient 1 with breathing rate of 6 SPB.

These profiles correspond to gamma passing rates of 99%-100% between the 4D-reconstruction (green solid profile) and treatment plan (red dashed profile) using gamma criteria 3% and 2mm. The measured dose profile (film) is plotted for comparison, and we found little visible difference between the measured distribution with film and either of the calculated distributions. This corresponds to a MCSv of 0.363 and low motion amplitude of 5mm.

Gamma maps are presented in Figure 3.6 and Figure 3.7 for the 3 and 6 SPB cases, respectively, for Patient 1. To aid in interpretation of the gamma passing and failing points, isodose lines for 70% and 85% of max film measured dose are plotted with the gamma maps. Only values within the MIP extent are included in the gamma calculation because of our finding that the 4D reconstruction breaks down outside of the MIP extent.

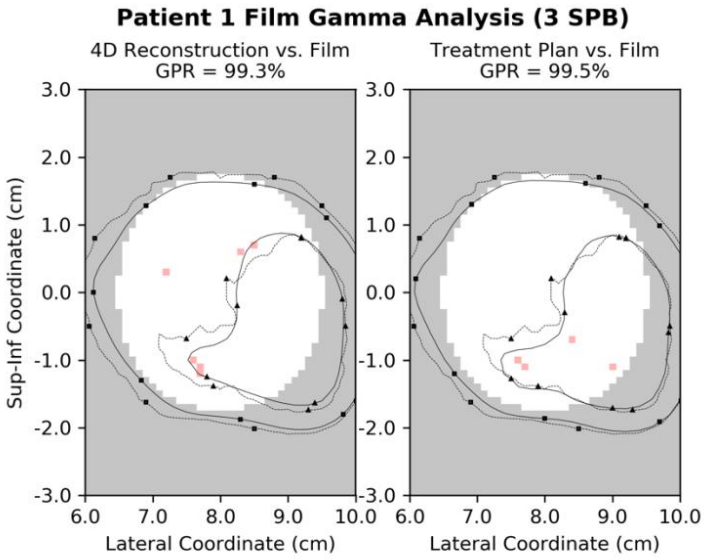

Figure 3.6. Gamma map (global 3%, 2mm) for 4D reconstruction and treatment plan vs. film measurement, within MIP extent, for Patient 1 with breathing rate 3 SPB. Color legend: (Gray: Point not included in calculation; White: Passing point; Red: Failing point. Circle and square markers indicate 70% and 85% isodose contour and dashed and solid lines indicate film and calculated dose, respectively.

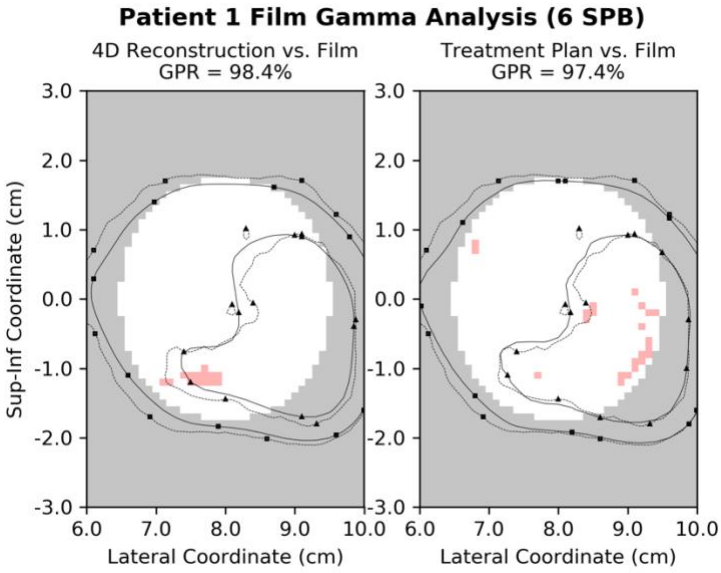

Figure 3.7. Gamma map (global 3%, 2mm) for 4D reconstruction and treatment plan vs. film measurement, within MIP extent, for Patient 1 with breathing rate 6 SPB. Color legend: Gray: Point not included in calculation; White: Passing point; Red: Failing point. Circle and square markers indicate 70% and 85% isodose contour. Dashed and solid lines indicate film and calculated dose, respectively.

3.4.2. Patient 4

The measured (film), 4D reconstruction, and planned dose distributions are plotted for Patient 4 in Figures 3.8 and 3.9. Patient 4 was associated with gamma passing rates of 93.8% (3 SPB) and 94.8% (6 SPB) between the 4D reconstruction and treatment plan as shown in Table 3.1. The amplitude of motion for Patient 4 was 15 mm (the highest we studied), and the complexity score was 0.471, indicating low plan complexity. Within the MIP extent (ITV contour), the 4D dose reconstruction was found to be in better agreement with film measurement than the treatment plan. This is within the MIP extent where the 4D reconstruction method was verified. The deviation between 2 and 4 cm may be due to the gradient effect (‘smearing’) on the measured dose distribution from the large motion amplitude.

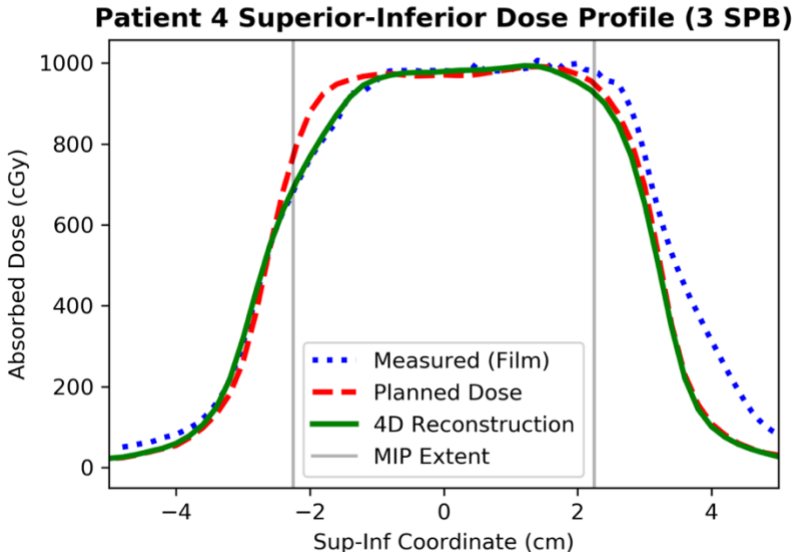

Figure 3.8. Superior-inferior profile for Patient 4 with breathing rate of 3 SPB.

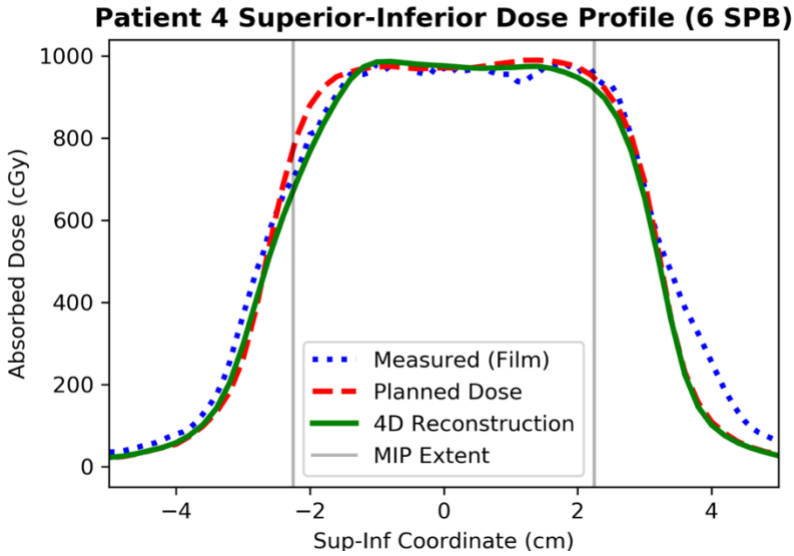

Figure 3.9. Superior-inferior profile for Patient 4 with breathing rate of 6 SPB.

A possible reason that the 4D log file-based dose calculation did not reflect this is the breakdown of the 4D deformable registration method outside of the MIP extent, beyond which the deformable image registration algorithm lacks sufficient information to accurately map voxels. Gamma maps for the 3 and 6 SPB measurements for Patient 4 are presented in Figures 3.10 and 3.11, respectively.

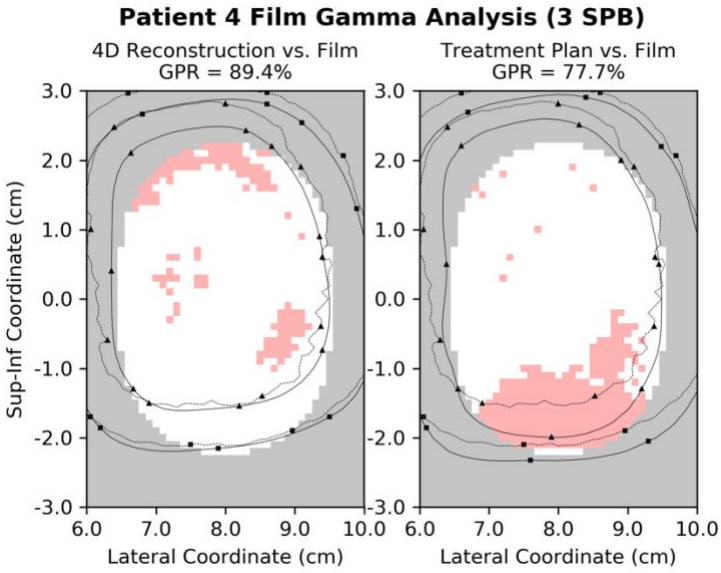

Figure 3.10. Gamma map (global 3%, 2mm) for 4D reconstruction and treatment plan vs. film measurement, within MIP extent, for Patient 4 with breathing rate 3 SPB. Color legend: Gray: Point not included in calculation; White: Passing point; Red: Failing point. Circle and square markers indicate 70% and 85% isodose contour. Dashed and solid lines indicate film and calculated dose, respectively.

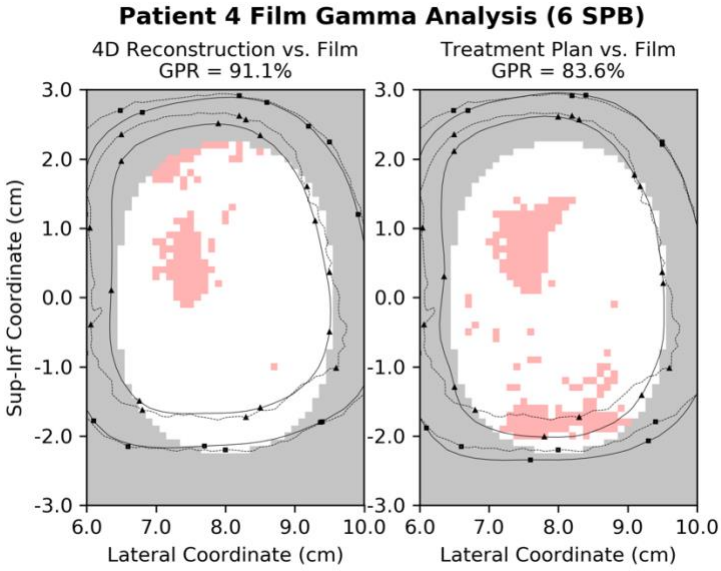

Figure 3.11. Gamma map (global 3%, 2mm) for 4D reconstruction and treatment plan vs. film measurement, within MIP extent, for Patient 4 with breathing rate 6 SPB. Color legend: Gray: Point not included in calculation; White: Passing point; Red: Failing point. Circle and square markers indicate 70% and 85% isodose contour. Dashed and solid lines indicate film and calculated dose, respectively.

3.4.3. Patient 5

Profiles for the 3 and 6 SPB measurements for Patient 5 are presented in Figure 3.12 and Figure 3.13, respectively. Profile assessment of Patient 5 along the principle axis of motion resulted in similar regions of agreement and of failure of the 4D reconstruction to Patient 4.

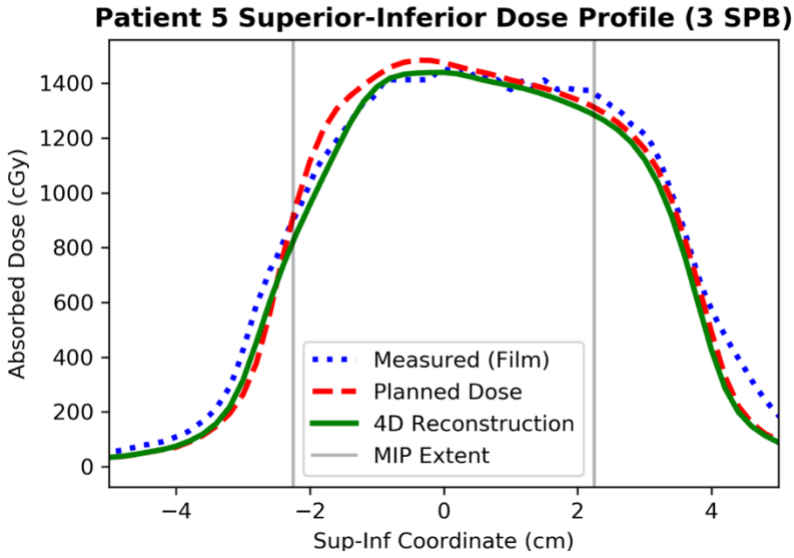

Figure 3.12. Superior-inferior dose profile for Patient 5 with breathing rate of 3 SPB.

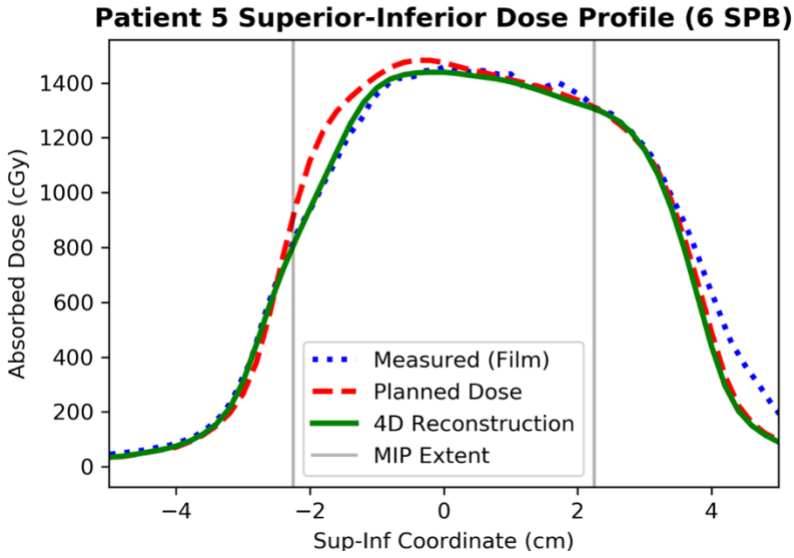

Figure 3.13. Superior-inferior dose profile for Patient 5 with breathing rate of 6 SPB.

Gamma maps comparing the 4D reconstructions and treatment plan for Patient 5 to the 3 and 6 SPB film measurements are presented in Figure 3.14 and Figure 3.15.

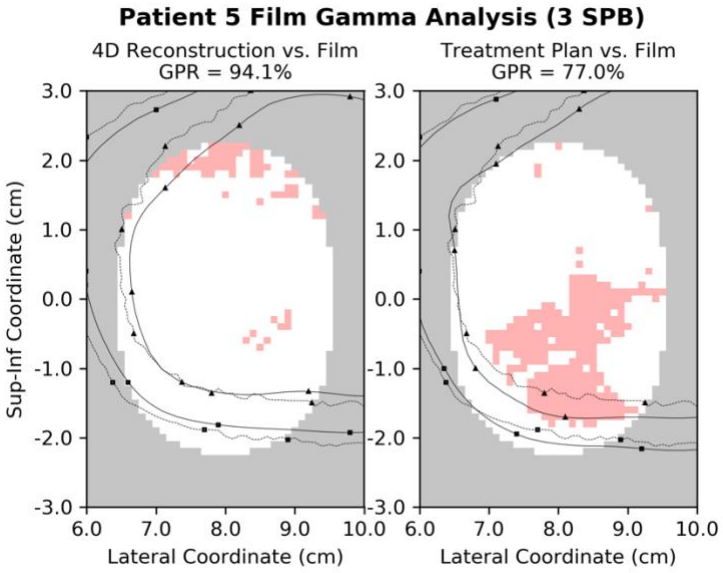

Figure 3.14. Gamma map (global 3%, 2mm) for 4D reconstruction and treatment plan vs. film measurement, within MIP extent, for Patient 5 with breathing rate 6 SPB. Color legend: Gray: Point not included in calculation; White: Passing point; Red: Failing point. Circle and square markers indicate 70% and 85% isodose contour. Dashed and solid lines indicate film and calculated dose, respectively.

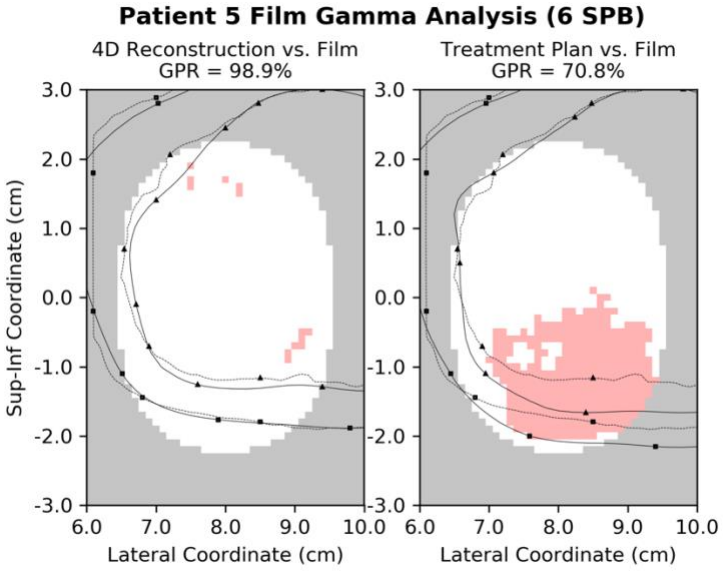

Figure 3.15. Gamma map (global 3%, 2mm) for 4D reconstruction and treatment plan vs. film measurement, within MIP extent, for Patient 5 with breathing rate 6 SPB. Color legend: Gray: Point not included in calculation; White: Passing point; Red: Failing point. Circle and square markers indicate 70% and 85% isodose contour. Dashed and solid lines indicate film and calculated dose, respectively.

The complexity score of this plan was lower (0.326, more complex) compared with the plan for Patient 4 (0.471, less complex), while having the same motion amplitude (15 mm). Due to the shape of the sine-6 wave, the sine-6 breathing pattern will result in more time spent superior to the home position (0 cm Sup-Inf) than inferior to the home position, possibly resulting in the delivered dose being lower than the planned dose at -1 cm. This would be attributed to the gradient effect, not the interplay effect. Again, the 4D calculation does not accurately reflect the high dose at the periphery, beyond the MIP extent. The gamma passing rate with film measurement for the Patient 5 dose reconstructions in both the 3 and 6-SPB cases was much higher (3 SPB: 94.1%, 6 SPB: 98.9%) than the treatment plan (3 SPB: 77.0%, 6 SPB: 70.8%) at 3%, 2mm gamma criteria within the MIP extent.

3.4.4. Patient 6

Profiles for Patient 6 at breathing rates of 3 and 6 SPB are shown in Figures 3.16 and 3.17, respectively. Gamma maps for Patient 6 are presented in Figures 3.18 and 3.19.

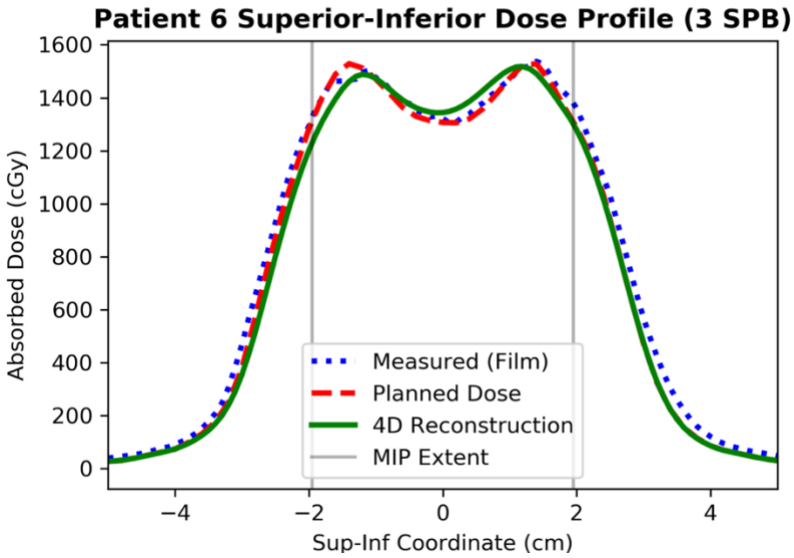

Figure 3.16. Superior-inferior dose profile for Patient 6 with breathing rate of 3 SPB.

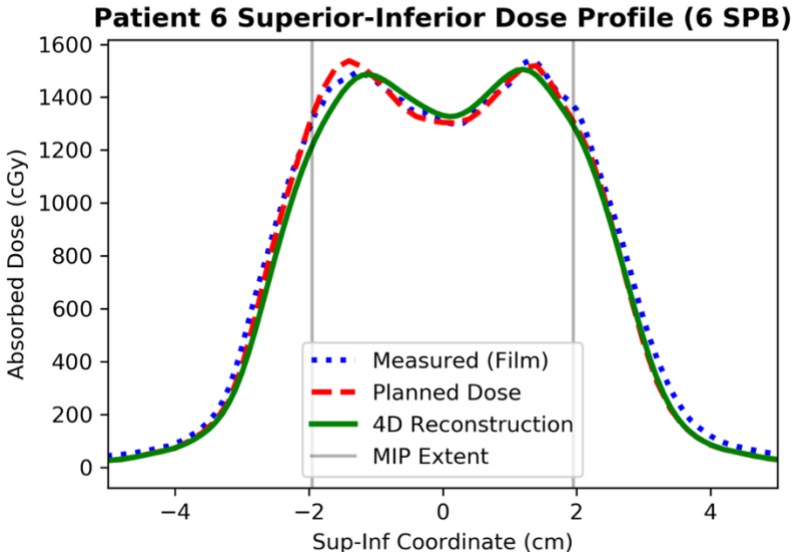

Figure 3.17. Superior-inferior dose profile for Patient 6 with breathing rate of 6 SPB.

4D reconstruction resulted in a higher dose at the center of motion than both the static planned distribution and film measurement.

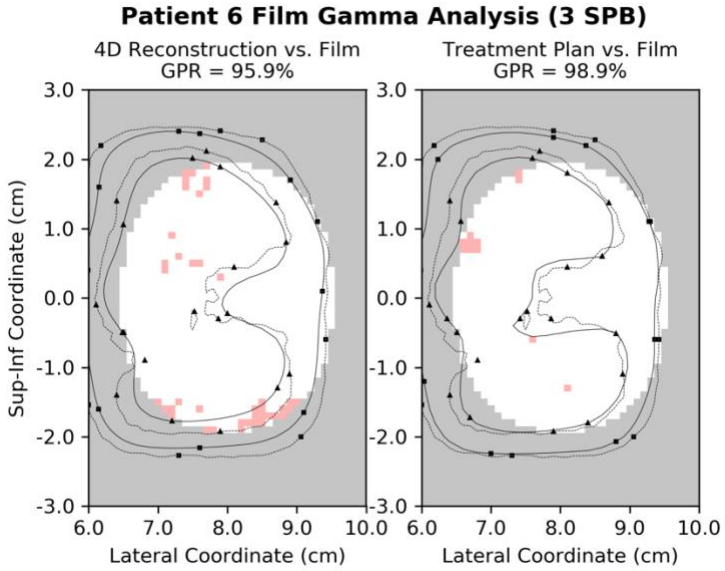

Figure 3.18. Gamma map (global 3%, 2mm) for 4D reconstruction and treatment plan vs. film measurement, within MIP extent, for Patient 6 with breathing rate 3 SPB. Color legend: Gray: Point not included in calculation; White: Passing point; Red: Failing point. Circle and square markers indicate 70% and 85% isodose contour. Dashed and solid lines indicate film and calculated dose, respectively.

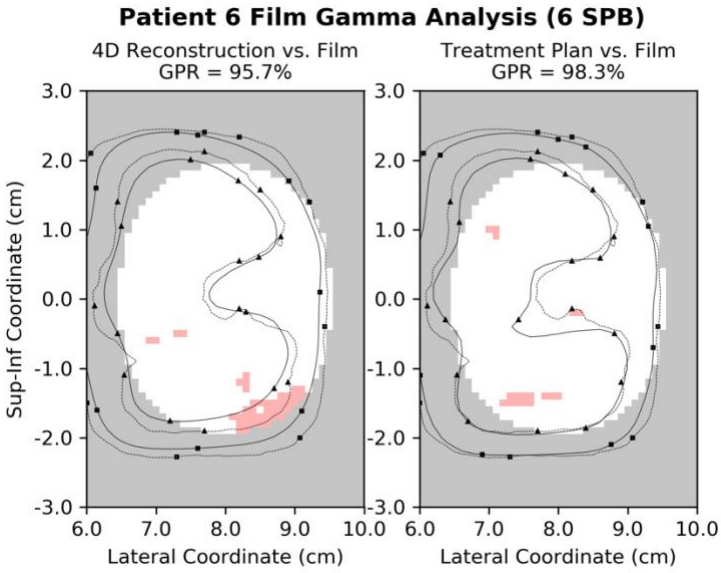

Figure 3.19. Gamma map (global 3%, 2mm) for 4D reconstruction and treatment plan vs. film measurement, within MIP extent, for Patient 6 with breathing rate 6 SPB. Color legend: Gray: Point not included in calculation; White: Passing point; Red: Failing point. Circle and square markers indicate 70% and 85% isodose contour. Dashed and solid lines indicate film and calculated dose, respectively.

The 4D reconstruction slightly underperformed when compared with film measurement than the treatment plan to the AIP image. This is quantified by a lower gamma passing rate of the 4D reconstruction with film (3 SPB: 95.9%, 6 SPB: 95.3%) within the MIP extent than the treatment plan with film (3 SPB: 98.9%, 6 SPB: 98.3%). Patient 6 was associated with 9 mm of tumor motion and a complexity score of 0.353.

3.4.5. Patient 10

Dose profiles for Patient 10 are presented in Figure 3.20 and Figure 3.21. The 4D reconstruction for Patient 10 exhibited better agreement with film measurement than the treatment plan. This plan had an MCSv of 0.250, with low tumor motion (5 mm amplitude). The 4D reconstruction of the moving target dose had a higher gamma passing rate when compared with the film measurement for both breathing rates (3 SPB: 82.0%, 6 SPB: 93.4%) than the treatment plan compared with the film measurement (3 SPB: 67.2%, 6 SPB: 67.1%).

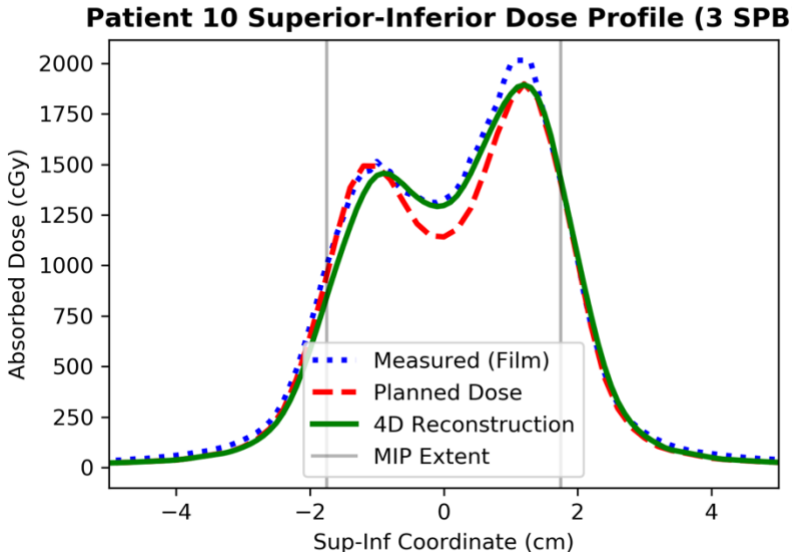

Figure 3.20. Superior-inferior dose profile for Patient 10 with breathing rate of 3 SPB.

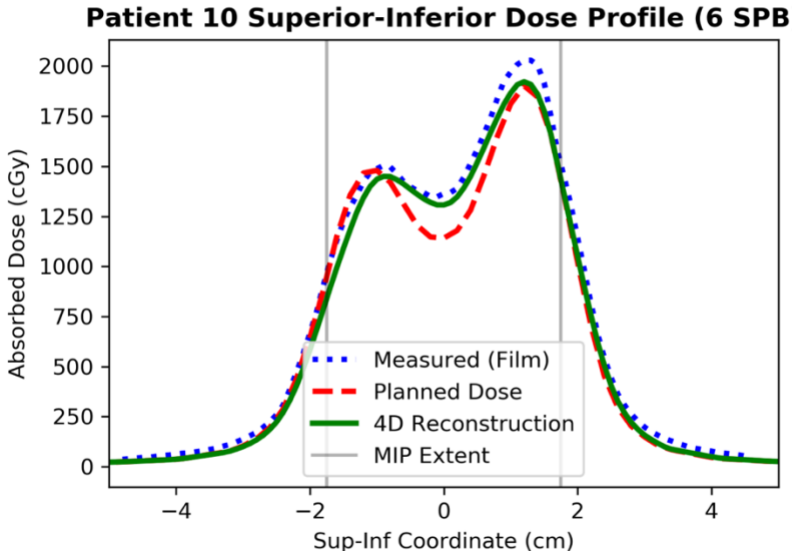

Figure 3.21. Superior-inferior dose profile for Patient 10 with breathing rate of 6 SPB.

Gamma maps for Patient 10 are presented in Figure 3.22 and Figure 3.23. Due to the low amplitude, it is unlikely that motion effects resulted in the dose deviation within the high dose region. Instead, due to the high complexity this dose error may be due to plan deliverability by the linear accelerator.

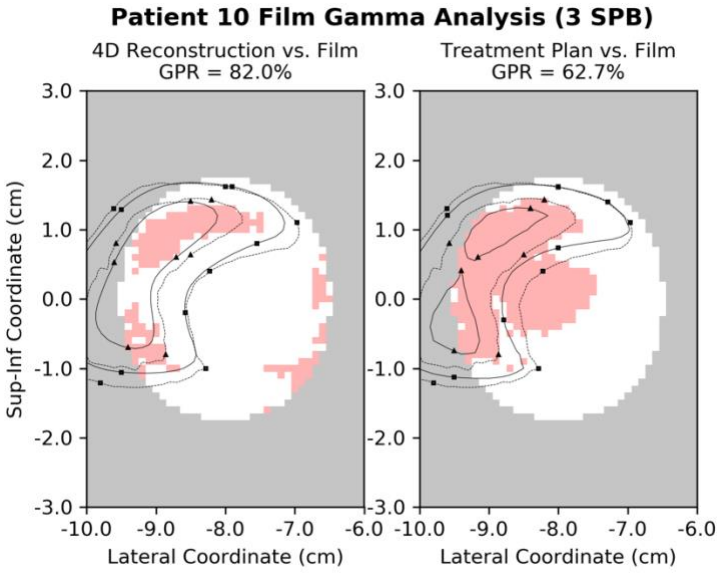

Figure 3.22. Gamma map (global 3%, 2mm) for 4D reconstruction and treatment plan vs. film measurement, within MIP extent, for Patient 10 with breathing rate 3 SPB. Color legend: Gray: Point not included in calculation; White: Passing point; Red: Failing point. Circle and square markers indicate 70% and 85% isodose contour. Dashed and solid lines indicate film and calculated dose, respectively.

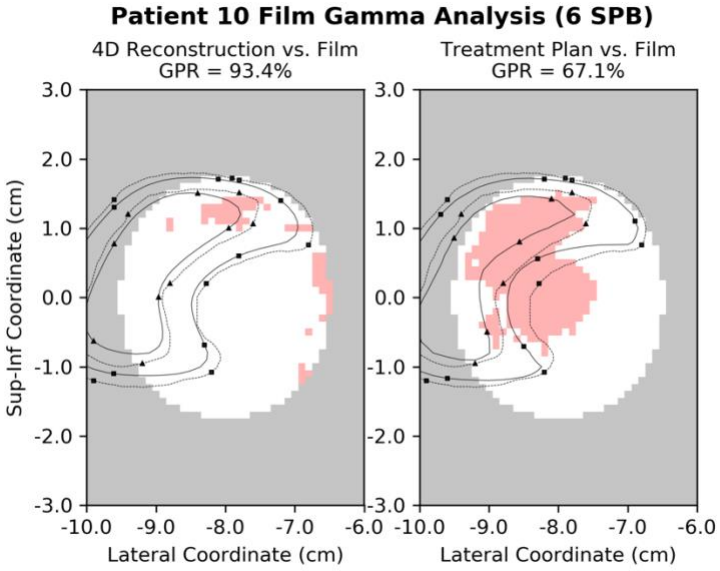

Figure 3.23. Gamma map (global 3%, 2mm) for 4D reconstruction and treatment plan vs. film measurement, within MIP extent, for Patient 10 with breathing rate 6 SPB. Color legend: Gray: Point not included in calculation; White: Passing point; Red: Failing point. Circle and square markers indicate 70% and 85% isodose contour. Dashed and solid lines indicate film and calculated dose, respectively.

3.5. Statistical Analysis of Gamma Passing Rates with Film

Gamma passing rates (GPR) were computed within the MIP extent (ITV contour) for the 4D reconstructions and treatment plans with film measurement to determine the level of agreement between each of the computed doses and the measured dose. These computations were performed for each patient at both breathing rate of 3 and 6 SPB, and with gamma criteria 3% global dose agreement and 2mm distance to agreement. Table 3.2 presents the gamma analysis results for all patients in our cohort. GPR difference was defined as the difference between the GPR of the 4D reconstruction vs. film, minus the GPR of the treatment plan vs. film in each case.

Table 3.2. Gamma passing rates (calculated vs. measured) within the MIP extent for all patient plans delivered to phantom. Bold indicates statistical significance ($p < 0.05$). GPR Difference computed as GPR(4D, Film) – GPR(Plan, Film).

Patient Number	Gamma Passing Rate within MIP 3 SPB (3%, 2mm)			Gamma Passing Rate within MIP 6 SPB (3%, 2mm)		
	4D vs Film	Plan vs Film	GPR Difference	GPR 4D vs. Film	GPR Plan vs. Film	GPR Difference
1	99.3	99.53	-0.23	98.36	97.42	0.94
2	97.88	98.21	-0.33	98.99	98.88	0.11
3	87.56	87.1	0.46	85.44	82.03	3.41
4	89.42	77.73	11.69	91.14	83.58	7.56
5	94.07	77.04	17.03	98.88	70.85	28.03
6	95.91	98.87	-2.96	95.7	98.26	-2.56
7	97.7	90.49	7.21	94.36	94.46	-0.1
8	97.44	90.79	6.65	99.8	96.11	3.69
9	97.88	97.88	0	99.66	98.21	1.45
10	81.95	62.72	19.23	93.43	67.06	26.37
11	98.26	90.58	7.68	99.28	100	-0.72
12	100	97.49	2.51	100	99.58	0.42
Mean	94.78	89.04	5.75	96.25	90.54	5.72
Median	97.57	90.69	**4.58**	98.62	96.77	**1.2**
St. Dev.	5.57	11.35	7.21	4.48	11.73	10.36

Figures 3.24 and 3.25 present plots of gamma passing rates for the 4D reconstructions and treatment plans vs. film measurement within the MIP extent for the 3 and 6 SPB breathing rates, respectively.

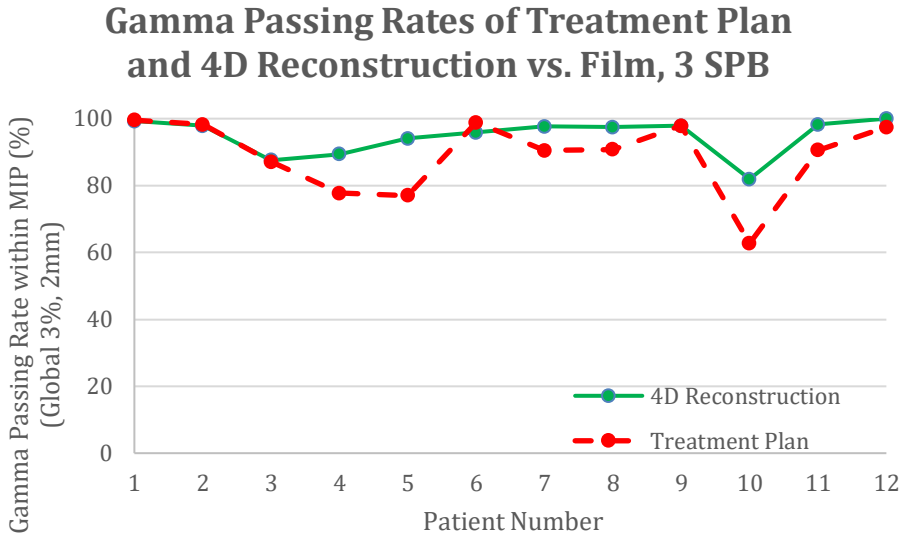

Figure 3.24. Gamma passing rates (4D reconstruction vs. film, treatment plan vs. film) within MIP extent with criteria global 3%, 2mm for all 12 patients at breathing rate of 3 SPB. Lines drawn as a visual aid.

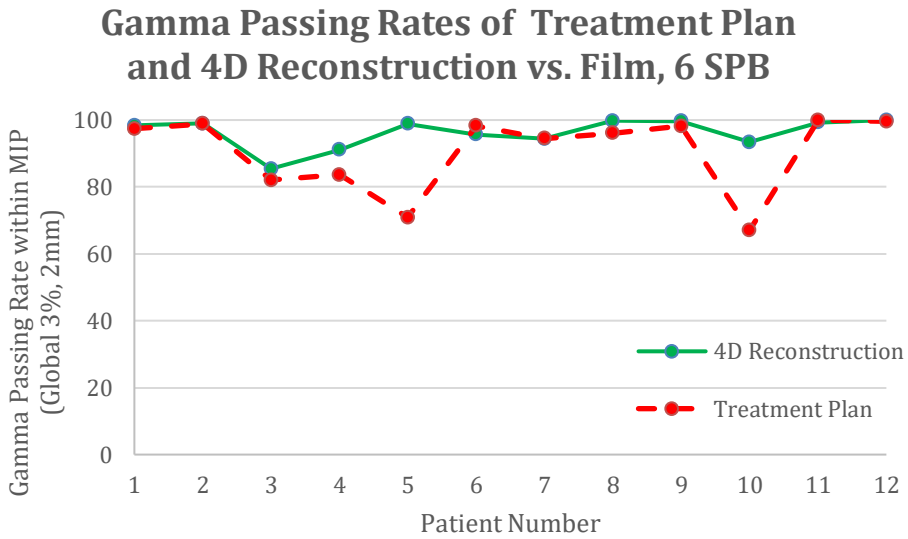

Figure 3.25. Gamma passing rates (4D reconstruction vs. film, treatment plan vs. film) within MIP extent with criteria global 3%, 2mm for all 12 patients at breathing rate of 3 SPB. Lines drawn as a visual aid.

A positive GPR difference value indicates that the 4D reconstruction outperformed the treatment plan in comparison with the film measurement. The mean gamma passing rates within the MIP for the 3 SPB breathing rate were found to be 94.8% $\pm$ 5.5% for the 4D accumulation vs. film and 89.0% $\pm$ 7.2% for the treatment plans vs. film. Median GPR values for the 3 SPB breathing rate were respectively 97.6% and 90.7%. The median GPR differences across all patients were +4.58% for the 3 SPB measurements and +1.2% for the 6 SPB measurements. Both median GPR differences were found to be statistically significant (p = 0.013 and p=0.017, respectively), according to a Wilcoxon signed-rank test of the data. A box plot presenting the aggregate GPR differences for both breathing rates across all patients is shown in Figure 3.26.

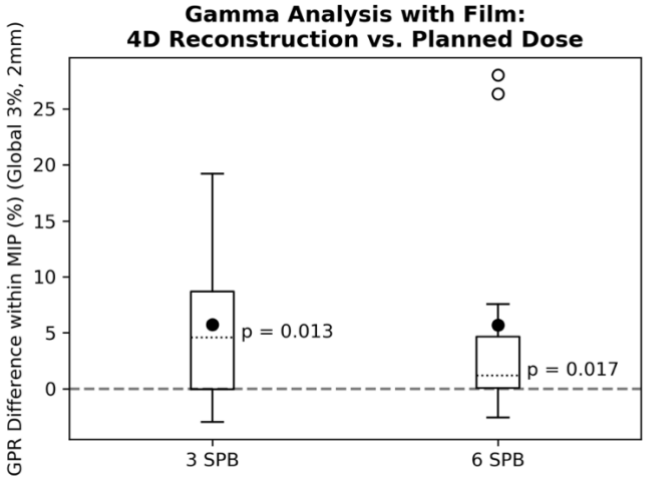

Figure 3.26. Gamma passing rate difference for breathing rates of 3 and 6 SPB for all patient plans delivered to phantom. Positive difference value indicates 4D dose reconstruction resulted in a higher GPR with film measurement than the treatment plan copied to the phantom. Values of statistical significance displayed as p-values for the median. P-values computed using Wilcoxon signed-rank test. Mean GPR difference displayed as filled circles.

Chapter 4. Discussion and Conclusions

4.1. Summary of Findings

In this work, we developed and tested a procedure for utilizing Elekta machine log files to retrospectively calculate the dose to the moving target during lung SBRT. To accomplish this, we used a programmable respiratory phantom as a surrogate for a lung cancer patient undergoing lung SBRT. The programmable respiratory phantom allowed us to place radiochromic film at the treatment isocenter and measure dose to a target moving in the superior-inferior direction. We reconstructed moving target dose for 12 clinical SBRT plans at 2 breathing rates (a clinically realistic 3 SPB and longer 6 SPB) and compared our reconstructed doses to the measured film doses. In addition, we compared the reconstructed doses to their corresponding static plans using gamma analysis. All reconstructed (4D) planar dose distributions had a gamma passing rate above 94% when compared with the corresponding static plans, using the AAPM TG 218 recommended criteria for IMRT patient-specific quality assurance (3%, 2mm, and 10% threshold) (Miften, et al. 2018).

Further gamma analysis using a more restrictive threshold (50%) allowed us to pinpoint cases in which motion resulted in dose deviations from the static plan within the high dose region. These cases were further considered by comparison with film. Profile comparison and gamma analysis of the treatment plans and 4D reconstructed doses with film measurement indicated that for 3 of the 4 studied cases with notable discrepancy, the film measurement more closely agreed with the 4D reconstruction than the static plan (Patients 4, 5, and 10).

We found that when considering the 4D dose reconstructions for all of the patients, the gamma passing between the 4D dose reconstruction and the film measurement was significantly higher according to the Wilcoxon signed-rank test (3 SPB, $p=0.013$; 6 SPB, $p=0.017$) for both

breathing rates within the tumor motion extent (within the MIP ITV contour) than the gamma passing rate between the treatment plan to static geometry and the film. This holds true to our expectations, and further verifies the 4D dose reconstruction method utilizing 4D-CT imaging.

To our knowledge, this is the first film-based end-to-end verification of log file-based dose reconstruction to moving targets during lung SBRT using 4D-CT imaging. Previously, Zou et al. simulated motion effects on dose using a similar 4D-CT based methodology (Zou, et al. 2014). However, in their study, motion was simulated in the treatment planning system and was not delivered to phantom or measured using film. In a study similar to this study, Poulsen, et al. performed an end-to-end verification of their isocenter shift method in which intrafraction respiratory motion was combined with the machine log data and log file control points were assigned an isocenter position based on the respiratory trace position at corresponding time points (Poulsen, et al. 2012). The incorporation of 4D-CT imaging into the determination of moving-target dose provides a first-order approximation of the deformation of the anatomy of the patient at each breathing phase during treatment. Hence, the dose to moving normal tissues may also be accounted for, as well as the effect of tumor deformation during respiration. Both of these benefits assume that the time-dependent patient internal anatomy during 4D-CT remains consistent during their course of treatment.

4.2. Limitations of this Work

In our study, lung SBRT plans were delivered to a programmable respiratory phantom, which allowed us to test our dose reconstruction under controlled respiratory motion which was identical during 4D-CT imaging and beam delivery. Exact reproducibility of the breathing pattern from 4D-CT to treatment is unrealistic to a clinical scenario with a real patient given the variability in patient breathing cycles over time (Mageras, et al. 2004) (Keall, et al. 2006) (Sonke, et al. 2008).

In addition, the phantom remained static on the treatment couch during beam delivery, which is again unrealistic to actual patient treatment conditions (i.e, small movements of the patient during treatment) and represents an ideal situation. Both of these inconsistencies between delivering beams to a phantom and to a real patient will cause deviation of the 4D reconstruction from the actual delivered dose.

In lieu of generating plans made specifically for the phantom geometry, real patient plans were copied onto the phantom. Due to the geometrical differences between the real patients and the phantom, the computed dose to the phantom may have contained dose heterogeneities and falloff within the region of tumor motion not found within the real patient plans. Thus, plans copied to the phantom may have been more susceptible to tumor motion than the original plans to the patients. However, the treatment plans copied to the phantom still provided a valid baseline upon which to compare the 4D dose reconstructions because the geometrical setup of both dose computations (planned and reconstructed) remained consistent.

Next, we saw a breakdown of the 4D dose reconstruction outside of the MIP extent; the region outside of the MIP extent is still within the PTV due to the setup margin, and these results suggest that 4D dose reconstruction may yield incorrect dose to the peripheral portion of the PTV. However, intensity-based DIR has been previously shown to have decreased performance in low-contrast regions (Zhong, et al. 2012). Thus, the breakdown of the 4D dose reconstruction outside of the MIP extent may have been associated with the homogeneity of the phantom and lack of spatial information surrounding the tumor. It has been shown that, for similar DIR performance in phantom images to a real patient images, the phantom should have similar density heterogeneity to the patient (Kirby, et al. 2013). This suggests that the 4D reconstruction will perform better

outside the MIP extent in real patient cases than it does in the case of the Quasar phantom, since patient images provide increased tissue heterogeneity in the region surrounding the tumor.

4.3. Future Work

The Quasar phantom has several cylindrical insert types, including an insert that has been drilled for an ion chamber. Therefore, ion chamber measurements may be used to further validate the 4D dose reconstruction method and provide normalization for subsequent film measurements (i.e., correct for daily machine output variance, which was not accounted for in this study). The 4D dose reconstruction procedure is time and labor intensive (approximately 2 hours per reconstruction) and the isocenter shift method is much faster (during the isocenter shift method, beams are only computed on one image (Poulsen, et al. 2012); in a 4D dose reconstruction, beams are computed on all 4D-CT images). Thus, the clinical utility of performing a full 4D dose reconstruction using 4D-CT should be understood. The dose reconstruction quality difference between the two methods could be assessed using a deformable respiratory phantom, as this would better represent the internal deformation of patient anatomy.

Later work should consider the variability of internal patient anatomy caused by respiration during treatment delivery and incorporate this information into the 4D dose reconstruction. To accommodate this, on-board imaging with cone-beam CT (CBCT) during beam delivery may allow mapping between the patient anatomy during the treatment and during the 4D-CT images taken at the start of their treatment cycle. On-board imaging during beam delivery has been studied for the purpose of determining intra-fraction tumor motion; these methods include both partial-arc CBCT reconstruction and fluoroscopy using the on-board CBCT imager (Haytmyradov, et al. 2019,Shieh, et al. 2015). By finding the deformation mapping between the intra-fraction on-board imaging and the corresponding 4D-CT images taken during the planning phase, intra-fraction

anatomical variation could be incorporated into the 4D-CT based dose reconstruction presented in this work. However, the addition of on-board imaging during treatment would increase the radiation dose to the patient, and the trade-off between increased dose reconstruction accuracy and increased patient dose must be considered.

Appendix A. Superior-Inferior Dose Profiles

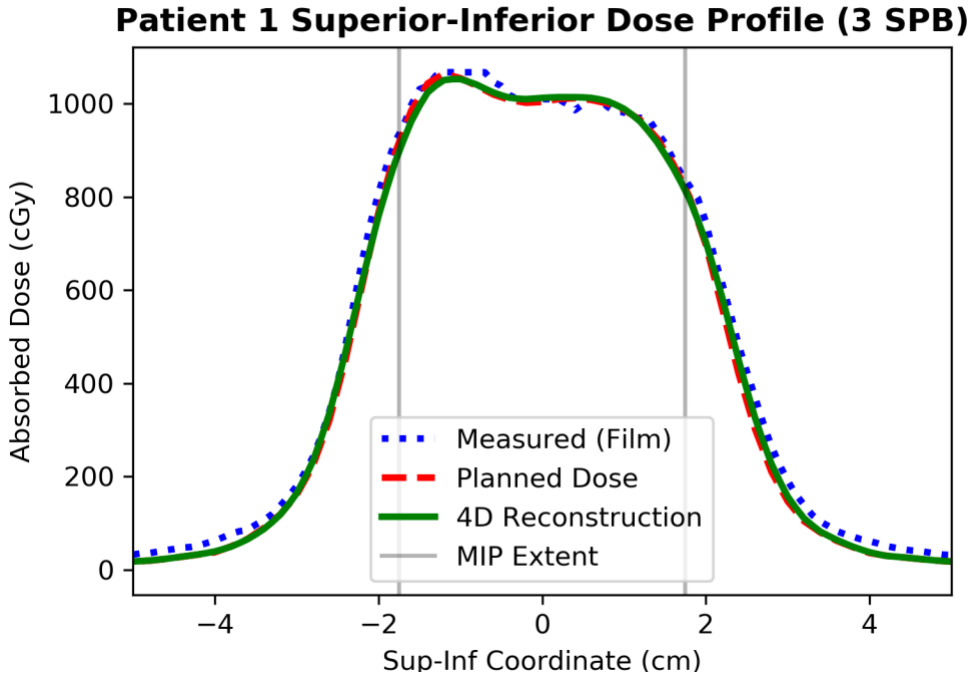

Figure A.1. Superior-inferior dose profiles showing film measurement, treatment plan, and 4D reconstructed dose, for Patient 1 at a breathing rate of 3 SPB.

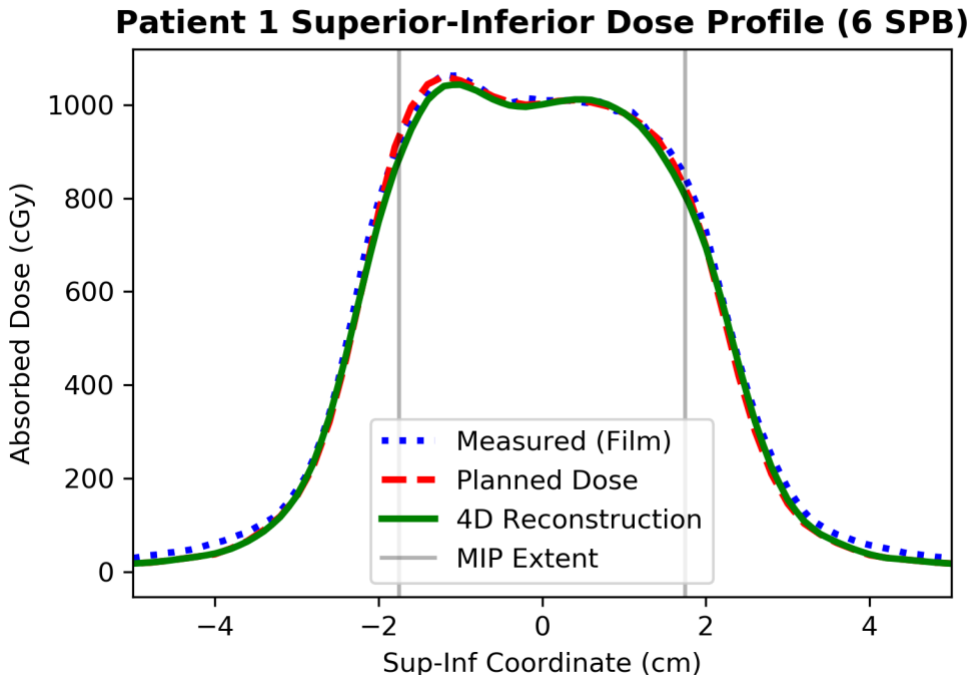

Figure A.2. Superior-inferior dose profiles showing film measurement, treatment plan, and 4D reconstructed dose, for Patient 1 at a breathing rate of 6 SPB.

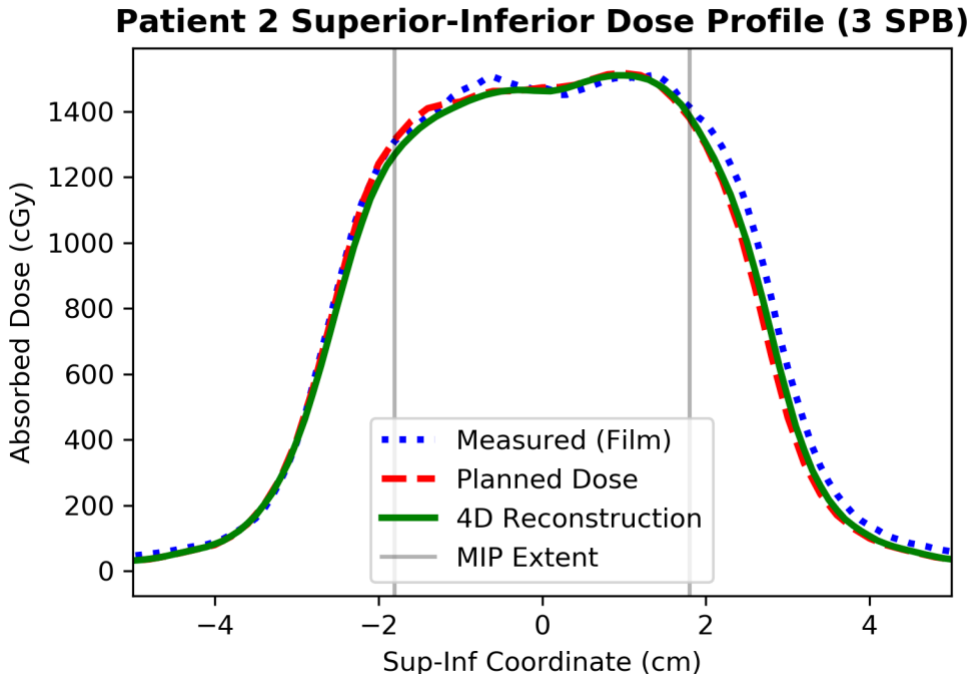

Figure A.3. Superior-inferior dose profiles showing film measurement, treatment plan, and 4D reconstructed dose, for Patient 2 at a breathing rate of 3 SPB.

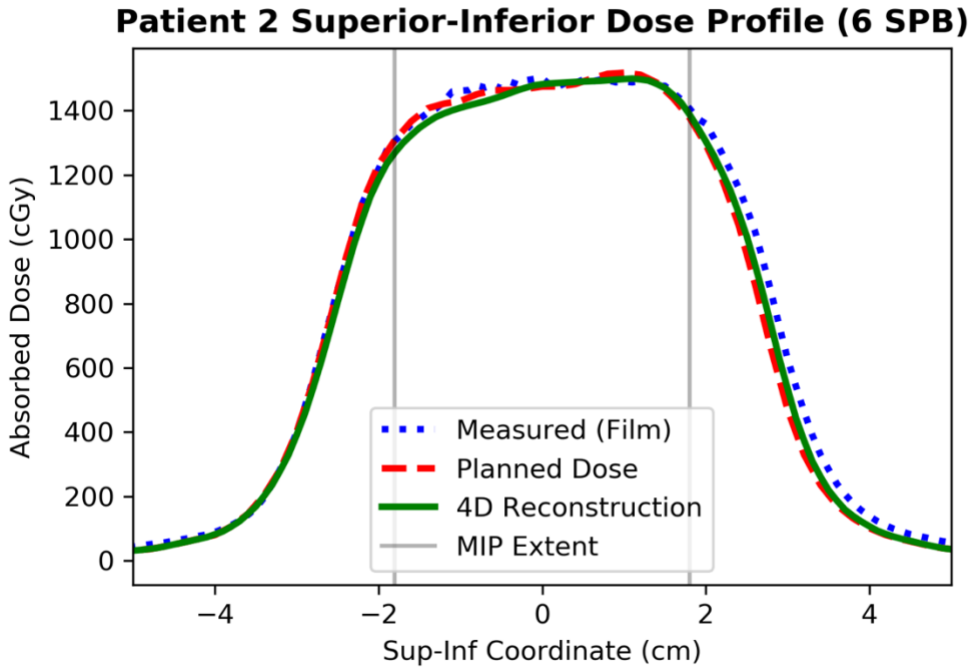

Figure A.4. Superior-inferior dose profiles showing film measurement, treatment plan, and 4D reconstructed dose, for Patient 2 at a breathing rate of 6 SPB.

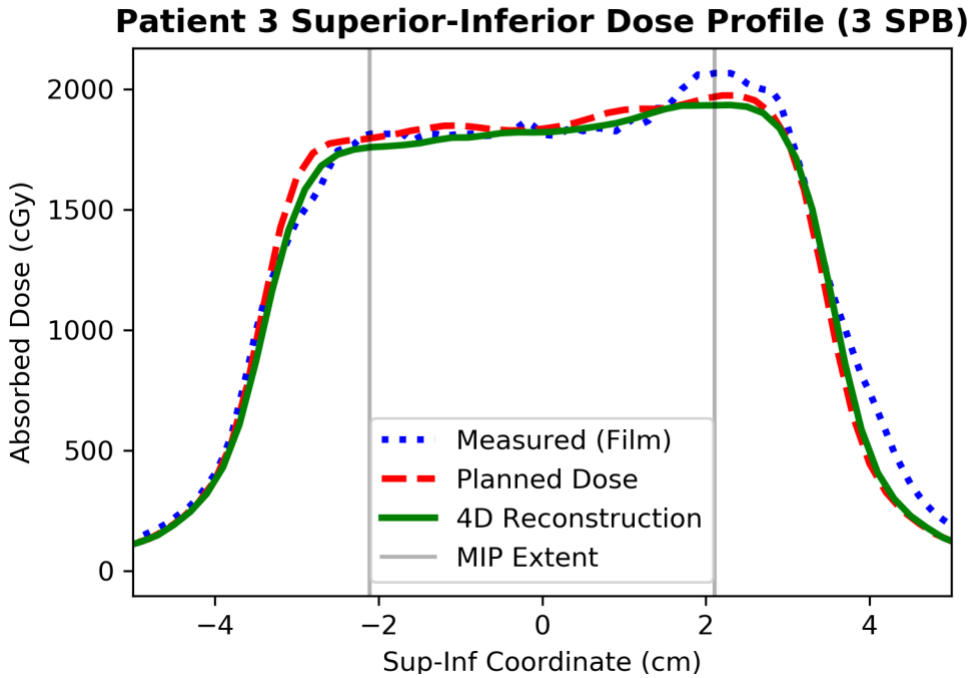

Figure A.5. Superior-inferior dose profiles showing film measurement, treatment plan, and 4D reconstructed dose, for Patient 3 at a breathing rate of 3 SPB.

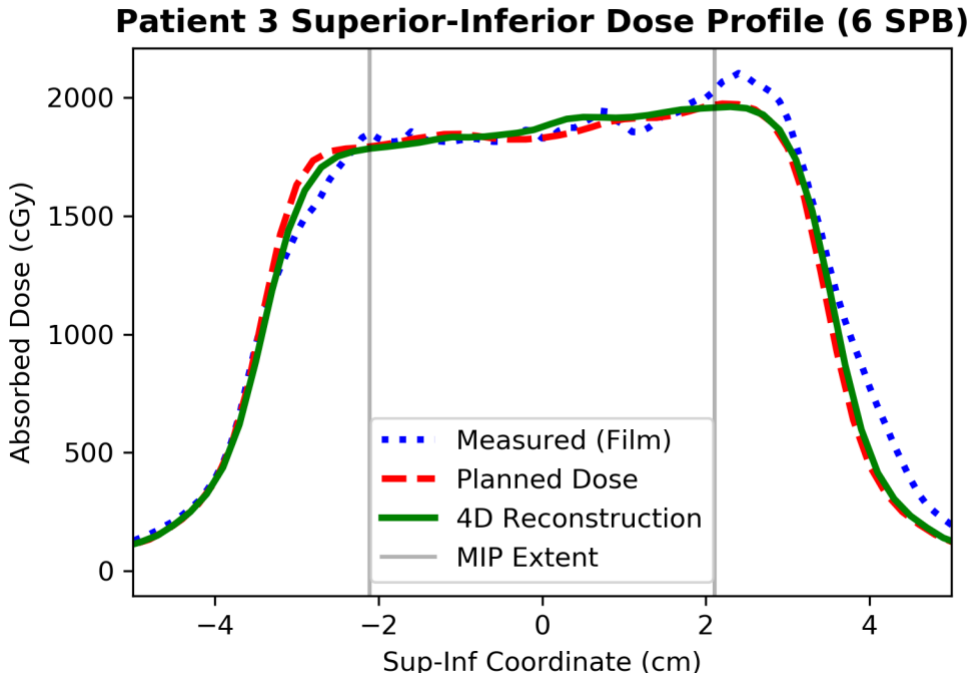

Figure A.6. Superior-inferior dose profiles showing film measurement, treatment plan, and 4D reconstructed dose, for Patient 3 at a breathing rate of 6 SPB.

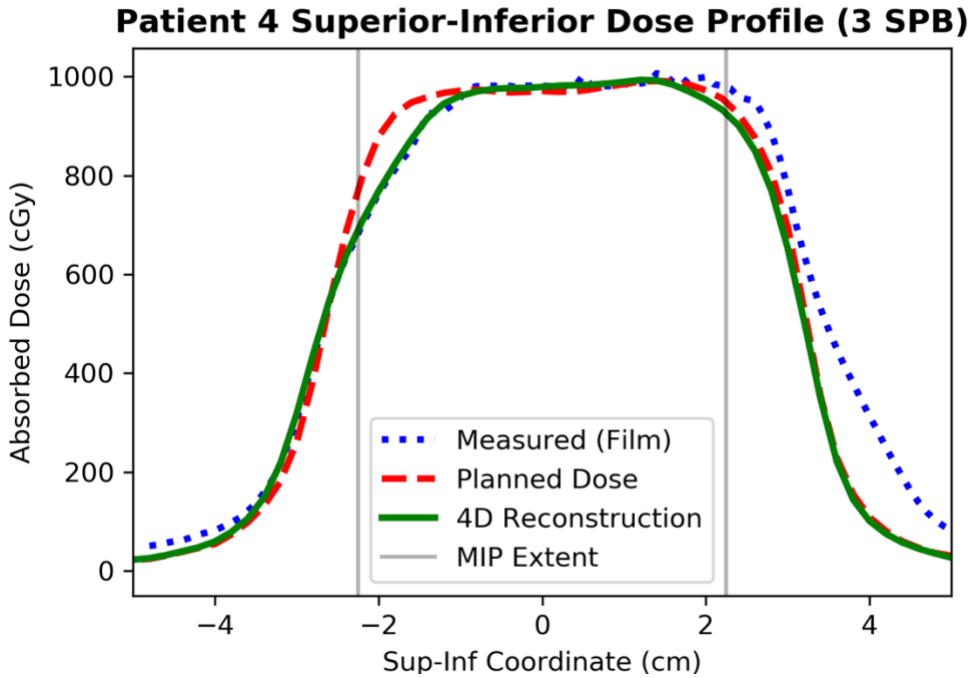

Figure A.7. Superior-inferior dose profiles showing film measurement, treatment plan, and 4D reconstructed dose, for Patient 4 at a breathing rate of 3 SPB.

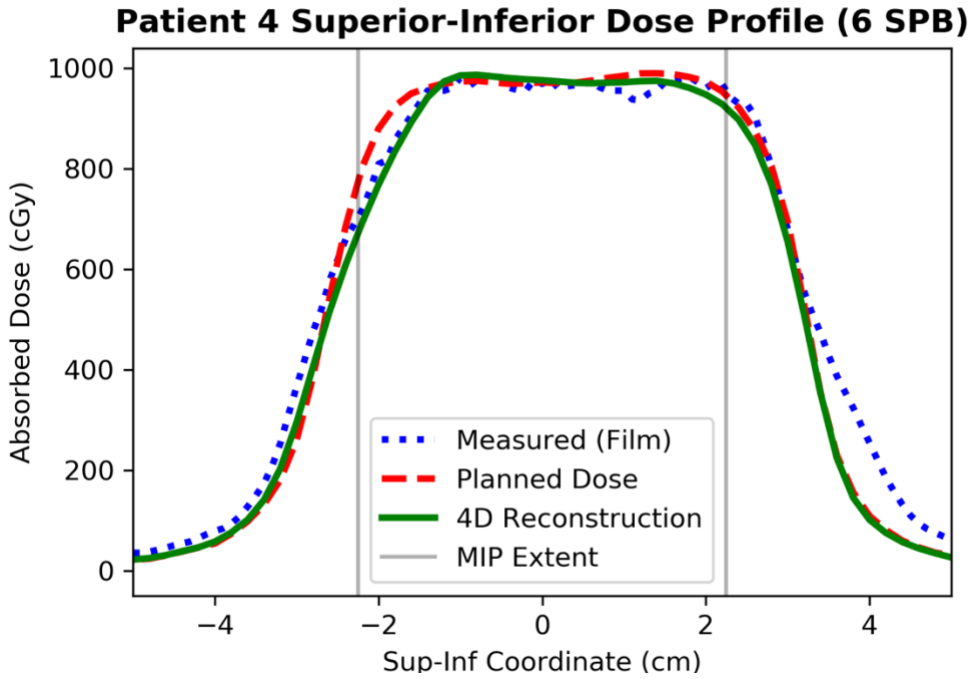

Figure A.8. Superior-inferior dose profiles showing film measurement, treatment plan, and 4D reconstructed dose, for Patient 4 at a breathing rate of 6 SPB.

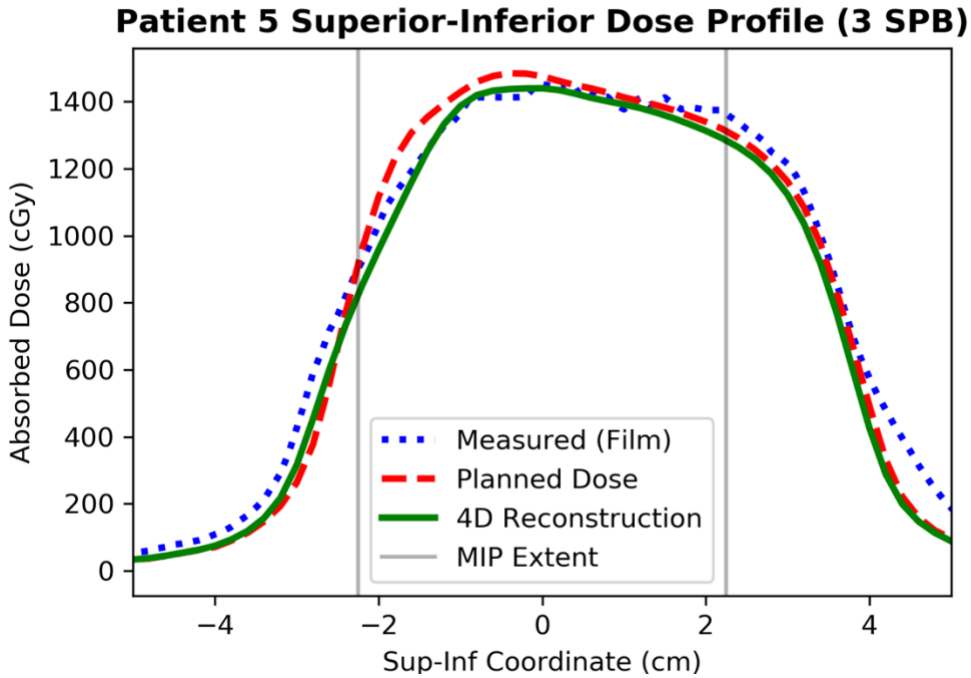

Figure A.9. Superior-inferior dose profiles showing film measurement, treatment plan, and 4D reconstructed dose, for Patient 5 at a breathing rate of 3 SPB.

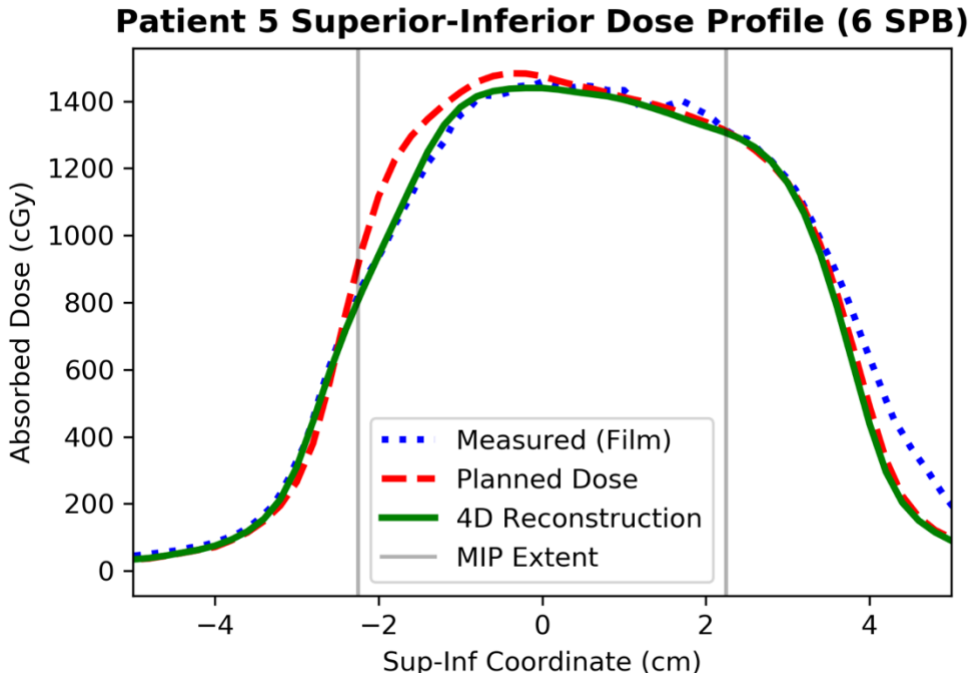

Figure A.10. Superior-inferior dose profiles showing film measurement, treatment plan, and 4D reconstructed dose, for Patient 5 at a breathing rate of 6 SPB.

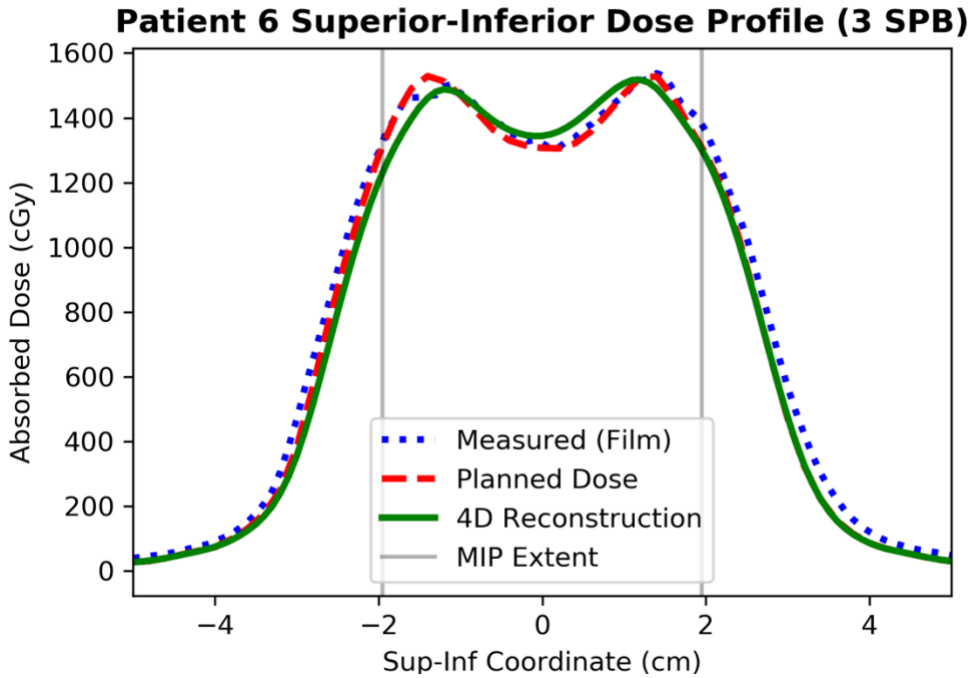

Figure A.11. Superior-inferior dose profiles showing film measurement, treatment plan, and 4D reconstructed dose, for Patient 6 at a breathing rate of 3 SPB.

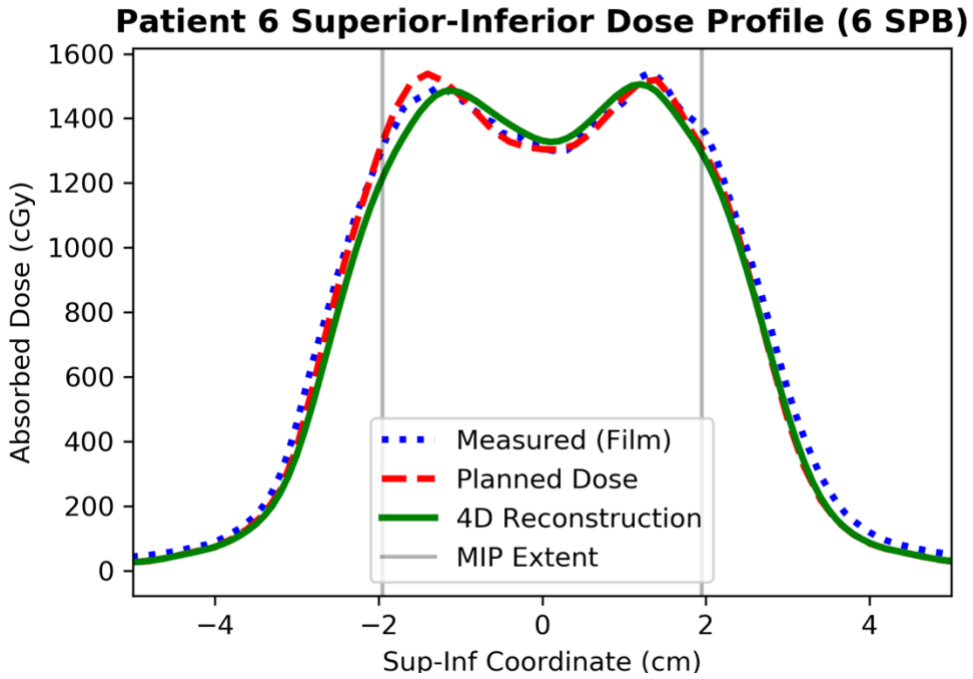

Figure A.12. Superior-inferior dose profiles showing film measurement, treatment plan, and 4D reconstructed dose, for Patient 6 at a breathing rate of 6 SPB.

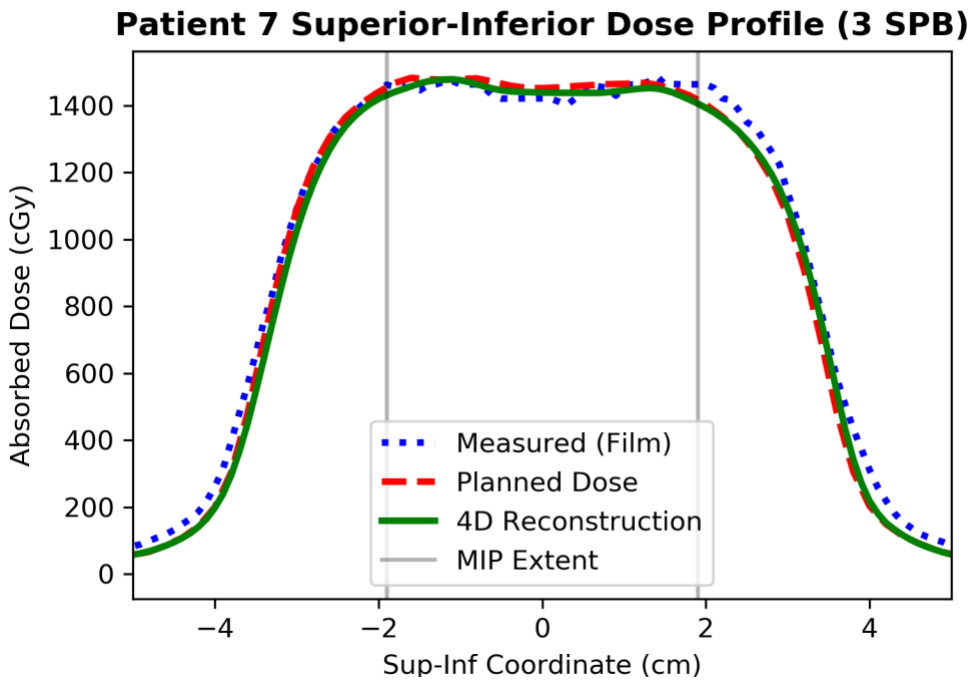

Figure A.13. Superior-inferior dose profiles showing film measurement, treatment plan, and 4D reconstructed dose, for Patient 7 at a breathing rate of 3 SPB.

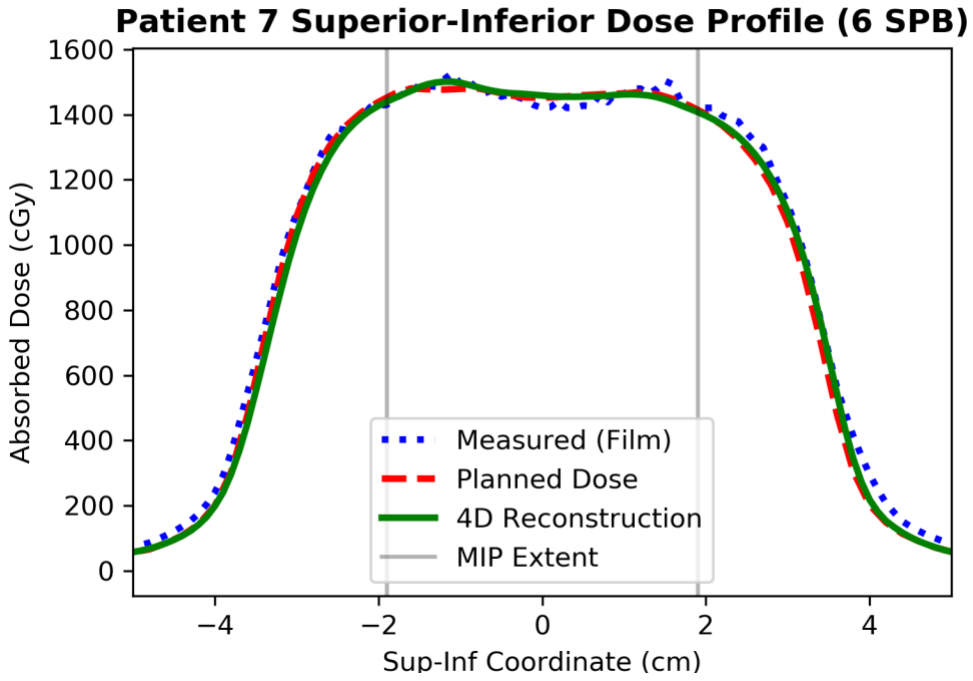

Figure A.14. Superior-inferior dose profiles showing film measurement, treatment plan, and 4D reconstructed dose, for Patient 7 at a breathing rate of 6 SPB.

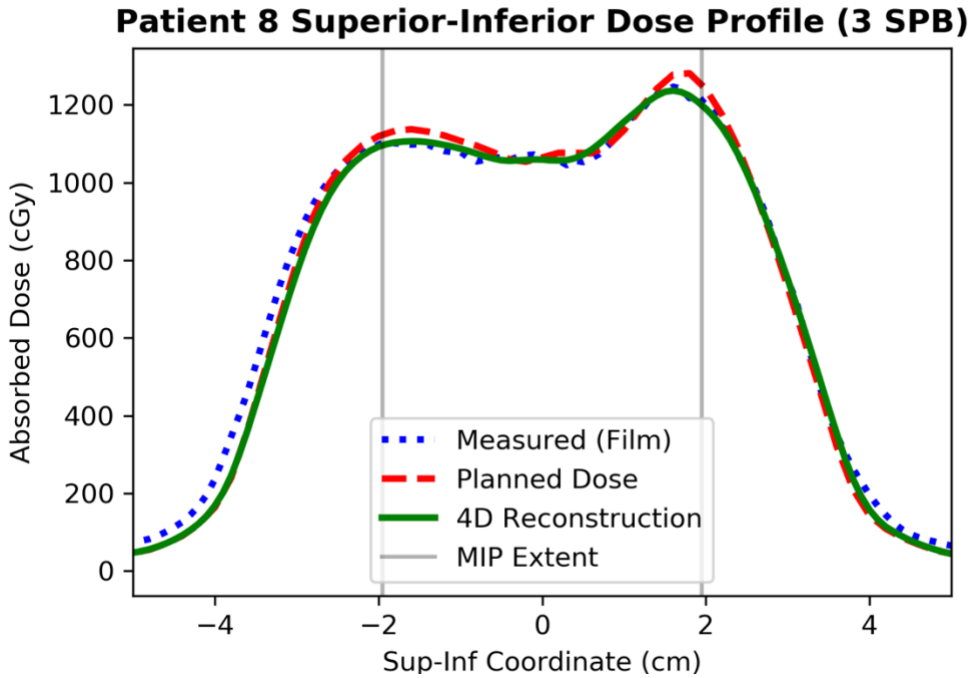

Figure A.15. Superior-inferior dose profiles showing film measurement, treatment plan, and 4D reconstructed dose, for Patient 8 at a breathing rate of 3 SPB.

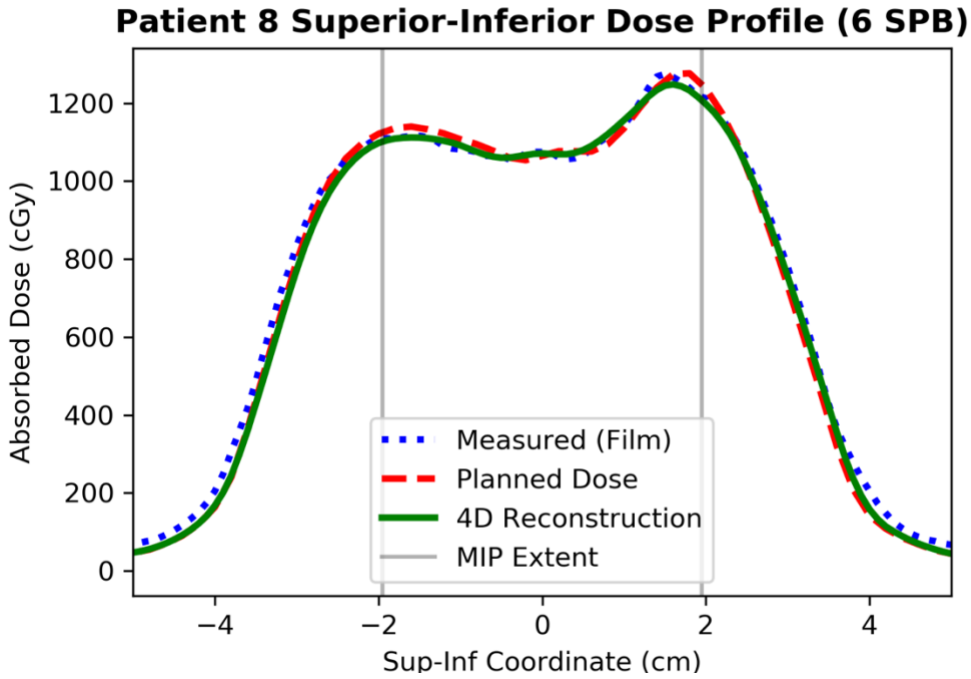

Figure A.16. Superior-inferior dose profiles showing film measurement, treatment plan, and 4D reconstructed dose, for Patient 8 at a breathing rate of 6 SPB.

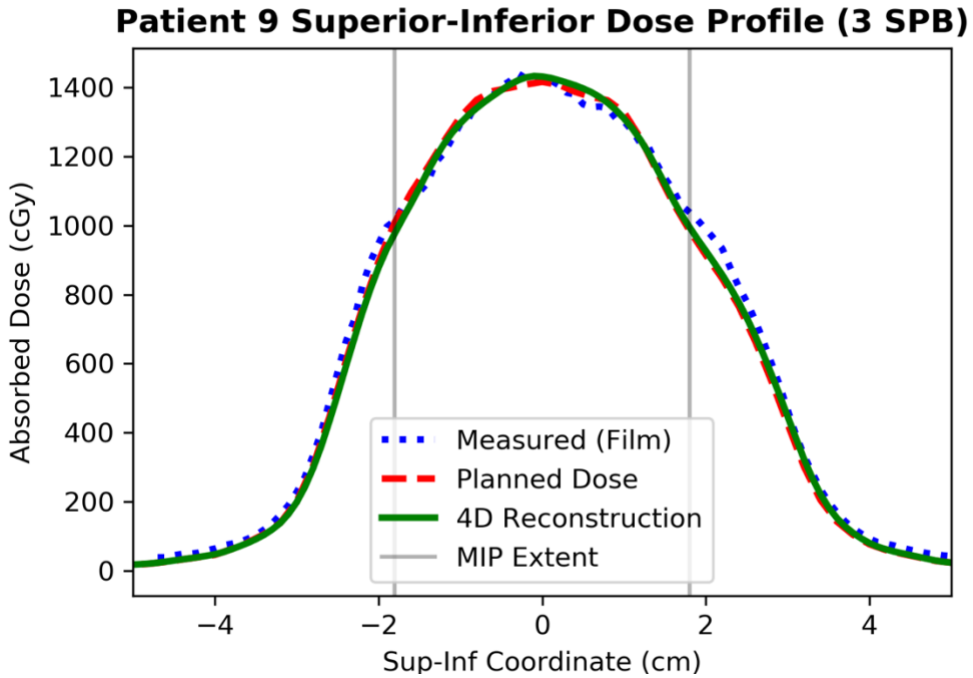

Figure A.17. Superior-inferior dose profiles showing film measurement, treatment plan, and 4D reconstructed dose, for Patient 9 at a breathing rate of 3 SPB.

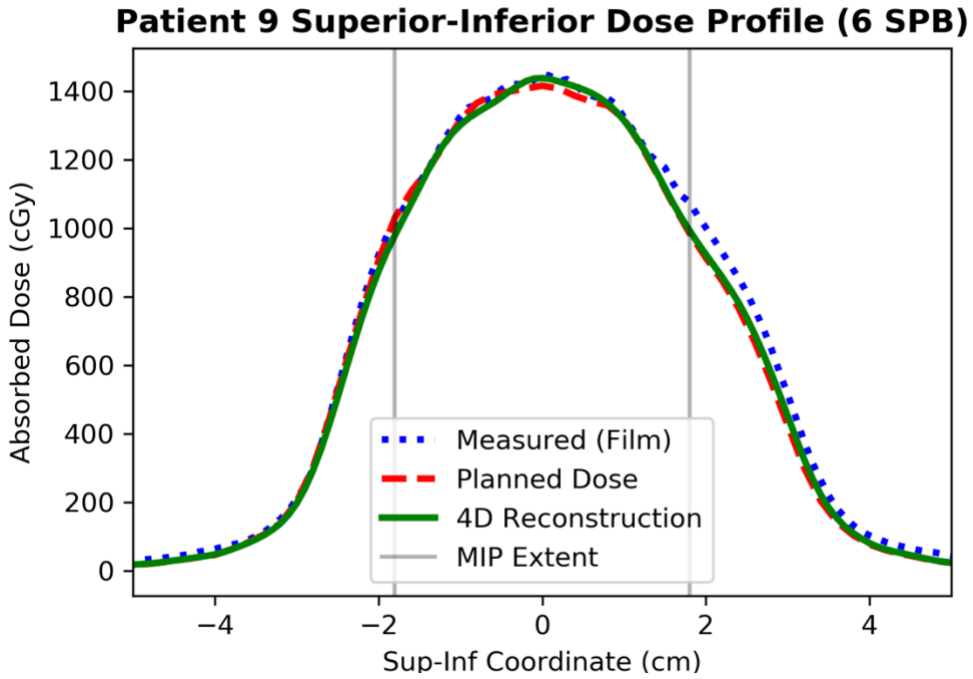

Figure A.18. Superior-inferior dose profiles showing film measurement, treatment plan, and 4D reconstructed dose, for Patient 9 at a breathing rate of 6 SPB.

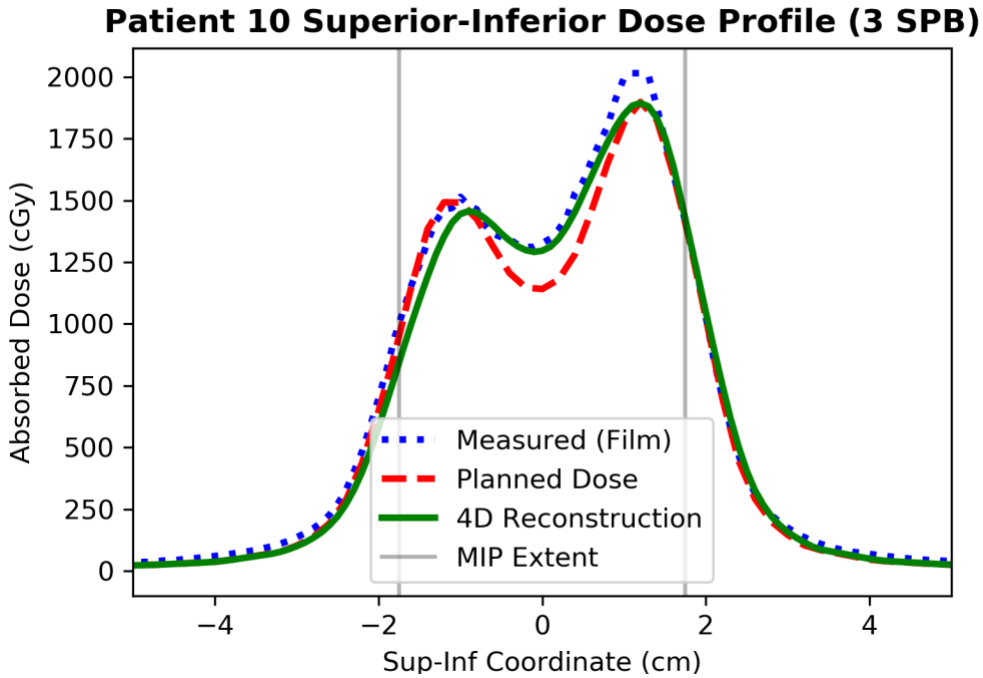

Figure A.19. Superior-inferior dose profiles showing film measurement, treatment plan, and 4D reconstructed dose, for Patient 10 at a breathing rate of 3 SPB.

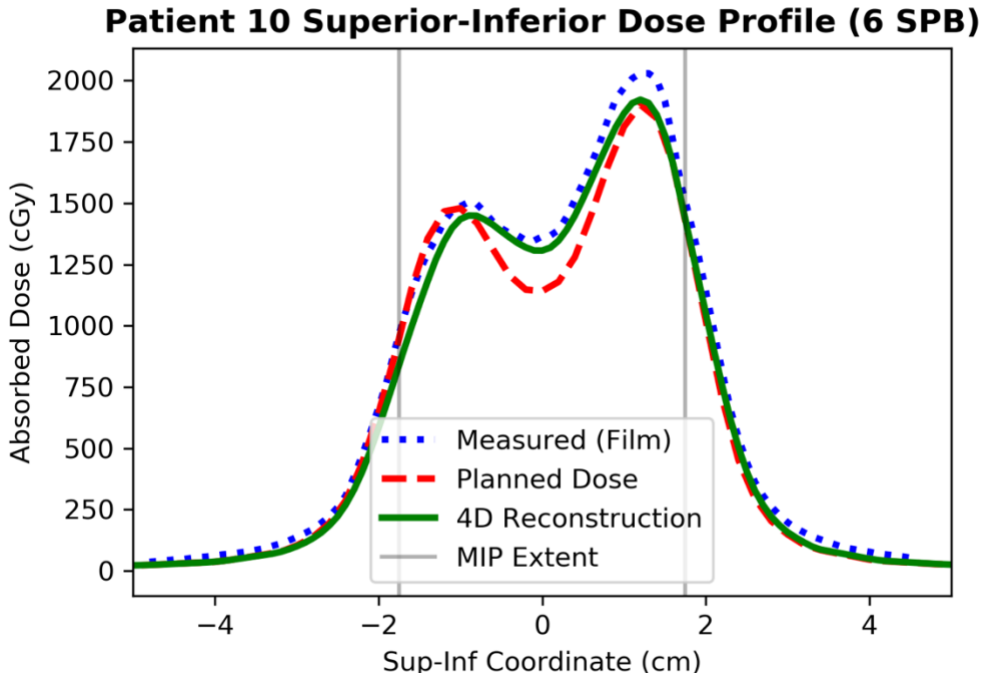

Figure A.20. Superior-inferior dose profiles showing film measurement, treatment plan, and 4D reconstructed dose, for Patient 10 at a breathing rate of 6 SPB.

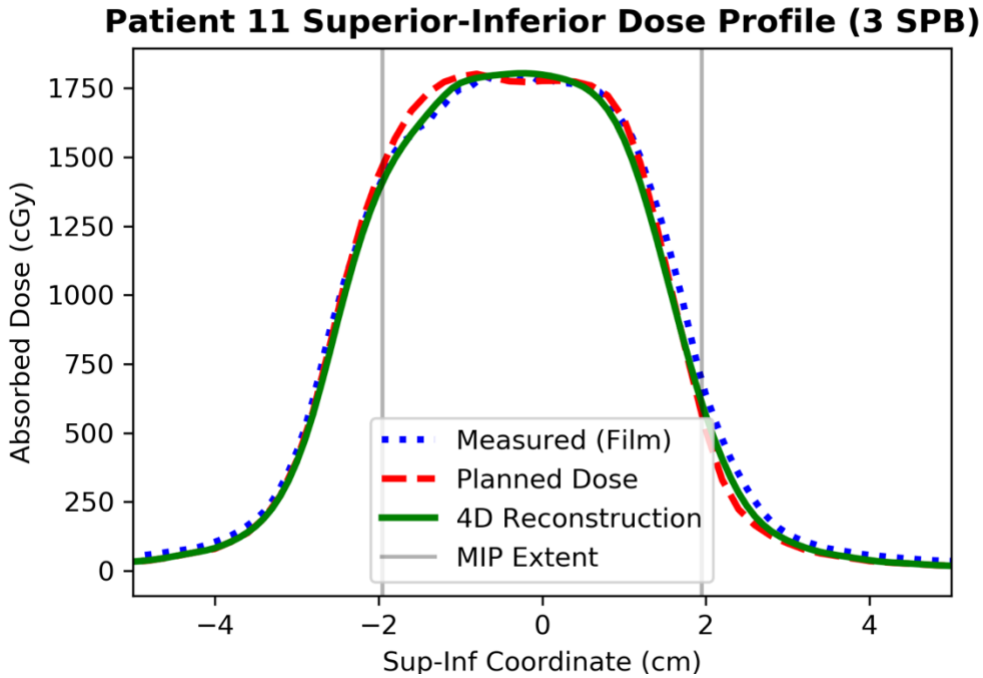

Figure A.21. Superior-inferior dose profiles showing film measurement, treatment plan, and 4D reconstructed dose, for Patient 11 at a breathing rate of 3 SPB.

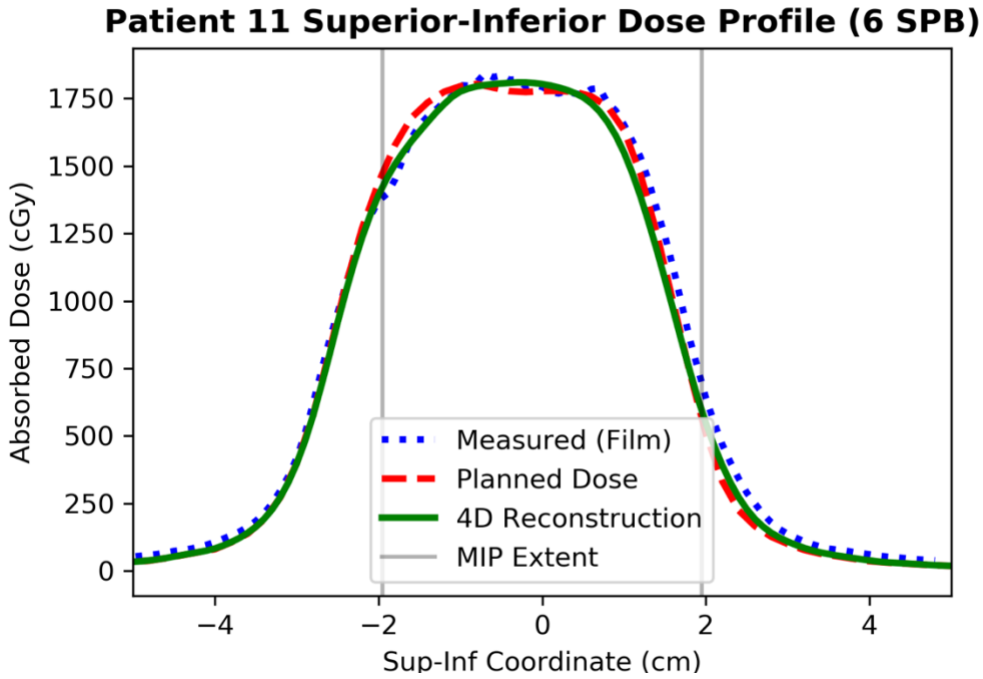

Figure A.22. Superior-inferior dose profiles showing film measurement, treatment plan, and 4D reconstructed dose, for Patient 11 at a breathing rate of 6 SPB.

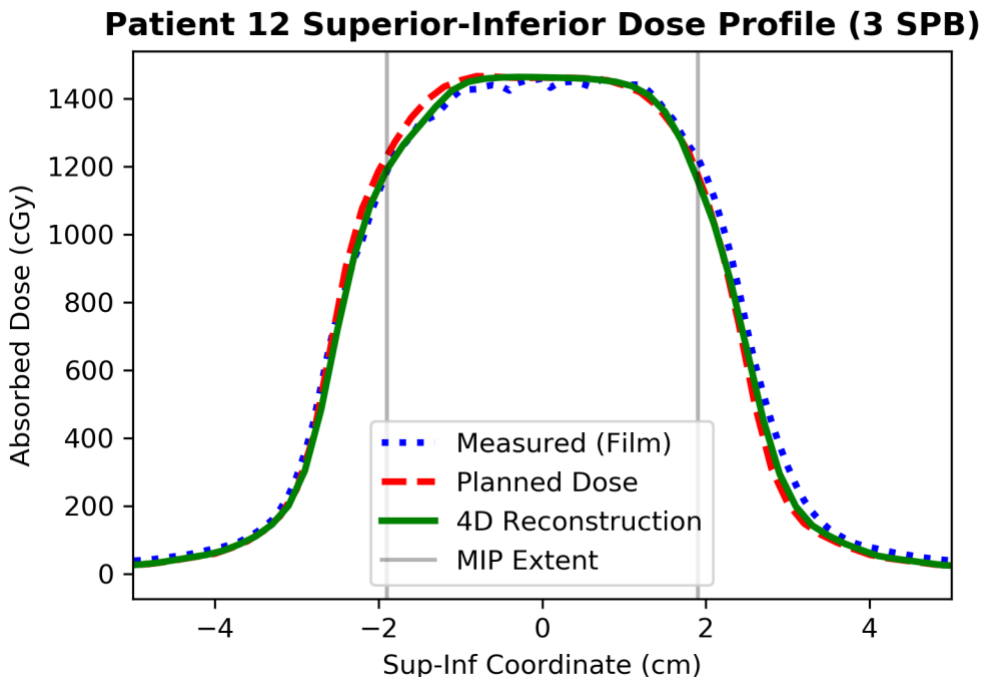

Figure A.23. Superior-inferior dose profiles showing film measurement, treatment plan, and 4D reconstructed dose, for Patient 12 at a breathing rate of 3 SPB.

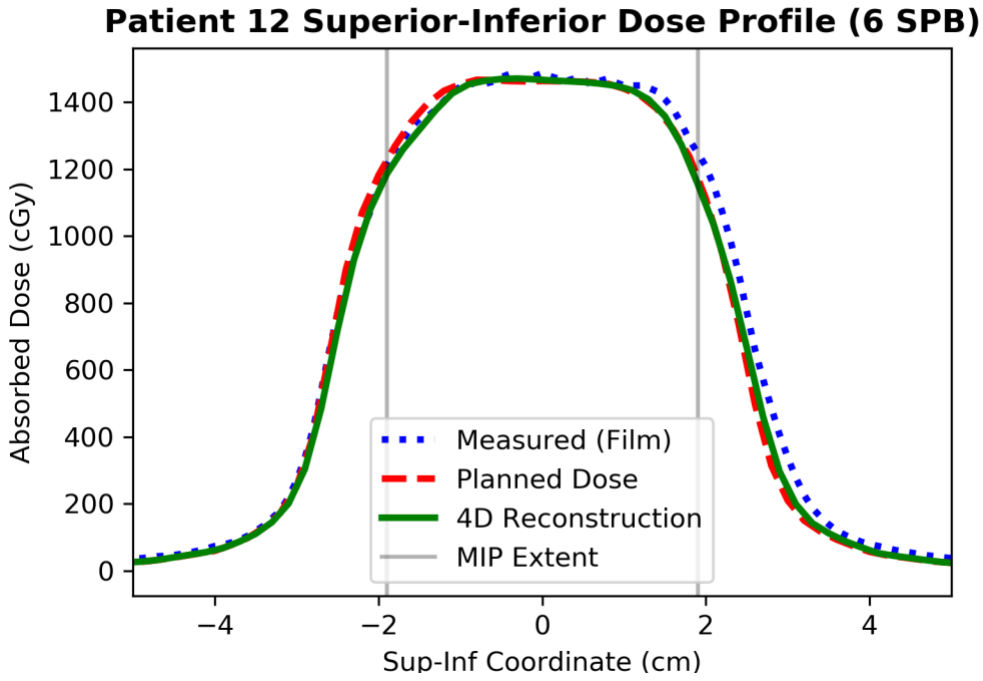

Figure A.24. Superior-inferior dose profiles showing film measurement, treatment plan, and 4D reconstructed dose, for Patient 12 at a breathing rate of 6 SPB.

Appendix B. Lateral Dose Profiles

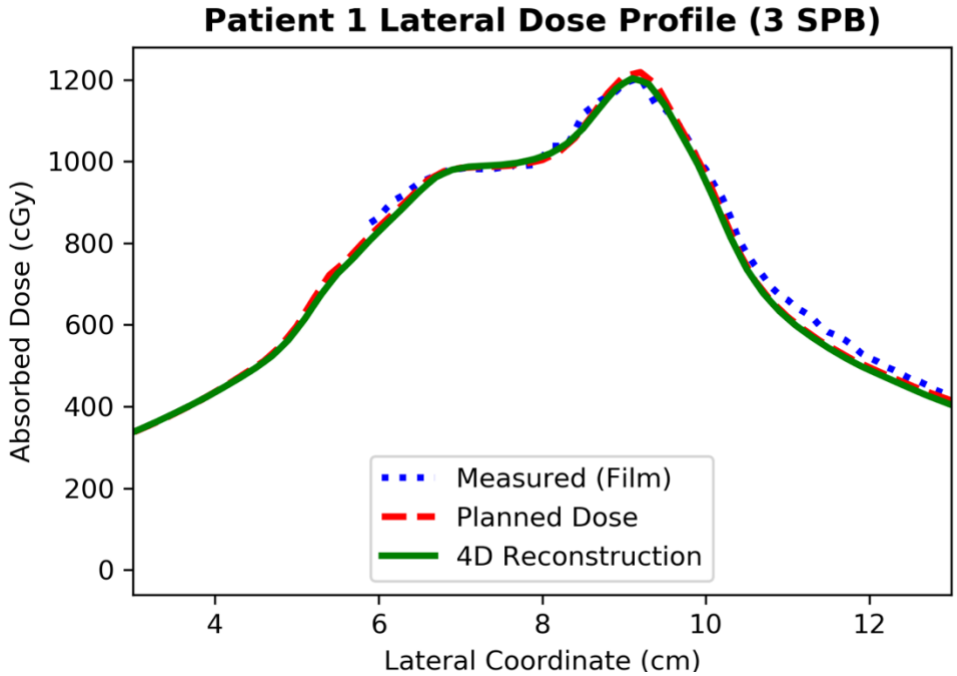

Figure B.1. Lateral dose profiles showing film measurement, treatment plan, and 4D reconstructed dose, for Patient 1 at a breathing rate of 3 SPB.

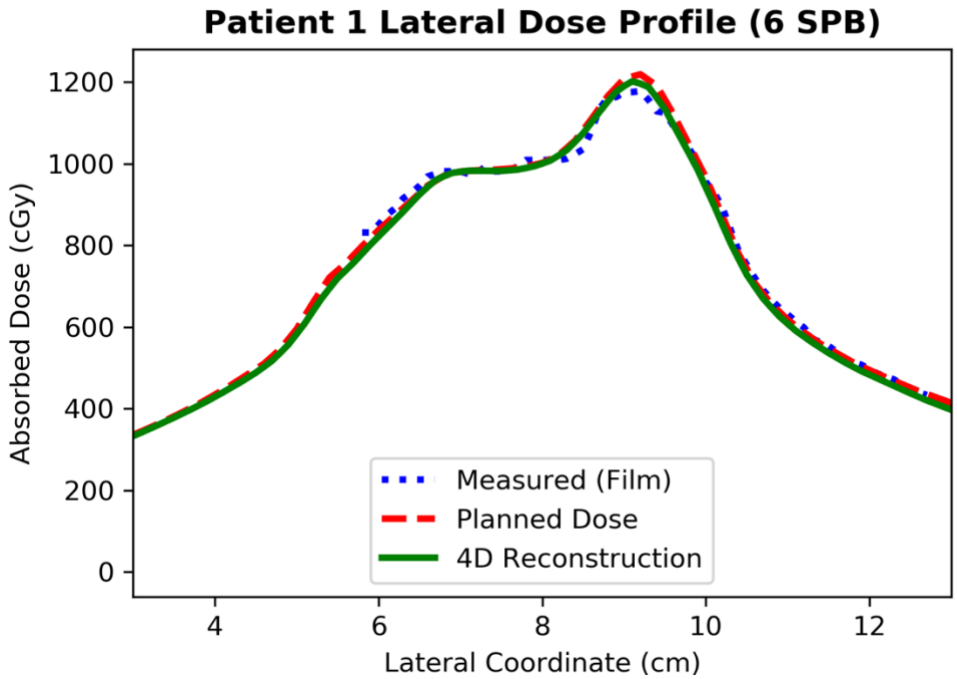

Figure B.2. Lateral dose profiles showing film measurement, treatment plan, and 4D reconstructed dose, for Patient 1 at a breathing rate of 6 SPB.

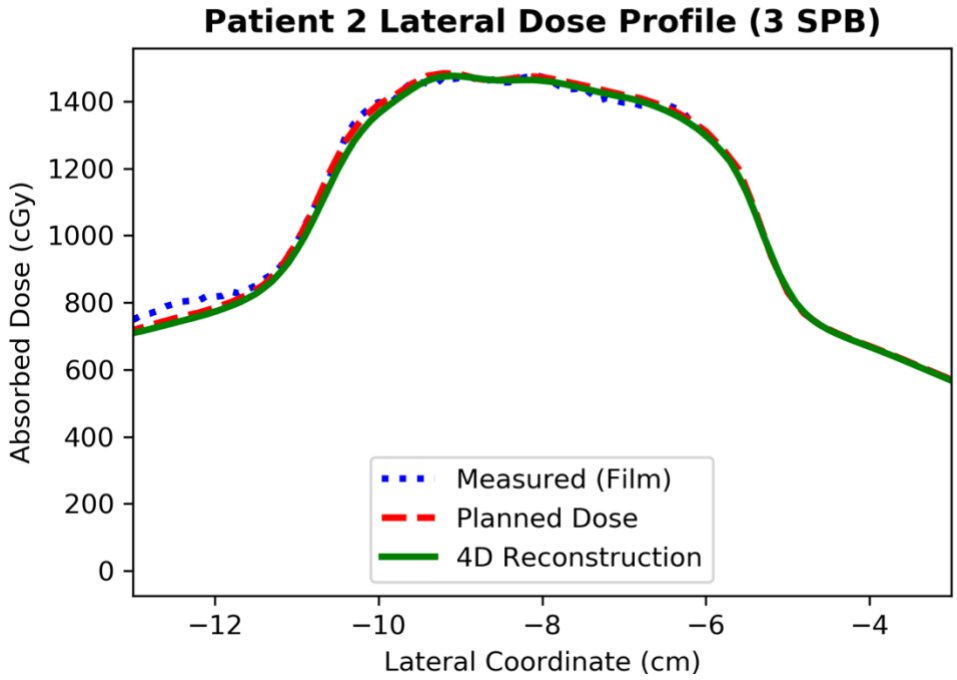

Figure B.3. Lateral dose profiles showing film measurement, treatment plan, and 4D reconstructed dose, for Patient 2 at a breathing rate of 3 SPB.

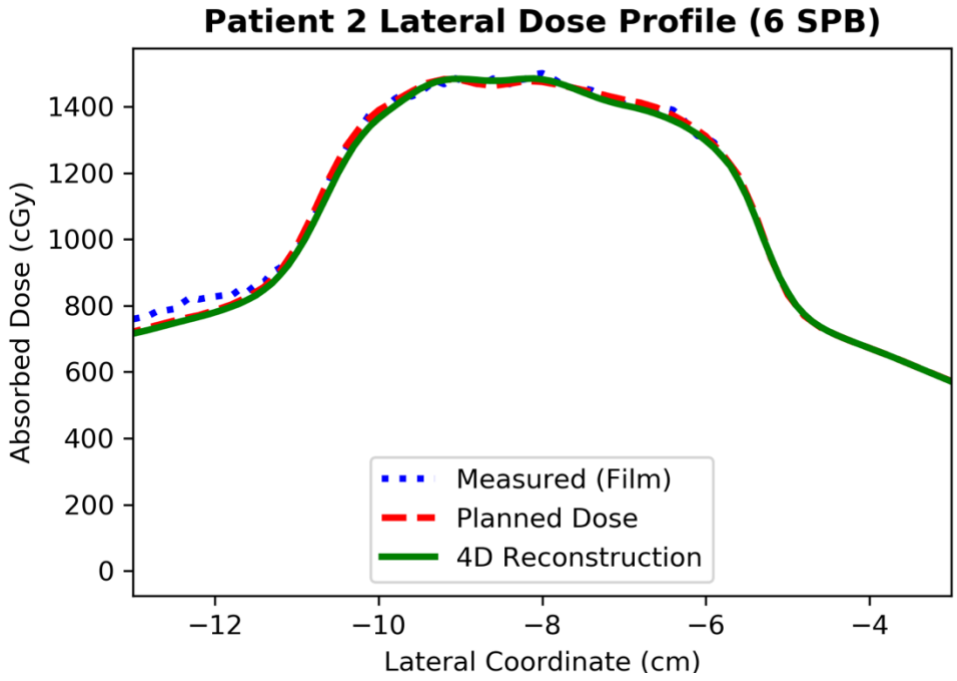

Figure B.4. Lateral dose profiles showing film measurement, treatment plan, and 4D reconstructed dose, for Patient 2 at a breathing rate of 6 SPB.

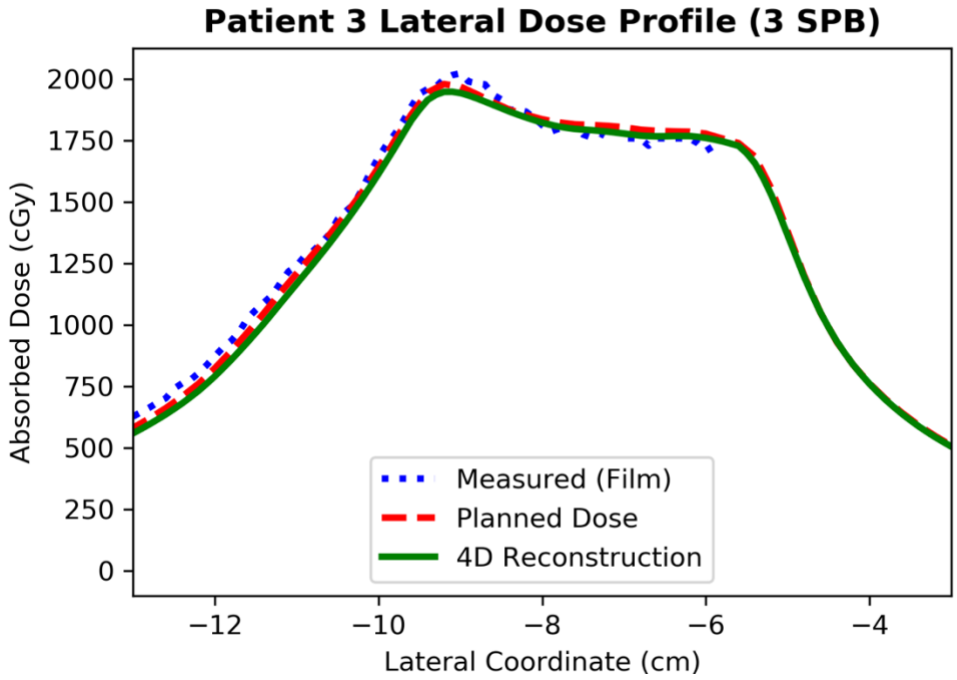

Figure B.5. Lateral dose profiles showing film measurement, treatment plan, and 4D reconstructed dose, for Patient 3 at a breathing rate of 3 SPB.

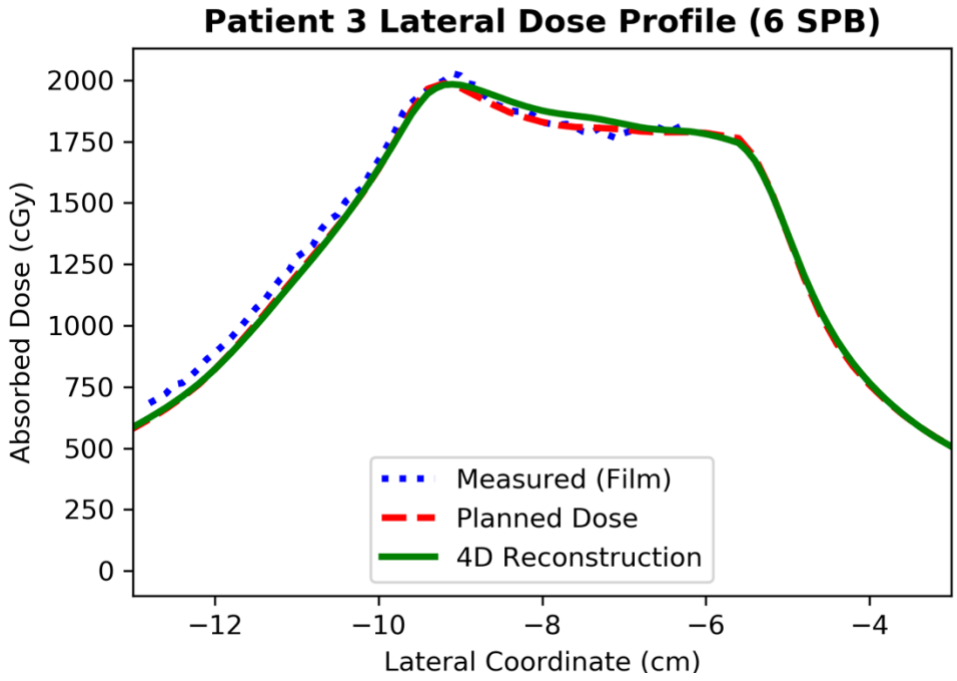

Figure B.6. Lateral dose profiles showing film measurement, treatment plan, and 4D reconstructed dose, for Patient 3 at a breathing rate of 6 SPB.

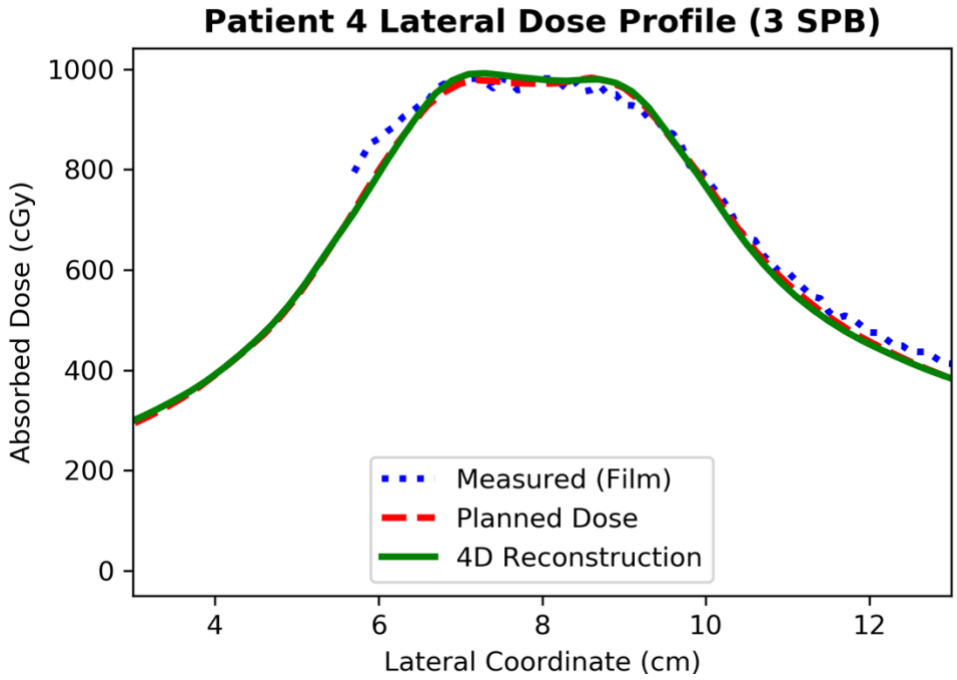

Figure B.7. Lateral dose profiles showing film measurement, treatment plan, and 4D reconstructed dose, for Patient 4 at a breathing rate of 3 SPB.

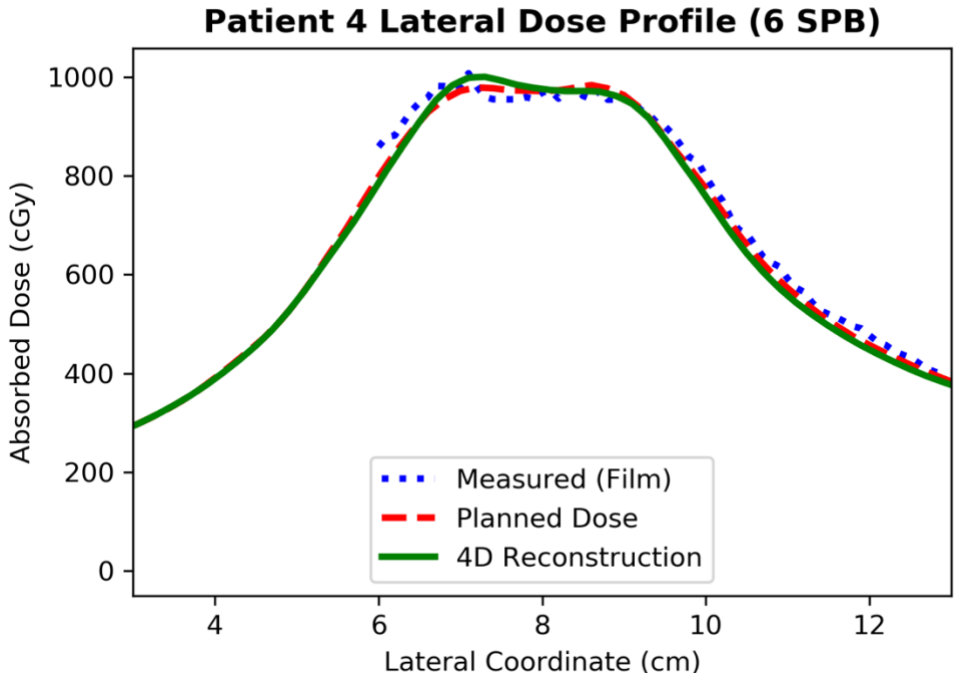

Figure B.8. Lateral dose profiles showing film measurement, treatment plan, and 4D reconstructed dose, for Patient 4 at a breathing rate of 6 SPB.

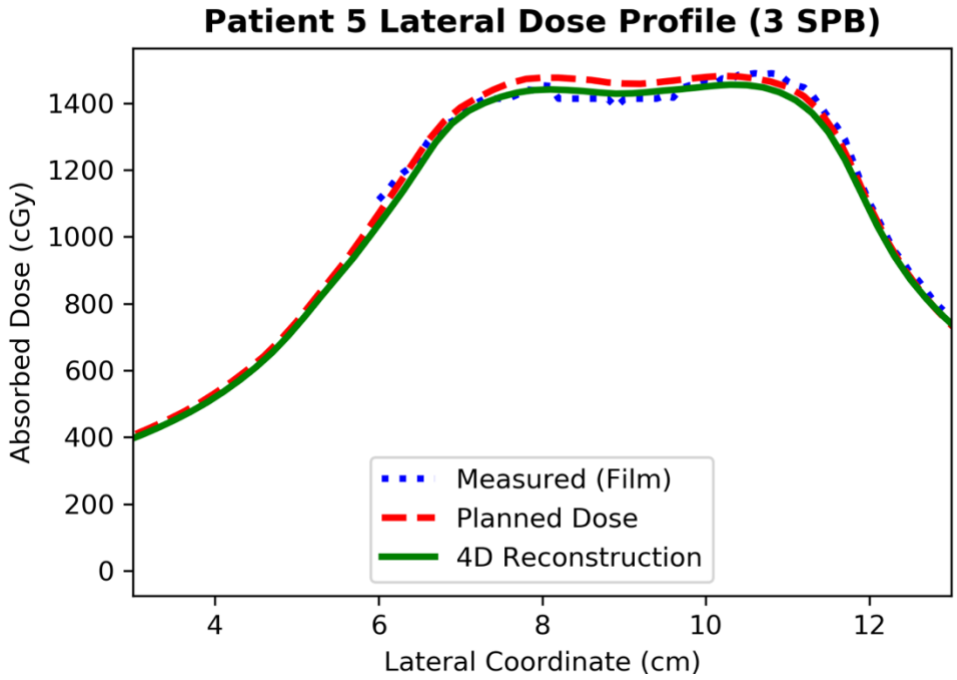

Figure B.9. Lateral dose profiles showing film measurement, treatment plan, and 4D reconstructed dose, for Patient 5 at a breathing rate of 3 SPB.

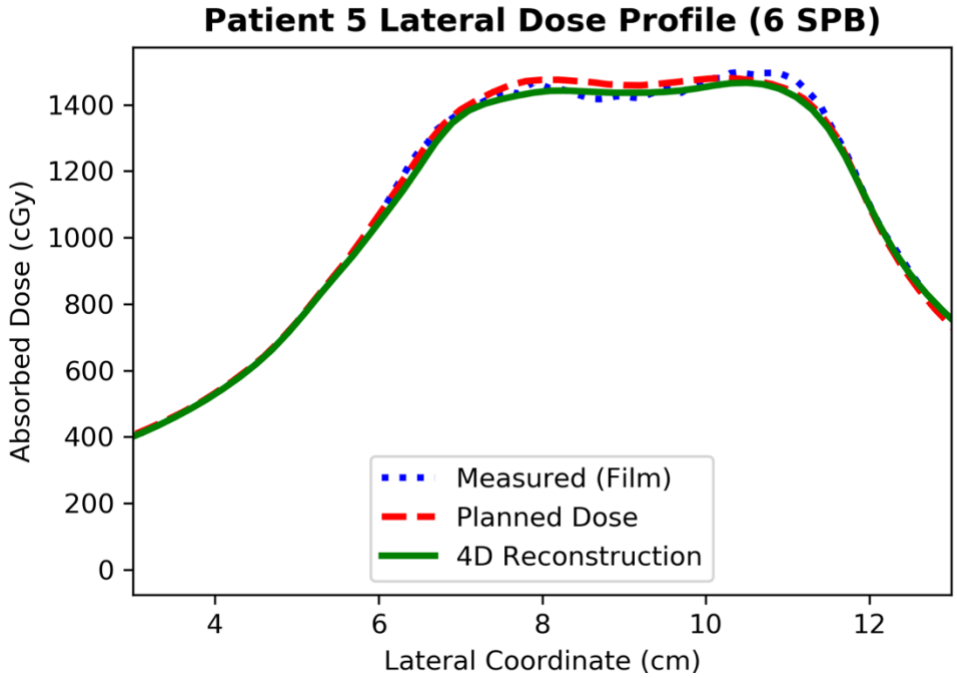

Figure B.10. Lateral dose profiles showing film measurement, treatment plan, and 4D reconstructed dose, for Patient 5 at a breathing rate of 6 SPB.

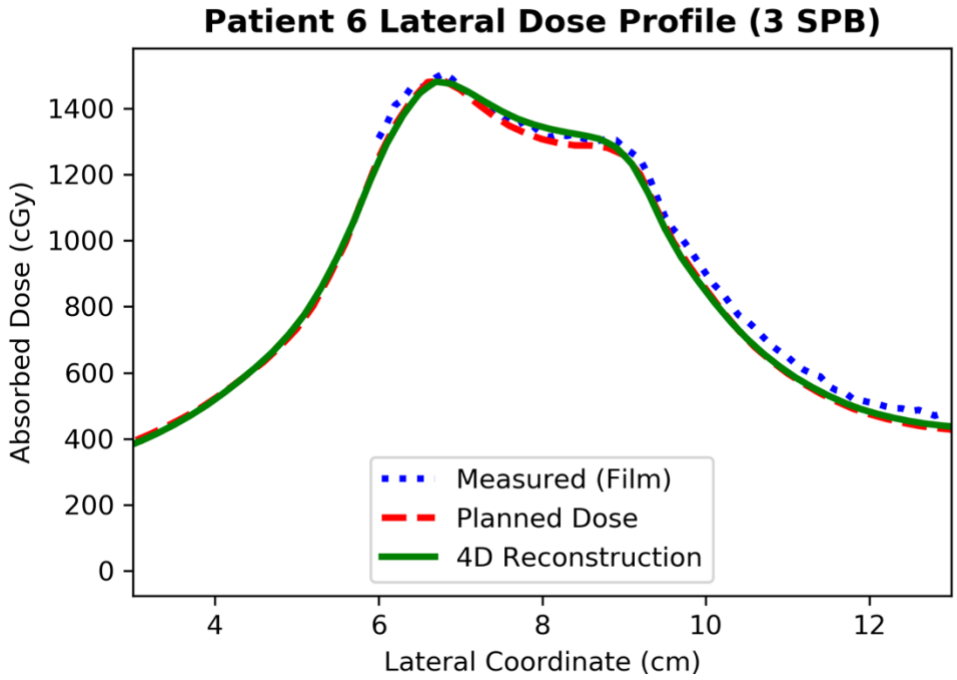

Figure B.11. Lateral dose profiles showing film measurement, treatment plan, and 4D reconstructed dose, for Patient 6 at a breathing rate of 3 SPB.

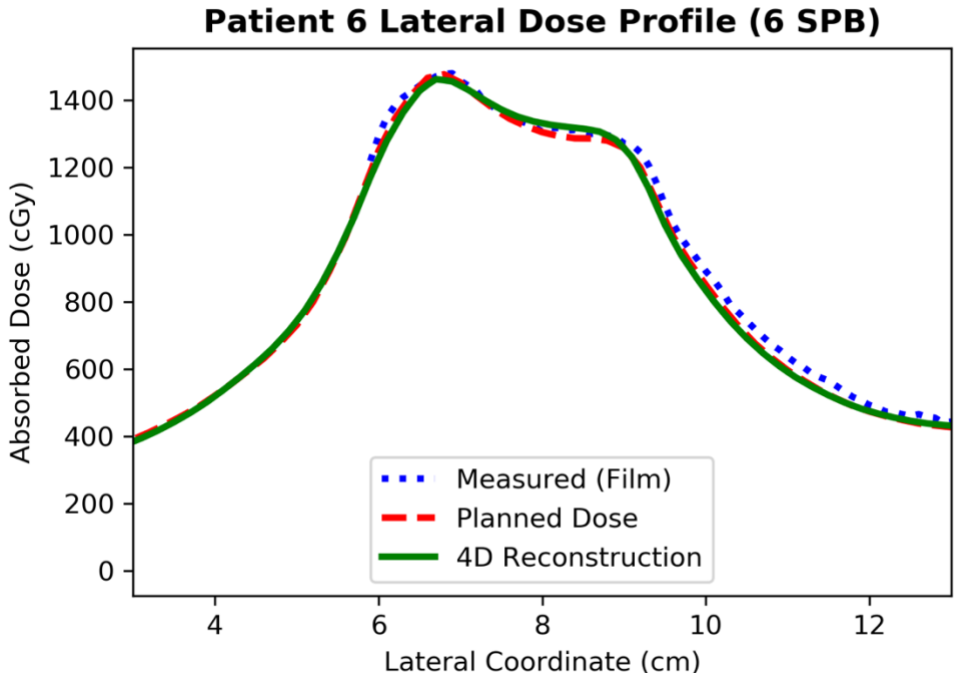

Figure B.12. Lateral dose profiles showing film measurement, treatment plan, and 4D reconstructed dose, for Patient 6 at a breathing rate of 6 SPB.

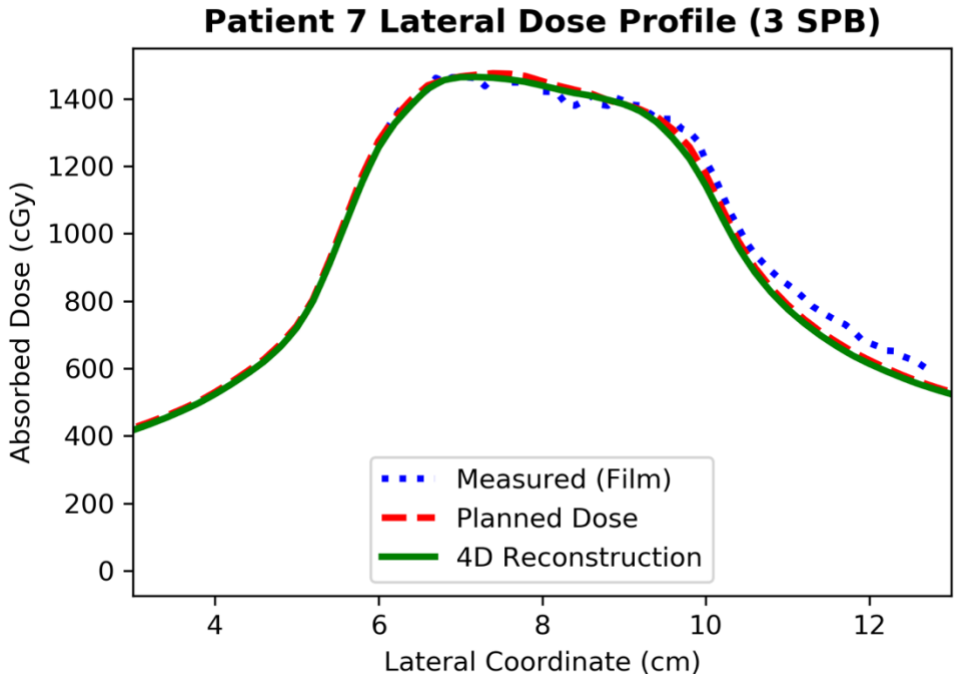

Figure B.13. Lateral dose profiles showing film measurement, treatment plan, and 4D reconstructed dose, for Patient 7 at a breathing rate of 3 SPB.

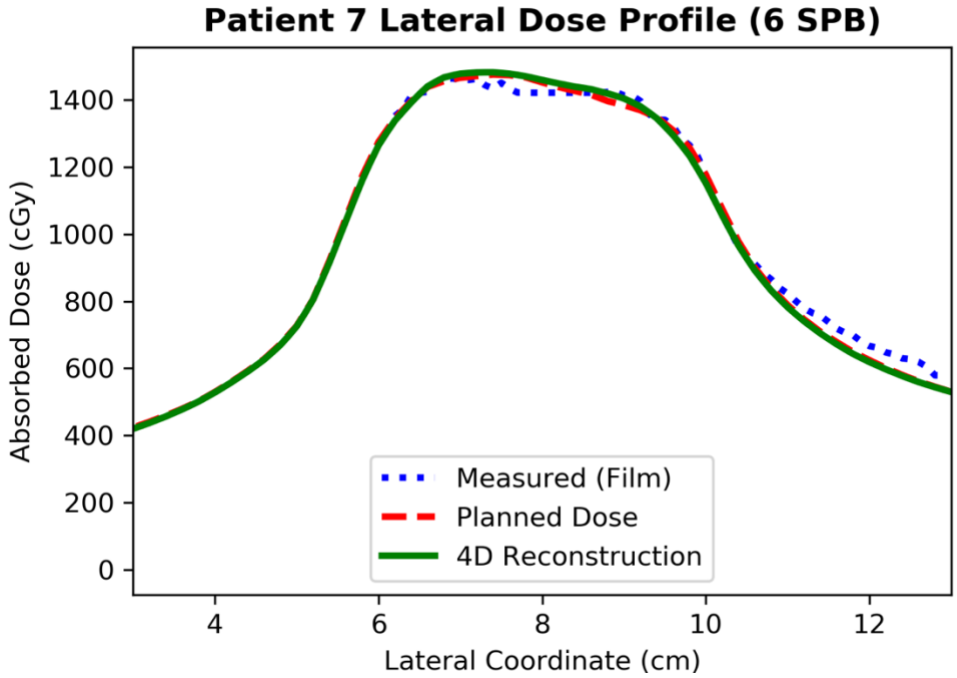

Figure B.14. Lateral dose profiles showing film measurement, treatment plan, and 4D reconstructed dose, for Patient 7 at a breathing rate of 6 SPB.

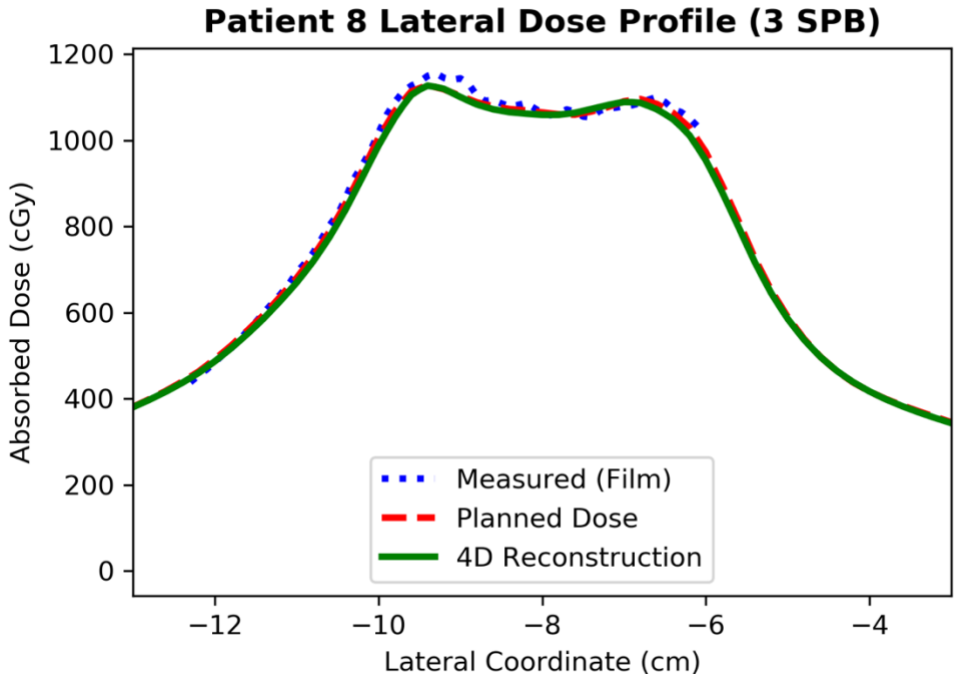

Figure B.15. Lateral dose profiles showing film measurement, treatment plan, and 4D reconstructed dose, for Patient 8 at a breathing rate of 3 SPB.

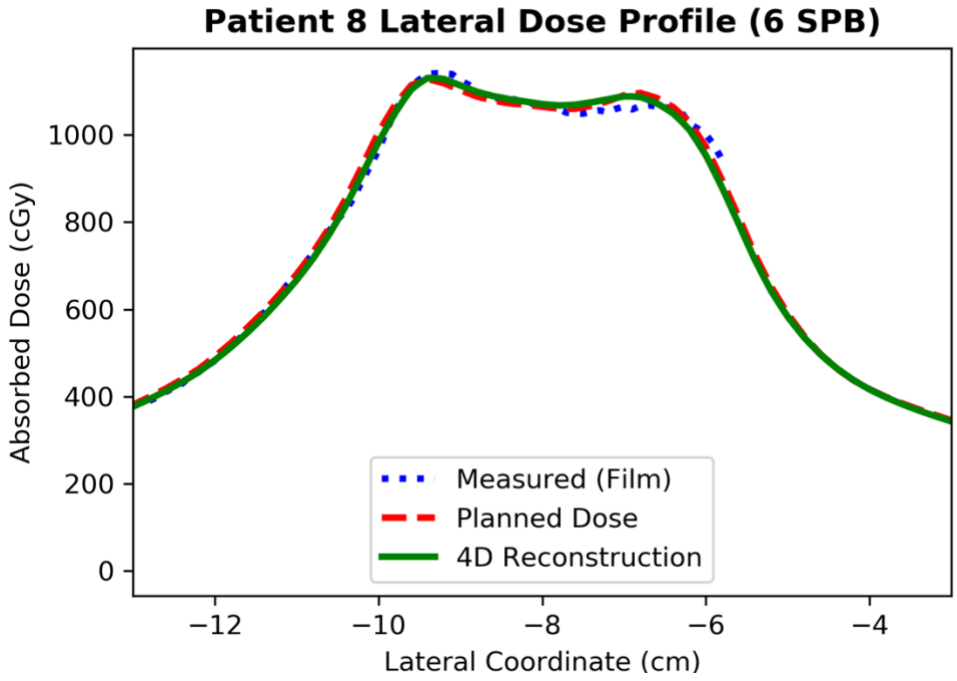

Figure B.16. Lateral dose profiles showing film measurement, treatment plan, and 4D reconstructed dose, for Patient 8 at a breathing rate of 6 SPB.

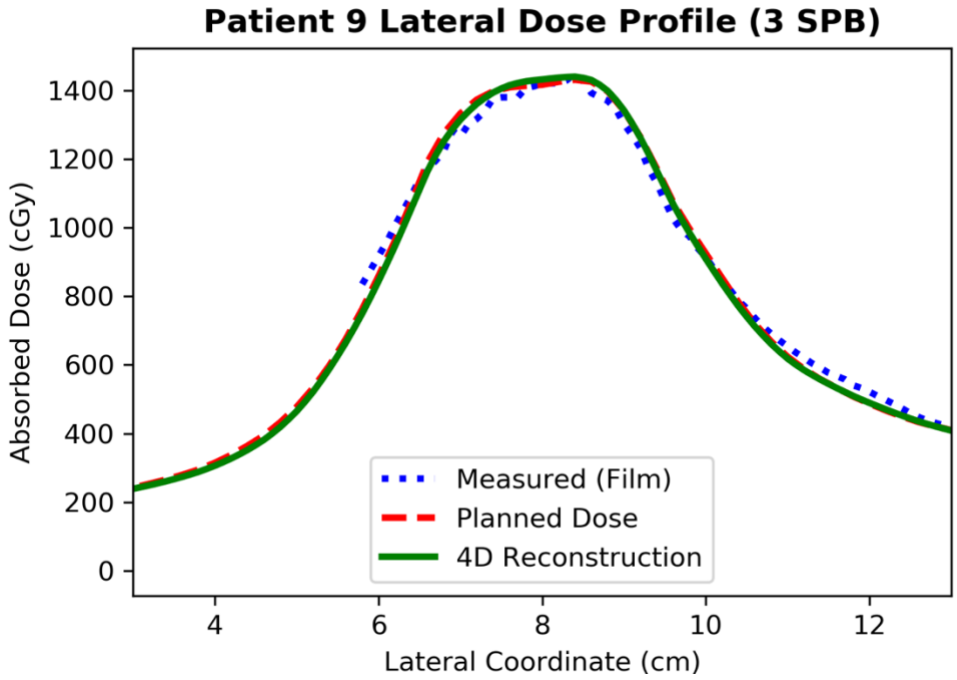

Figure B.17. Lateral dose profiles showing film measurement, treatment plan, and 4D reconstructed dose, for Patient 9 at a breathing rate of 3 SPB.

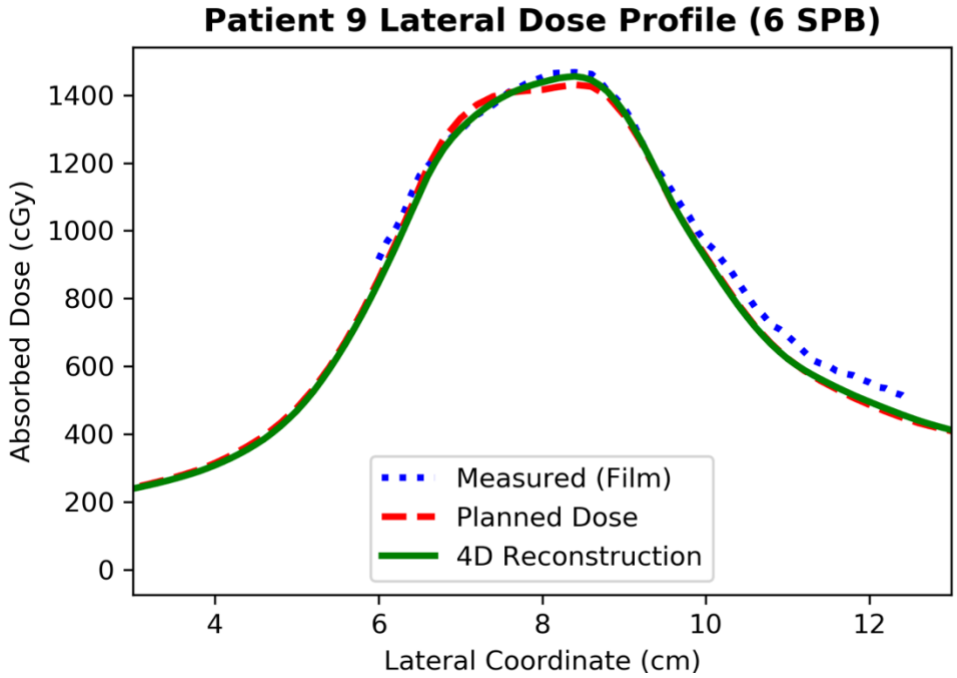

Figure B.18. Lateral dose profiles showing film measurement, treatment plan, and 4D reconstructed dose, for Patient 9 at a breathing rate of 6 SPB.

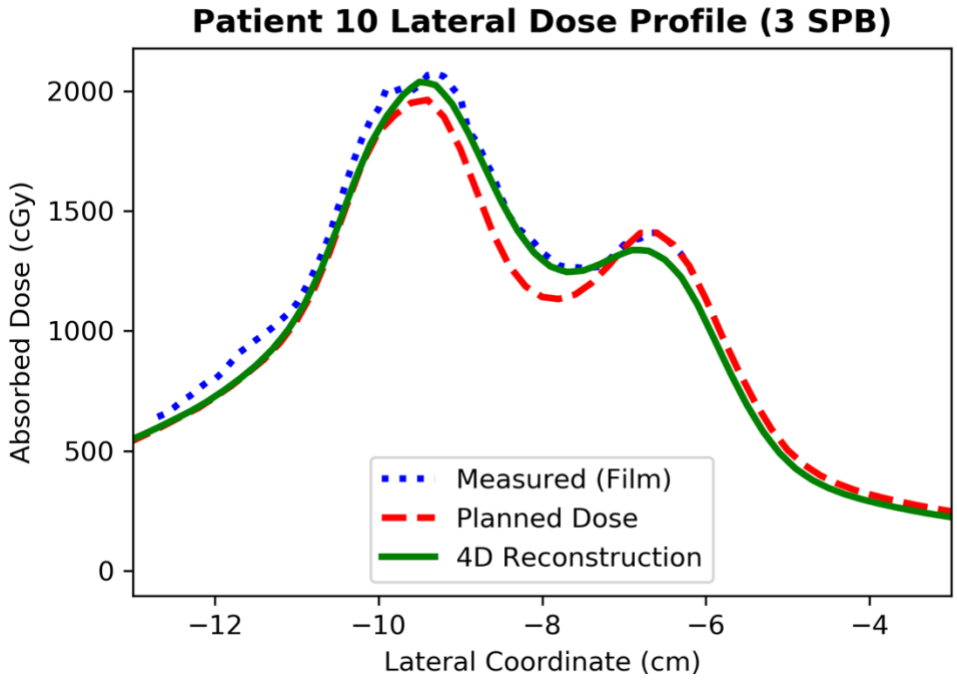

Figure B.19. Lateral dose profiles showing film measurement, treatment plan, and 4D reconstructed dose, for Patient 10 at a breathing rate of 3 SPB.

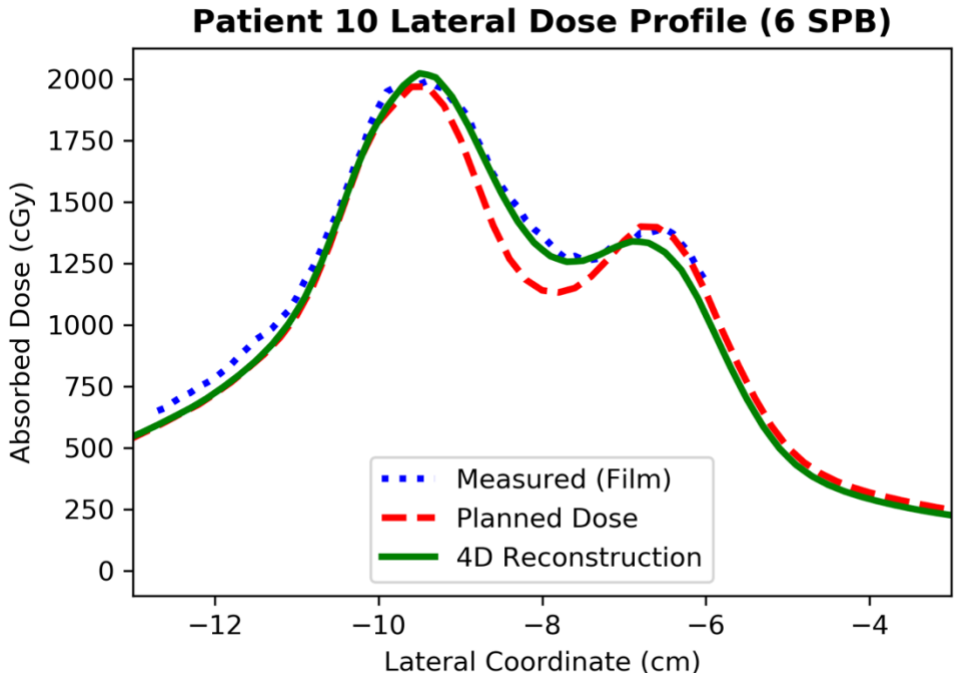

Figure B.20. Lateral dose profiles showing film measurement, treatment plan, and 4D reconstructed dose, for Patient 10 at a breathing rate of 6 SPB.

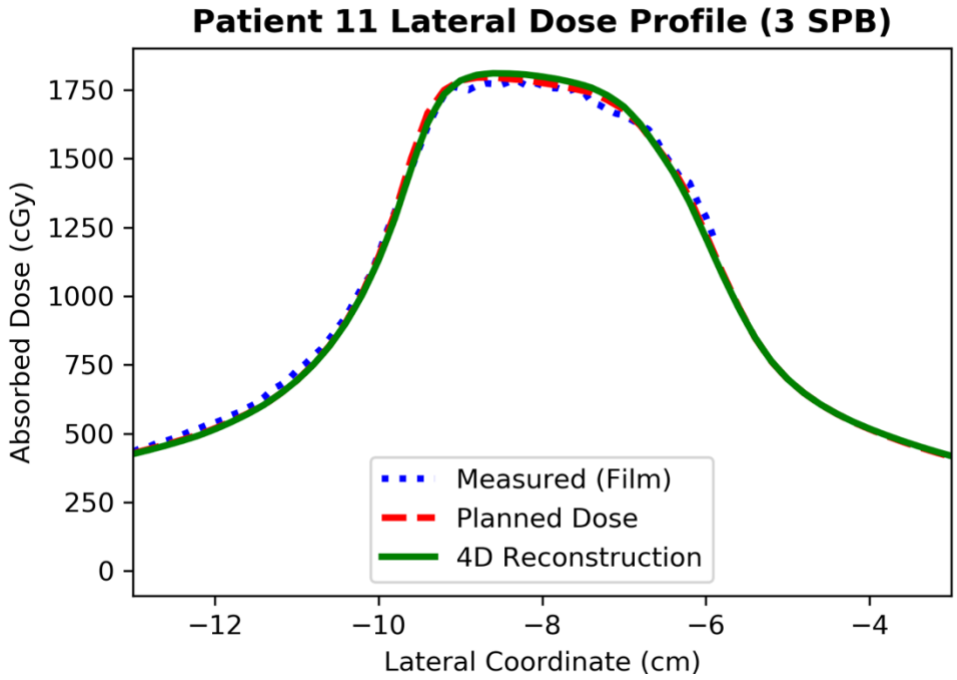

Figure B.21. Lateral dose profiles showing film measurement, treatment plan, and 4D reconstructed dose, for Patient 11 at a breathing rate of 3 SPB.

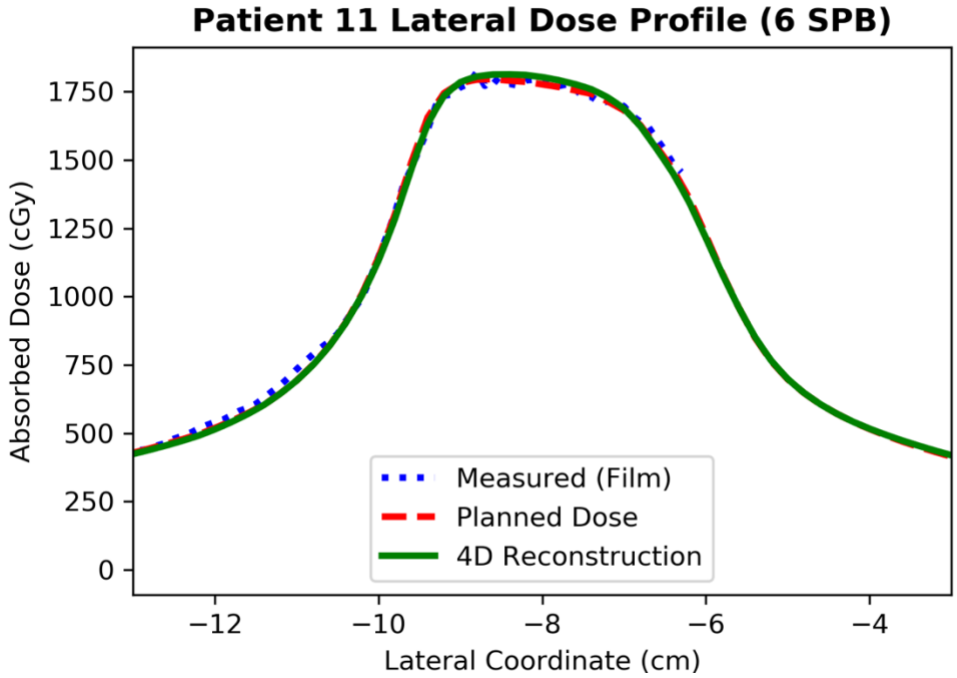

Figure B.22. Lateral dose profiles showing film measurement, treatment plan, and 4D reconstructed dose, for Patient 11 at a breathing rate of 6 SPB.

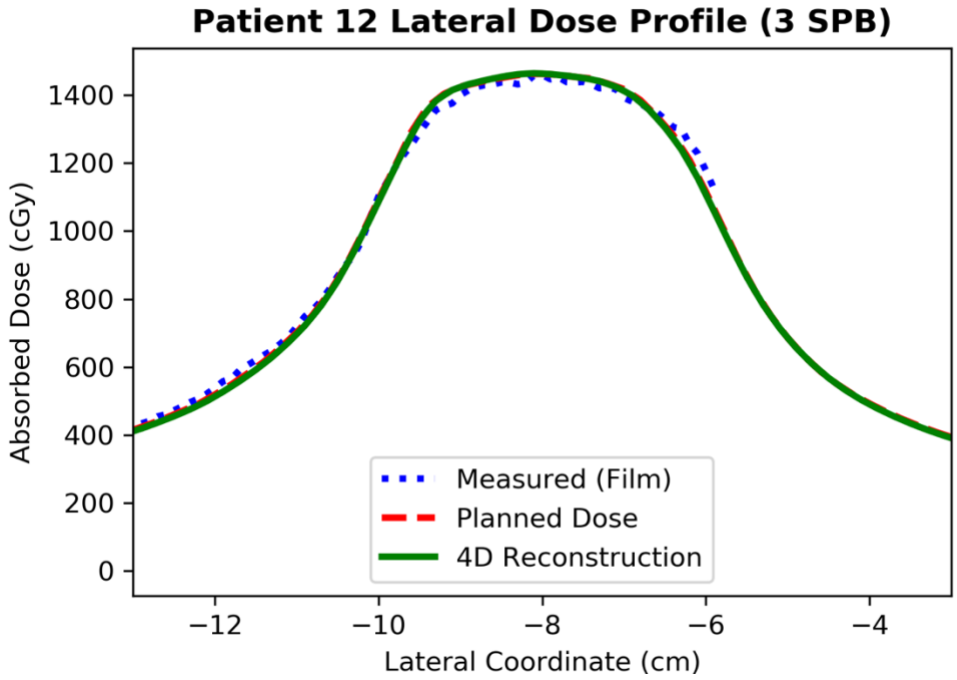

Figure B.23. Lateral dose profiles showing film measurement, treatment plan, and 4D reconstructed dose, for Patient 12 at a breathing rate of 3 SPB.

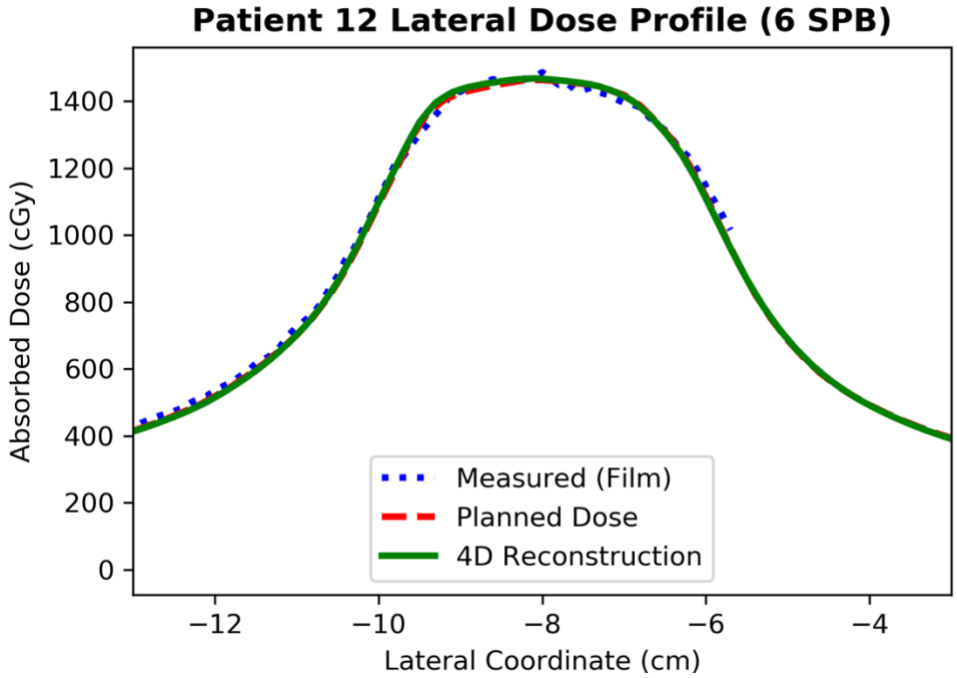

Figure B.24. Lateral dose profiles showing film measurement, treatment plan, and 4D reconstructed dose, for Patient 12 at a breathing rate of 6 SPB.

Appendix C. Gamma Analysis

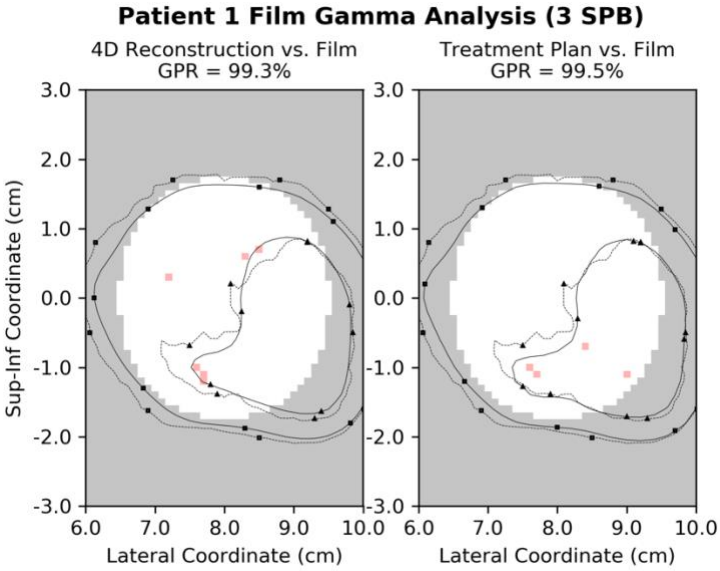

Figure C.1. Gamma map (global 3%, 2mm) for 4D reconstruction and treatment plan vs. film measurement, within MIP extent, for Patient 1 with breathing rate 3 SPB. Color legend: (Gray: Point not included in calculation; White: Passing point; Red: Failing point. Circle and square markers indicate 70% and 85% isodose contour and dashed and solid lines indicate film and calculated dose, respectively.

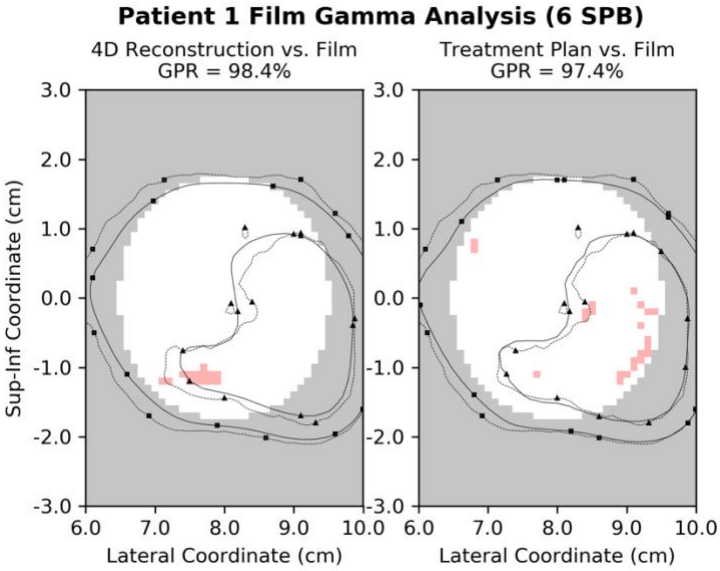

Figure C.2. Gamma map (global 3%, 2mm) for 4D reconstruction and treatment plan vs. film measurement, within MIP extent, for Patient 1 with breathing rate 6 SPB. Color legend: Gray: Point not included in calculation; White: Passing point; Red: Failing point.

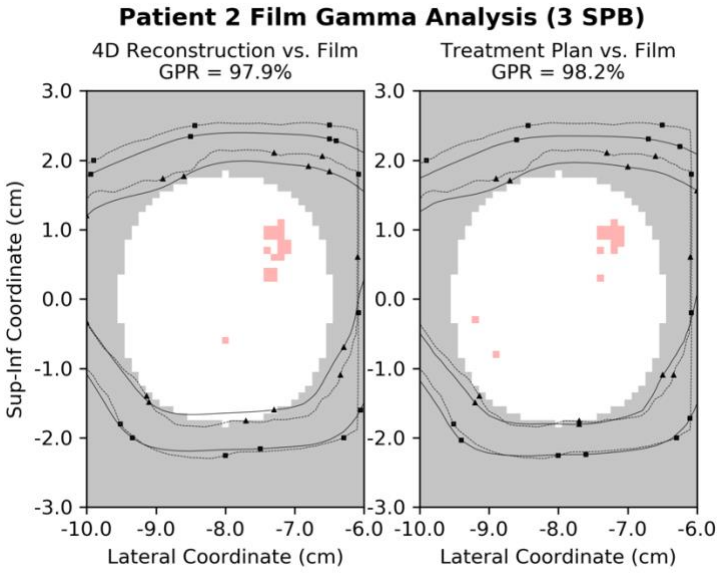

Figure C.3. Gamma map (global 3%, 2mm) for 4D reconstruction and treatment plan vs. film measurement, within MIP extent, for Patient 2 with breathing rate 3 SPB. Color legend: Gray: Point not included in calculation; White: Passing point; Red: Failing point. Circle and square markers indicate 70% and 85% isodose contour. Dashed and solid lines indicate film and calculated dose, respectively.

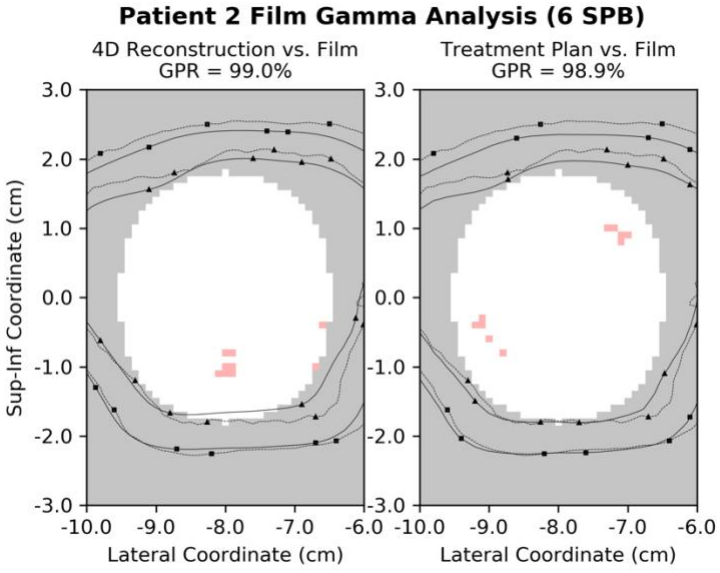

Figure C.4. Gamma map (global 3%, 2mm) for 4D reconstruction and treatment plan vs. film measurement, within MIP extent, for Patient 2 with breathing rate 6 SPB. Color legend: Gray: Point not included in calculation; White: Passing point; Red: Failing point. Circle and square markers indicate 70% and 85% isodose contour. Dashed and solid lines indicate film and calculated dose, respectively.

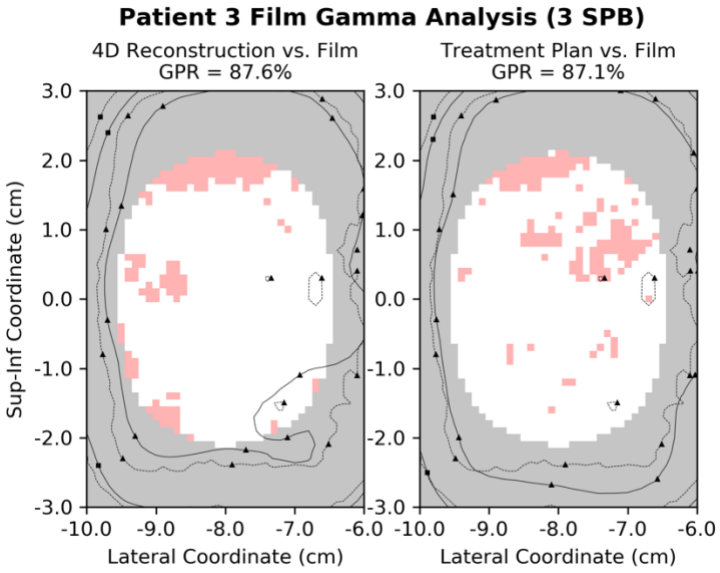

Figure C.5. Gamma map (global 3%, 2mm) for 4D reconstruction and treatment plan vs. film measurement, within MIP extent, for Patient 3 with breathing rate 3 SPB. Color legend: Gray: Point not included in calculation; White: Passing point; Red: Failing point. Circle and square markers indicate 70% and 85% isodose contour. Dashed and solid lines indicate film and calculated dose, respectively.

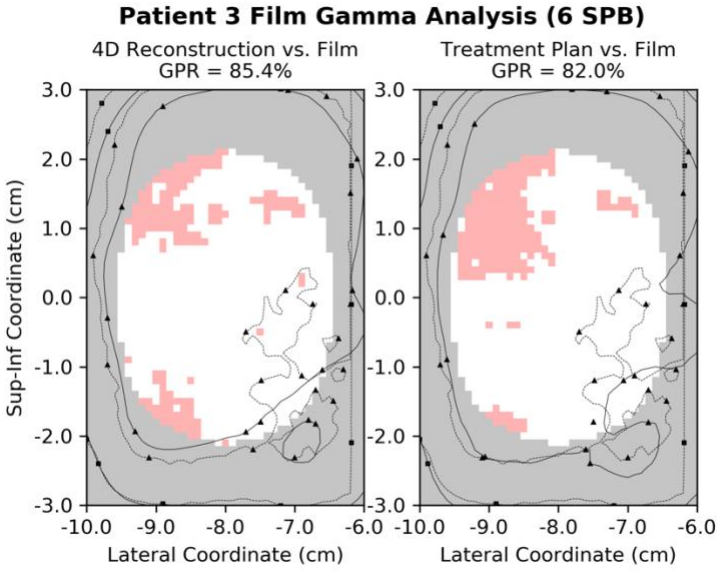

Figure C.6. Gamma map (global 3%, 2mm) for 4D reconstruction and treatment plan vs. film measurement, within MIP extent, for Patient 3 with breathing rate 6 SPB. Color legend: Gray: Point not included in calculation; White: Passing point; Red: Failing point. Circle and square markers indicate 70% and 85% isodose contour. Dashed and solid lines indicate film and calculated dose, respectively.

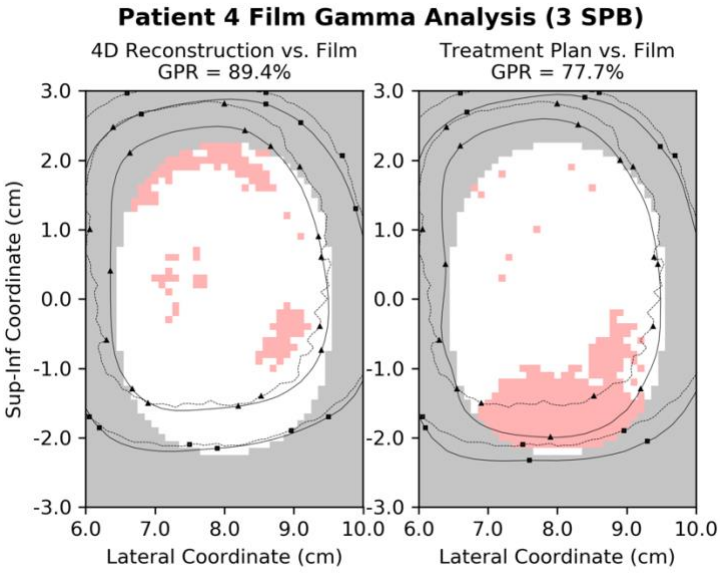

Figure C.7. Gamma map (global 3%, 2mm) for 4D reconstruction and treatment plan vs. film measurement, within MIP extent, for Patient 4 with breathing rate 3 SPB. Color legend: Gray: Point not included in calculation; White: Passing point; Red: Failing point. Circle and square markers indicate 70% and 85% isodose contour. Dashed and solid lines indicate film and calculated dose, respectively.

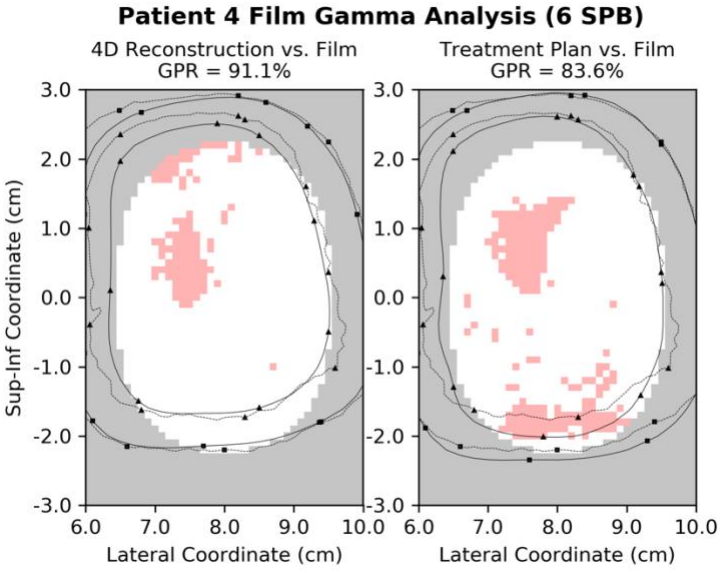

Figure C.8. Gamma map (global 3%, 2mm) for 4D reconstruction and treatment plan vs. film measurement, within MIP extent, for Patient 4 with breathing rate 6 SPB. Color legend: Gray: Point not included in calculation; White: Passing point; Red: Failing point. Circle and square markers indicate 70% and 85% isodose contour. Dashed and solid lines indicate film and calculated dose, respectively.

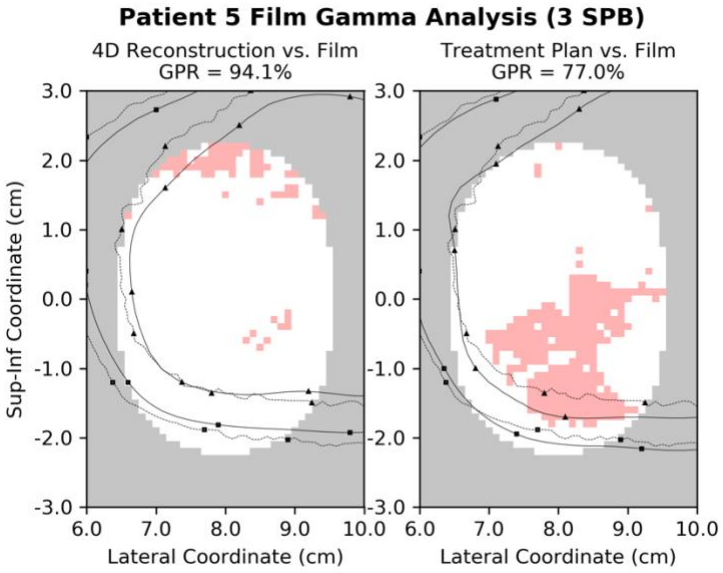

Figure C.9. Gamma map (global 3%, 2mm) for 4D reconstruction and treatment plan vs. film measurement, within MIP extent, for Patient 5 with breathing rate 6 SPB. Color legend: Gray: Point not included in calculation; White: Passing point; Red: Failing point. Circle and square markers indicate 70% and 85% isodose contour. Dashed and solid lines indicate film and calculated dose, respectively.

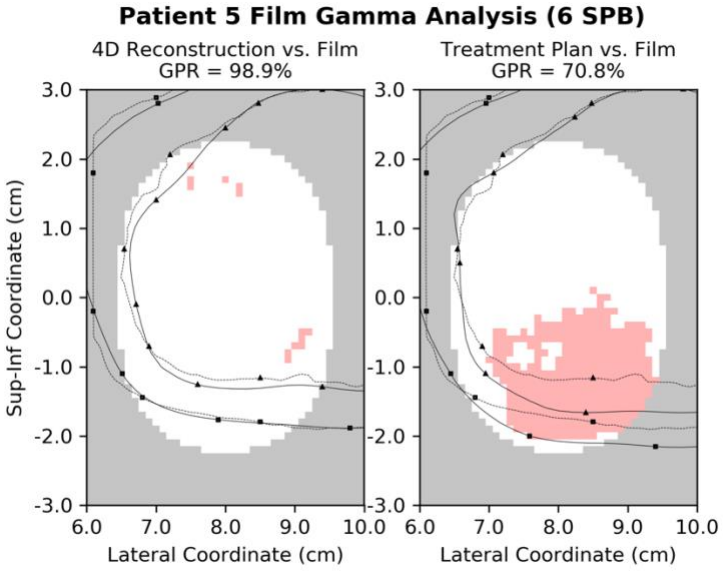

Figure C.10. Gamma map (global 3%, 2mm) for 4D reconstruction and treatment plan vs. film measurement, within MIP extent, for Patient 5 with breathing rate 6 SPB. Color legend: Gray: Point not included in calculation; White: Passing point; Red: Failing point. Circle and square markers indicate 70% and 85% isodose contour. Dashed and solid lines indicate film and calculated dose, respectively.

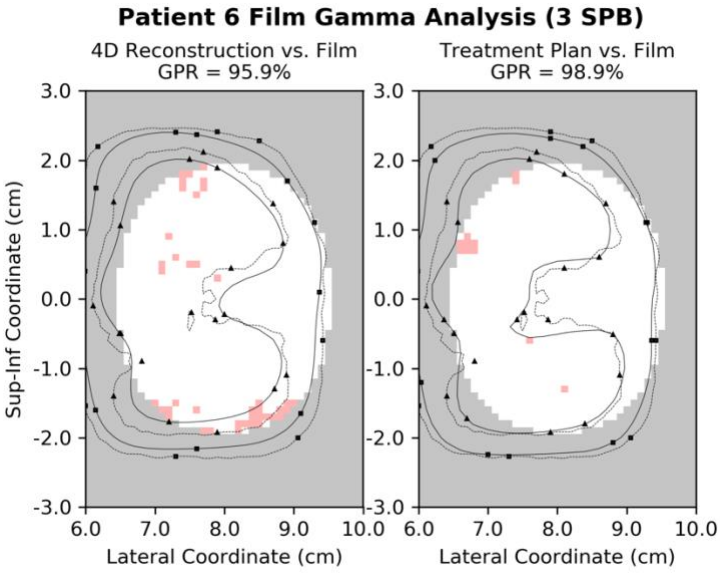

Figure C.11. Gamma map (global 3%, 2mm) for 4D reconstruction and treatment plan vs. film measurement, within MIP extent, for Patient 6 with breathing rate 3 SPB. Color legend: Gray: Point not included in calculation; White: Passing point; Red: Failing point. Circle and square markers indicate 70% and 85% isodose contour. Dashed and solid lines indicate film and calculated dose, respectively.

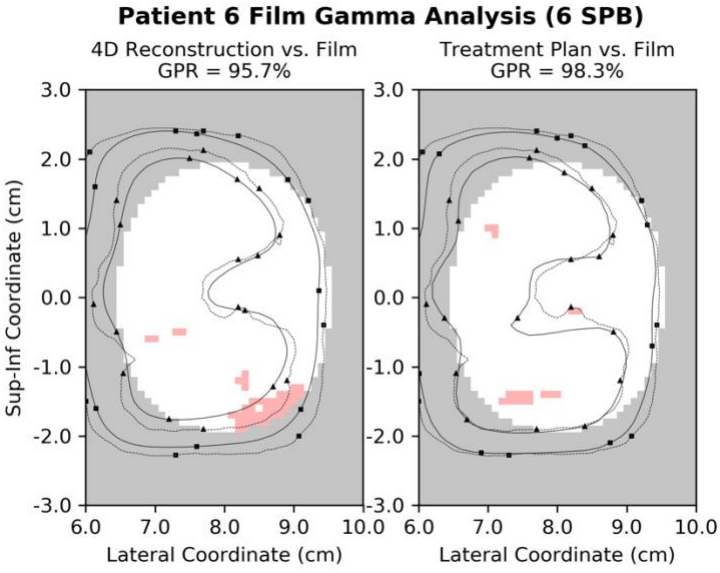

Figure C.12. Gamma map (global 3%, 2mm) for 4D reconstruction and treatment plan vs. film measurement, within MIP extent, for Patient 6 with breathing rate 6 SPB. Color legend: Gray: Point not included in calculation; White: Passing point; Red: Failing point. Circle and square markers indicate 70% and 85% isodose contour. Dashed and solid lines indicate film and calculated dose, respectively.

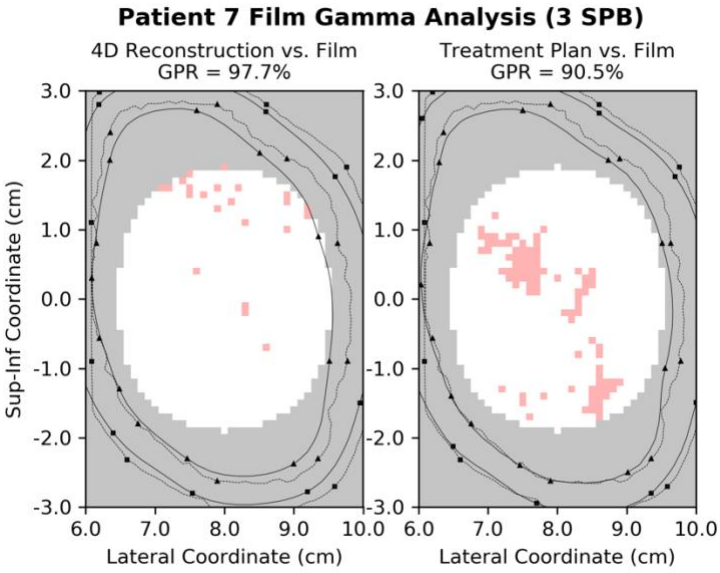

Figure C.13. Gamma map (global 3%, 2mm) for 4D reconstruction and treatment plan vs. film measurement, within MIP extent, for Patient 7 with breathing rate 3 SPB. Color legend: Gray: Point not included in calculation; White: Passing point; Red: Failing point. Circle and square markers indicate 70% and 85% isodose contour. Dashed and solid lines indicate film and calculated dose, respectively.

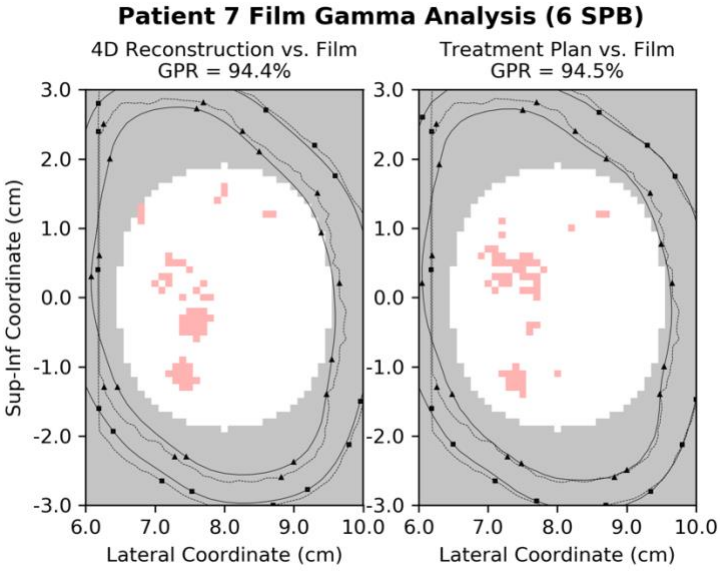

Figure C.14. Gamma map (global 3%, 2mm) for 4D reconstruction and treatment plan vs. film measurement, within MIP extent, for Patient 7 with breathing rate 6 SPB. Color legend: Gray: Point not included in calculation; White: Passing point; Red: Failing point. Circle and square markers indicate 70% and 85% isodose contour. Dashed and solid lines indicate film and calculated dose, respectively.

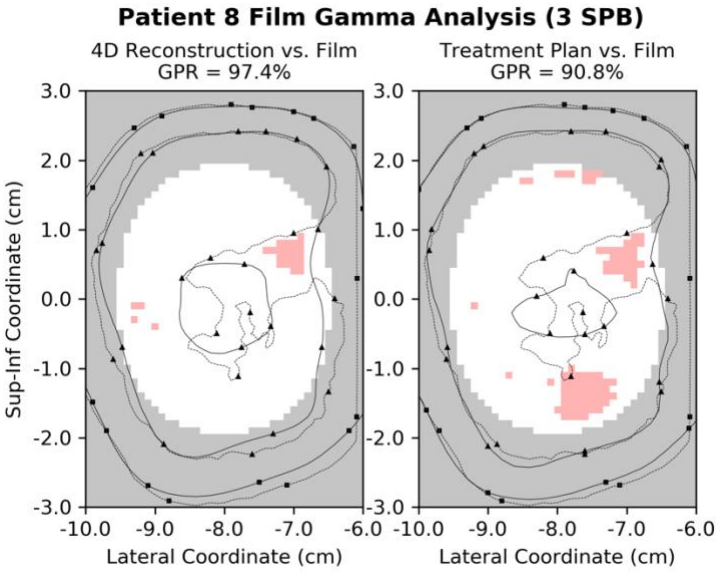

Figure C.15. Gamma map (global 3%, 2mm) for 4D reconstruction and treatment plan vs. film measurement, within MIP extent, for Patient 8 with breathing rate 3 SPB. Color legend: Gray: Point not included in calculation; White: Passing point; Red: Failing point. Circle and square markers indicate 70% and 85% isodose contour. Dashed and solid lines indicate film and calculated dose, respectively.

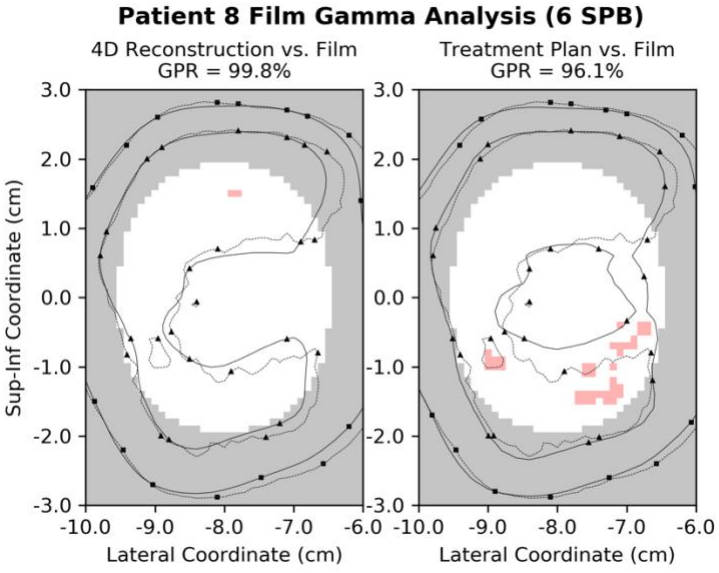

Figure C.16. Gamma map (global 3%, 2mm) for 4D reconstruction and treatment plan vs. film measurement, within MIP extent, for Patient 8 with breathing rate 6 SPB. Color legend: Gray: Point not included in calculation; White: Passing point; Red: Failing point. Circle and square markers indicate 70% and 85% isodose contour. Dashed and solid lines indicate film and calculated dose, respectively.

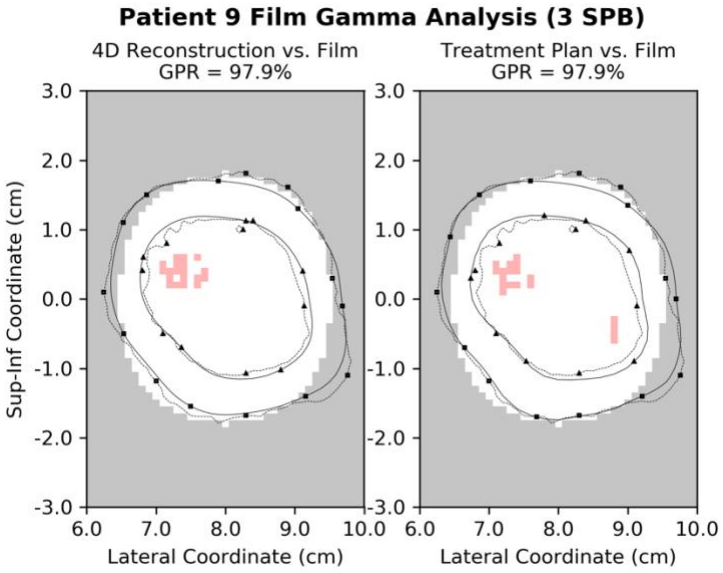

Figure C.17. Gamma map (global 3%, 2mm) for 4D reconstruction and treatment plan vs. film measurement, within MIP extent, for Patient 9 with breathing rate 3 SPB. Color legend: Gray: Point not included in calculation; White: Passing point; Red: Failing point. Circle and square markers indicate 70% and 85% isodose contour. Dashed and solid lines indicate film and calculated dose, respectively.

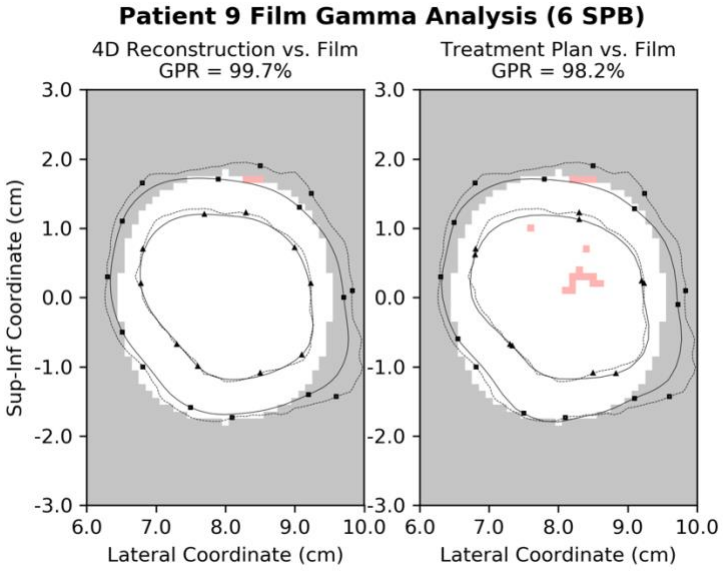

Figure C.18. Gamma map (global 3%, 2mm) for 4D reconstruction and treatment plan vs. film measurement, within MIP extent, for Patient 9 with breathing rate 6 SPB. Color legend: Gray: Point not included in calculation; White: Passing point; Red: Failing point. Circle and square markers indicate 70% and 85% isodose contour. Dashed and solid lines indicate film and calculated dose, respectively.

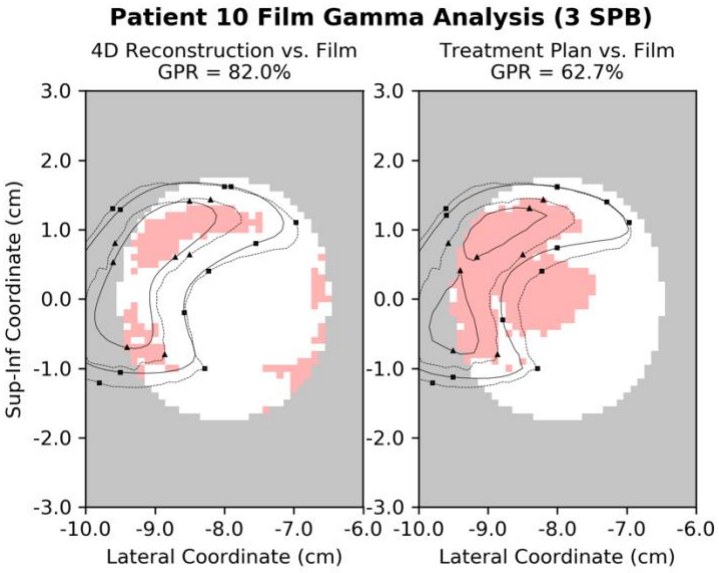

Figure C.19. Gamma map (global 3%, 2mm) for 4D reconstruction and treatment plan vs. film measurement, within MIP extent, for Patient 10 with breathing rate 3 SPB. Color legend: Gray: Point not included in calculation; White: Passing point; Red: Failing point. Circle and square markers indicate 70% and 85% isodose contour. Dashed and solid lines indicate film and calculated dose, respectively.

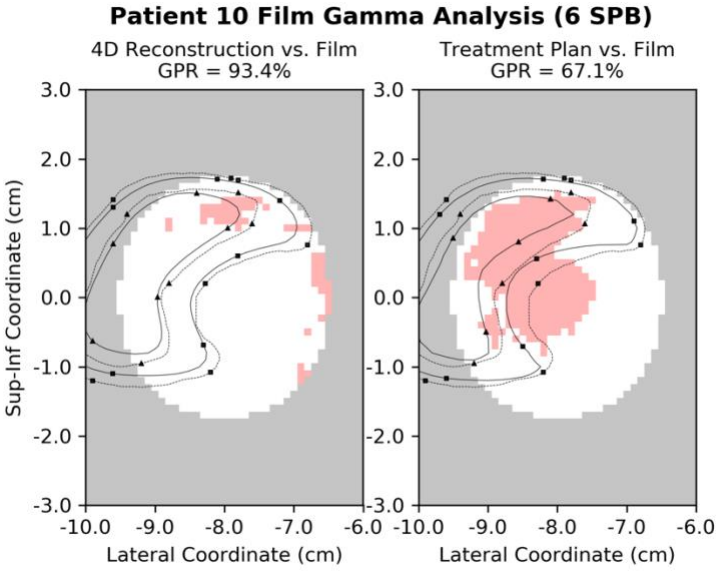

Figure C.20. Gamma map (global 3%, 2mm) for 4D reconstruction and treatment plan vs. film measurement, within MIP extent, for Patient 10 with breathing rate 6 SPB. Color legend: Gray: Point not included in calculation; White: Passing point; Red: Failing point. Circle and square markers indicate 70% and 85% isodose contour. Dashed and solid lines indicate film and calculated dose, respectively.

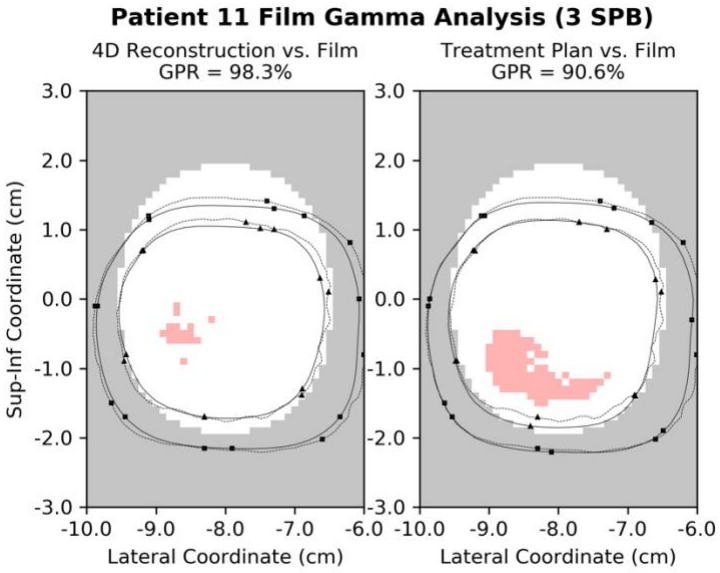

Figure C.21. Gamma map (global 3%, 2mm) for 4D reconstruction and treatment plan vs. film measurement, within MIP extent, for Patient 11 with breathing rate 3 SPB. Color legend: Gray: Point not included in calculation; White: Passing point; Red: Failing point. Circle and square markers indicate 70% and 85% isodose contour. Dashed and solid lines indicate film and calculated dose, respectively.

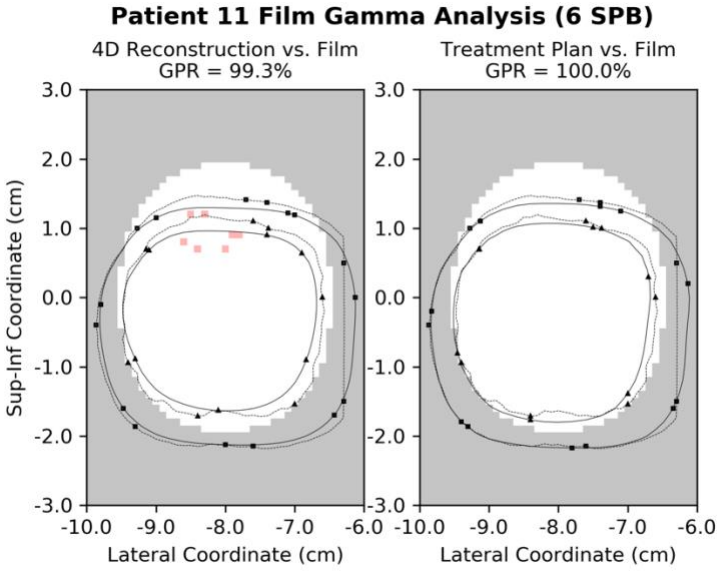

Figure C.22. Gamma map (global 3%, 2mm) for 4D reconstruction and treatment plan vs. film measurement, within MIP extent, for Patient 11 with breathing rate 6 SPB. Color legend: Gray: Point not included in calculation; White: Passing point; Red: Failing point. Circle and square markers indicate 70% and 85% isodose contour. Dashed and solid lines indicate film and calculated dose, respectively.

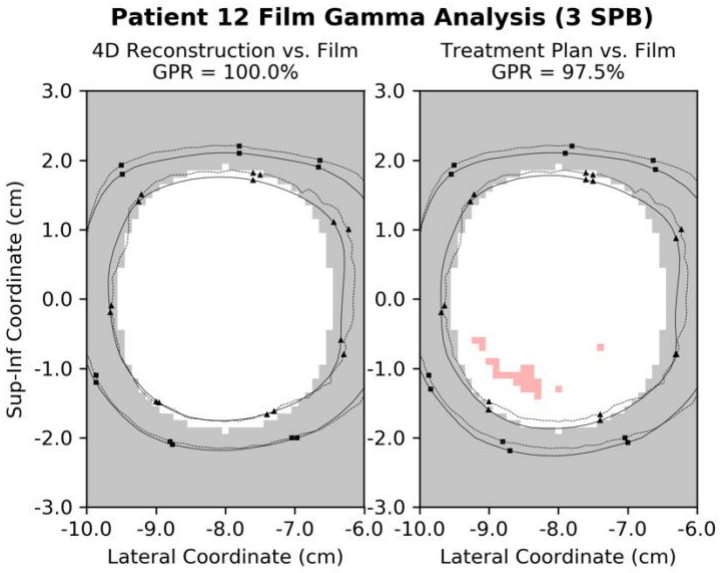

Figure C.23. Gamma map (global 3%, 2mm) for 4D reconstruction and treatment plan vs. film measurement, within MIP extent, for Patient 12 with breathing rate 3 SPB. Color legend: Gray: Point not included in calculation; White: Passing point; Red: Failing point. Circle and square markers indicate 70% and 85% isodose contour. Dashed and solid lines indicate film and calculated dose, respectively.

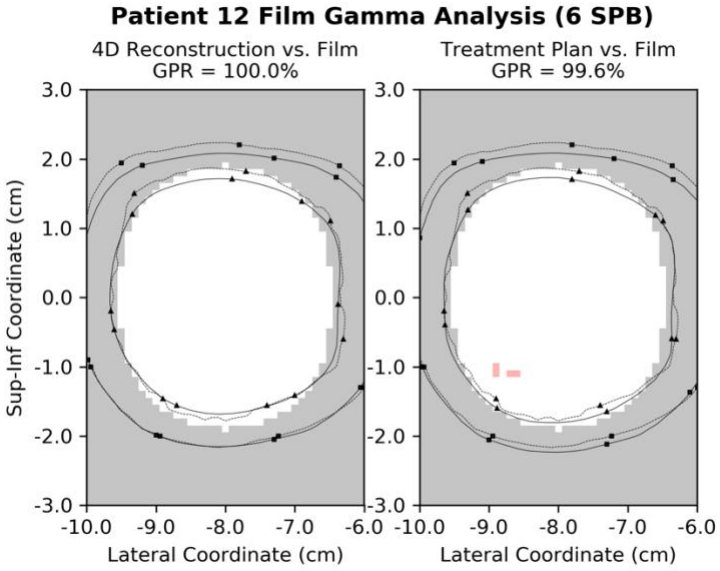

Figure C.24. Gamma map (global 3%, 2mm) for 4D reconstruction and treatment plan vs. film measurement, within MIP extent, for Patient 12 with breathing rate 6 SPB. Color legend: Gray: Point not included in calculation; White: Passing point; Red: Failing point. Circle and square markers indicate 70% and 85% isodose contour. Dashed and solid lines indicate film and calculated dose, respectively.

References

Ashland, "GAFCHROMIC™ DOSIMETRY MEDIA, TYPE EBT-3", (2020).

Benedict, S. H., Yenice, K. M., Followill, D., Galvin, J. M., Hinson, W., Kavanagh, B., Keall, P., Lovelock, M., Meeks, S., Papiez, L., Purdie, T., Sadagopan, R., Schell, M. C., Salter, B., Schlesinger, D. J., Shiu, A. S., Solberg, T., Song, D. Y., Stieber, V., Timmerman, R., Tome, W. A., Verellen, D., Wang, L., and Yin, F. F., "Stereotactic body radiation therapy: the report of AAPM Task Group 101," Med Phys **37** (8), 4078-4101 (2010).

Bortfeld, T., Jokivarsi, K., Goitein, M., Kung, J., and Jiang, S. B., "Effects of intra-fraction motion on IMRT dose delivery: statistical analysis and simulation," Phys Med Biol **47** (13), 2203-2220 (2002).

Brandner, E. D., Chetty, I. J., Giaddui, T. G., Xiao, Y., and Huq, M. S., "Motion management strategies and technical issues associated with stereotactic body radiotherapy of thoracic and upper abdominal tumors: A review from NRG oncology," Med Phys **44** (6), 2595-2612 (2017).

Calusi, S., Labanca, G., Zani, M., Casati, M., Marrazzo, L., Noferini, L., Talamonti, C., Fusi, F., Desideri, I., Bonomo, P., Livi, L., and Pallotta, S., "A multiparametric method to assess the MIM deformable image registration algorithm," J Appl Clin Med Phys **20** (4), 75-82 (2019).

Casanova Borca, V., Pasquino, M., Russo, G., Grosso, P., Cante, D., Sciacero, P., Girelli, G., La Porta, M. R., and Tofani, S., "Dosimetric characterization and use of GAFCHROMIC EBT3 film for IMRT dose verification," J Appl Clin Med Phys **14** (2), 4111 (2013).

Chetty, I. J. and Rosu-Bubulac, M., "Deformable Registration for Dose Accumulation," Semin Radiat Oncol **29** (3), 198-208 (2019).

Chung, H., Jung, J., Jeong, C., Kwak, J., Park, J. H., Kim, S. S., Yoon, S. M., Song, S. Y., Kim, J. H., Choi, E. K., Cho, S., and Cho, B., "Evaluation of delivered dose to a moving target by 4D dose reconstruction in gated volumetric modulated arc therapy," PLoS One **13** (9), e0202765 (2018).

Court, L., Wagar, M., Berbeco, R., Reisner, A., Winey, B., Schofield, D., Ionascu, D., Allen, A. M., Popple, R., and Lingos, T., "Evaluation of the interplay effect when using RapidArc to treat targets moving in the craniocaudal or right-left direction," Med Phys **37** (1), 4-11 (2010).

Devic, S., Tomic, N., and Lewis, D., "Reference radiochromic film dosimetry: Review of technical aspects," Phys Med **32** (4), 541-556 (2016).

Faddegon, B. A., Ross, C. K., and Rogers, D. W., "Forward-directed bremsstrahlung of 10- to 30-MeV electrons incident on thick targets of Al and Pb," Med Phys **17** (5), 773-785 (1990).

Gibbons, J. P., Antolak, J. A., Followill, D. S., Huq, M. S., Klein, E. E., Lam, K. L., Palta, J. R., Roback, D. M., Reid, M., and Khan, F. M., "Monitor unit calculations for external photon and electron beams: Report of the AAPM Therapy Physics Committee Task Group No. 71," Med Phys **41** (3), 031501 (2014).

Haytmyradov, M., Mostafavi, H., Wang, A., Zhu, L., Surucu, M., Patel, R., Ganguly, A., Richmond, M., Cassetta, R., Harkenrider, M. M., and Roeske, J. C., "Markerless tumor tracking using fast-kV switching dual-energy fluoroscopy on a benchtop system," Med Phys **46** (7), 3235-3244 (2019).

Jiang, S. B., Pope, C., Al Jarrah, K. M., Kung, J. H., Bortfeld, T., and Chen, G. T., "An experimental investigation on intra-fractional organ motion effects in lung IMRT treatments," Phys Med Biol **48** (12), 1773-1784 (2003).

Keall, P. J., Mageras, G. S., Balter, J. M., Emery, R. S., Forster, K. M., Jiang, S. B., Kapatoes, J. M., Low, D. A., Murphy, M. J., Murray, B. R., Ramsey, C. R., Van Herk, M. B., Vedam, S. S., Wong, J. W., and Yorke, E., "The management of respiratory motion in radiation oncology report of AAPM Task Group 76," Med Phys **33** (10), 3874-3900 (2006).

Kirby, N., Chuang, C., Ueda, U., and Pouliot, J., "The need for application-based adaptation of deformable image registration," Med Phys **40** (1), 011702 (2013).

Kubo, K., Monzen, H., Tamura, M., Hirata, M., Ishii, K., Okada, W., Nakahara, R., Kishimoto, S., Kawamorita, R., and Nishimura, Y., "Minimizing dose variation from the interplay effect in stereotactic radiation therapy using volumetric modulated arc therapy for lung cancer," J Appl Clin Med Phys **19** (2), 121-127 (2018).

Liu, W., Haley, B. M., Kwasny, M. J., Li, J. J., Grdina, D. J., Paunesku, T., and Woloschak, G. E., "The effects of radiation and dose-fractionation on cancer and non-tumor disease development," Int J Environ Res Public Health **9** (12), 4688-4703 (2012).

Low, D. A., Harms, W. B., Mutic, S., and Purdy, J. A., "A technique for the quantitative evaluation of dose distributions," Med Phys **25** (5), 656-661 (1998).

Mageras, G. S., Pevsner, A., Yorke, E. D., Rosenzweig, K. E., Ford, E. C., Hertanto, A., Larson, S. M., Lovelock, D. M., Erdi, Y. E., Nehmeh, S. A., Humm, J. L., and Ling, C. C., "Measurement of lung tumor motion using respiration-correlated CT," Int J Radiat Oncol Biol Phys **60** (3), 933-941 (2004).

Masi, L., Doro, R., Favuzza, V., Cipressi, S., and Livi, L., "Impact of plan parameters on the dosimetric accuracy of volumetric modulated arc therapy," Med Phys **40** (7), 071718 (2013).

McNiven, A. L., Sharpe, M. B., and Purdie, T. G., "A new metric for assessing IMRT modulation complexity and plan deliverability," Med Phys **37** (2), 505-515 (2010).

Miften, M., Olch, A., Mihailidis, D., Moran, J., Pawlicki, T., Molineu, A., Li, H., Wijesooriya, K., Shi, J., Xia, P., Papanikolaou, N., and Low, D. A., "Tolerance limits and methodologies for IMRT measurement-based verification QA: Recommendations of AAPM Task Group No. 218," Med Phys **45** (4), e53-e83 (2018).

Morrison, H., Menon, G., and Sloboda, R. S., "Radiochromic film calibration for low-energy seed brachytherapy dose measurement," Med Phys **41** (7), 072101 (2014).

NCI, "Cancer Stat Facts: Lung and Bronchus Cancer", (2019).

NCI, "Non-Small Cell Lung Cancer Treatment (PDQ®)–Health Professional Version", (National Cancer Institute, 2019).

Niroomand-Rad, A., Blackwell, C. R., Coursey, B. M., Gall, K. P., Galvin, J. M., McLaughlin, W. L., Meigooni, A. S., Nath, R., Rodgers, J. E., and Soares, C. G., "Radiochromic film dosimetry: recommendations of AAPM Radiation Therapy Committee Task Group 55. American Association of Physicists in Medicine," Med Phys **25** (11), 2093-2115 (1998).

Onishi, H., Shirato, H., Nagata, Y., Hiraoka, M., Fujino, M., Gomi, K., Karasawa, K., Hayakawa, K., Niibe, Y., Takai, Y., Kimura, T., Takeda, A., Ouchi, A., Hareyama, M., Kokubo, M., Kozuka, T., Arimoto, T., Hara, R., Itami, J., and Araki, T., "Stereotactic body radiotherapy (SBRT) for operable stage I non-small-cell lung cancer: can SBRT be comparable to surgery?," Int J Radiat Oncol Biol Phys **81** (5), 1352-1358 (2011).

Papanikolaou, N. and Stathakis, S., "Dose-calculation algorithms in the context of inhomogeneity corrections for high energy photon beams," Med Phys **36** (10), 4765-4775 (2009).

Perez Azorin, J. F., Garcia, L. I., Ozcoidi, D. M., and Almansa, J. F., "Polarized dosimetry method for Gafchromic EBT3," Phys Med **32** (8), 972-980 (2016).

Poulsen, P. R., Schmidt, M. L., Keall, P., Worm, E. S., Fledelius, W., and Hoffmann, L., "A method of dose reconstruction for moving targets compatible with dynamic treatments," Med Phys **39** (10), 6237-6246 (2012).

Shah, C., Kestin, L. L., Hope, A. J., Bissonnette, J. P., Guckenberger, M., Xiao, Y., Sonke, J. J., Belderbos, J., Yan, D., and Grills, I. S., "Required target margins for image-guided lung SBRT: Assessment of target position intrafraction and correction residuals," Pract Radiat Oncol **3** (1), 67-73 (2013).

Shieh, C. C., Keall, P. J., Kuncic, Z., Huang, C. Y., and Feain, I., "Markerless tumor tracking using short kilovoltage imaging arcs for lung image-guided radiotherapy," Phys Med Biol **60** (24), 9437-9454 (2015).

Sonke, J. J., Lebesque, J., and van Herk, M., "Variability of four-dimensional computed tomography patient models," Int J Radiat Oncol Biol Phys **70** (2), 590-598 (2008).

Stambaugh, C., Nelms, B. E., Dilling, T., Stevens, C., Latifi, K., Zhang, G., Moros, E., and Feygelman, V., "Experimentally studied dynamic dose interplay does not meaningfully affect target dose in VMAT SBRT lung treatments," Med Phys **40** (9), 091710 (2013).

Tian, Y., Wang, Z., Ge, H., Zhang, T., Cai, J., Kelsey, C., Yoo, D., and Yin, F. F., "Dosimetric comparison of treatment plans based on free breathing, maximum, and average intensity projection CTs for lung cancer SBRT," Med Phys **39** (5), 2754-2760 (2012).

Vassiliev, O. N., Titt, U., Ponisch, F., Kry, S. F., Mohan, R., and Gillin, M. T., "Dosimetric properties of photon beams from a flattening filter free clinical accelerator," Phys Med Biol **51** (7), 1907-1917 (2006).

Zhong, H., Kim, J., Li, H., Nurushev, T., Movsas, B., and Chetty, I. J., "A finite element method to correct deformable image registration errors in low-contrast regions," Phys Med Biol **57** (11), 3499-3515 (2012).

Zou, W., Yin, L., Shen, J., Corradetti, M. N., Kirk, M., Munbodh, R., Fang, P., Jabbour, S. K., Simone, C. B., 2nd, Yue, N. J., Rengan, R., and Teo, B. K., "Dynamic simulation of motion effects in IMAT lung SBRT," Radiat Oncol **9**, 225 (2014).

Vita

Andrew Scott McGuffey was born in Bowling Green, KY, in 1994. Andrew graduated from Allen County-Scottsville High School in 2013 and enrolled at Western Kentucky University, where he majored in Physics. Upon graduating with a B.S. in Physics from WKU in 2017, Andrew matriculated into the LSU Medical Physics and Health Physics Graduate Program to pursue an M.S. in Medical Physics. Following his anticipated graduation with an M.S. degree in Summer, 2020, Andrew plans to continue his education toward a Ph.D. in Medical Physics.